2-1-2011

Modeling of Flash Boiling Flows in Injectors with Gasoline-Ethanol Fuel Blends

Kshitij Deepak Neroorkar
University of Massachusetts - Amherst

Follow this and additional works at: http://scholarworks.umass.edu/open_access_dissertations

MODELING OF FLASH BOILING FLOWS IN INJECTORS WITH GASOLINE-ETHANOL FUEL BLENDS

A Dissertation Presented

by

KSHITIJ NEROORKAR

Submitted to the Graduate School of the
University of Massachusetts Amherst in partial fulfillment
of the requirements for the degree of

DOCTOR OF PHILOSOPHY

February 2011

Mechanical and Industrial Engineering

MODELING OF FLASH BOILING FLOWS IN INJECTORS WITH GASOLINE-ETHANOL FUEL BLENDS

A Dissertation Presented

by

KSHITIJ NEROORKAR

Approved as to style and content by:

_____

David P. Schmidt, Chair

_____

Stephen de Bruyn Kops, Member

_____

Michael Henson, Member

_____

Ronald O. Grover, Jr., Member

_____

Donald Fisher, Department Head
Mechanical and Industrial Engineering

To my lovely family

ACKNOWLEDGMENTS

ABSTRACT

MODELING OF FLASH BOILING FLOWS IN INJECTORS WITH GASOLINE-ETHANOL FUEL BLENDS

FEBRUARY 2011

KSHITIJ NEROORKAR

B.E., MUMBAI UNIVERSITY

M.S., UNIVERSITY OF ALABAMA AT BIRMINGHAM

Ph.D., UNIVERSITY OF MASSACHUSETTS AMHERST

Directed by: Professor David P. Schmidt

Flash boiling may be defined as the finite-rate mechanism that governs phase change in a high temperature liquid that is depressurized below its vapor pressure. This is a transient and complicated phenomenon which has applications in many industries. The main focus of the current work is on modeling flash boiling in injectors used in engines operating on the principle of gasoline direct injection (GDI). These engines are prone to flash boiling due to the transfer of thermal energy to the fuel, combined with the sub-atmospheric pressures present in the cylinder during injection. Unlike cavitation, there is little tendency for the fuel vapor to condense as it moves downstream because the fuel vapor pressure exceeds the downstream cylinder pressure, especially in the homogeneous charge mode. In the current work, a pseudo-fluid approach is employed to model the flow, and the non-equilibrium nature of flash boil-

ing is captured through the use of an empirical time scale. This time scale represents the deviation from thermal equilibrium conditions.

The fuel composition plays an important role in flash boiling and hence, any modeling of this phenomenon must account for the type of fuel being used. In the current work, standard, NIST codes are used to model single component fluids like n-octane, n-hexane, and water, and a multi-component surrogate for JP8. Additionally, gasoline-ethanol blends are also considered. These mixtures are azeotropic in nature, generating vapor pressures that are higher than those of either pure component. To obtain the properties of these fuels, two mixing models are proposed that capture this non-ideal behavior.

Flash boiling simulations in a number of two and three dimensional nozzles are presented, and the flow behavior and phase change inside the nozzles is analyzed in detail. Comparison with experimental data is performed in cases where data are available. The results of these studies indicate that flash boiling significantly affects the characteristics of the nozzle spray, like the spray cone angle and liquid penetration into the cylinder. A parametric study is also presented that can help understand how the two different time scales, namely the residence time in the nozzle and the vaporization time scale, interact and affect the phenomenon of flash boiling.

TABLE OF CONTENTS

LIST OF TABLES

LIST OF FIGURES

xv

CHAPTER 1

INTRODUCTION

1.1 Flash Boiling

Flash boiling may be defined as the finite rate mechanism that governs phase change in a high temperature liquid that is depressurized below its vapor pressure. This phenomenon can be explained by considering the flow of a hot fluid through a nozzle as shown in Fig. 1.1. The elevated vapor pressure of this high temperature fluid makes it susceptible to vaporization since any pressure drop can cause the pressure to fall below the vapor pressure. Since the maximum pressure drop usually occurs at the inlet corner, vaporization may start at this location. This issue is further complicated when the downstream pressure is less than the saturation pressure of the fluid. In this case, the vapor formed inside the nozzle will continue to grow and will alter the characteristics of the ensuing spray. This process of flash boiling has significant applications in different industries.

For example, flash boiling has been considered as a possible method for improving fuel spray atomization during injection in internal combustion (IC) engines. Kim et al. [45] showed that flash boiling can improve engine performance. Kawano et al. [44] studied the effect of flash boiling on the spray, combustion and the exhaust emissions and concluded that flashing reduced smoke emission due to better atomization. In another application, flashing is induced in a certain type of desalination method known as Multi-Stage Flash Distillation (MSF). In the MSF process, heated seawater is passed into a vessel, known as a stage, where its pressure is suddenly dropped. This causes the water to flash, and the vapor generated by flashing is converted into

1
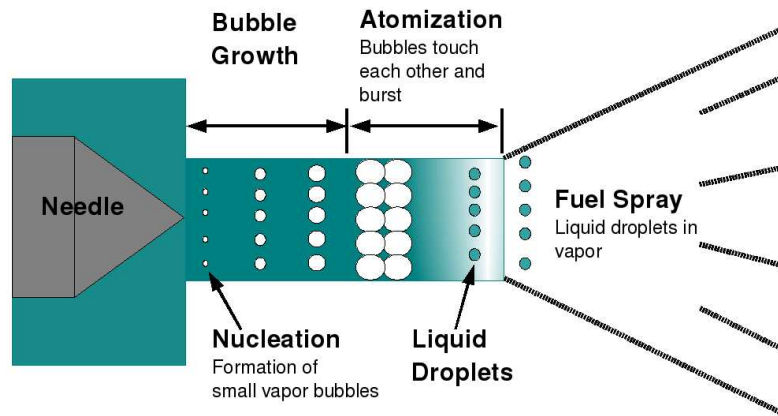
Figure 1.1. Process of flash boiling in nozzle, adapted from [67]

fresh water by condensing it on heat exchanger tubing [14]. Usually, there can be 15 to 25 such stages, and as the seawater flows from one stage to another, the flashing process continues since the pressure at each stage is lower than the previous one. An efficient method employed in paper drying is known as impulse drying and uses flash vaporization of the water in the paper [96]. Flash evaporation may be applied in wine making to cool grapes, concentrate the wine and to improve the wine quality [82]. In geothermal power plants based on water-based geothermal fields, flashing is used to convert the geofluid into vapor which is then passed through a turbine to generate power [22].

In addition, the study of flash vaporization is also important in order to address safety concerns in light water nuclear reactors. In case of a break in the cooling system circuit, known as a loss of coolant accident (LOCA), the high pressure water is exposed to low pressures and undergoes flashing. In such cases, the mass flow rate through the break will determine the time until the reactor core becomes uncovered
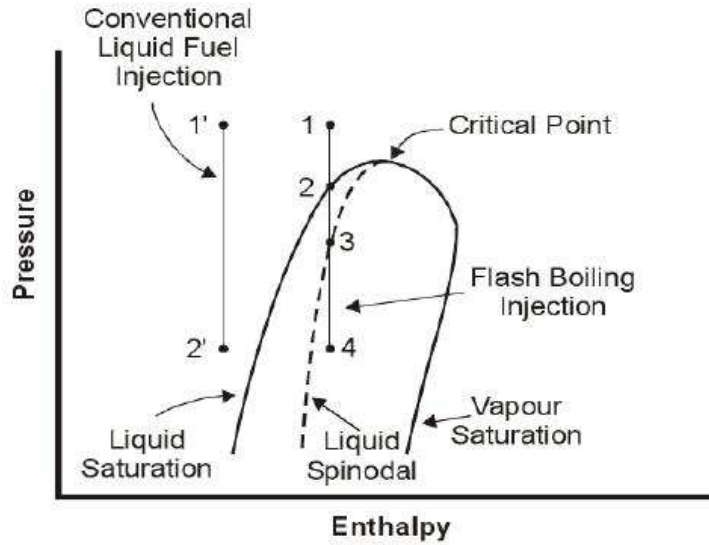
Figure 1.2. Pressure-enthalpy diagram showing the difference between conventional and flashing injection [68]

and the amount of water to be pumped in order to ensure sufficient cooling. Accurate prediction of this mass flow rate is extremely important to prevent overheating of the core [76].

In the current work, the application of flash boiling to fuel injection in IC engines is considered. However, most of the explanation of the physical processes in flash boiling and models developed would be valid for all applications.

1.1.1 Physics of Flash Boiling

The Fig. 1.2 shows the comparison between conventional injection and flash boiling injection on the pressure-enthalpy diagram of a single component fuel. Assume that the initial condition of the fuel is represented by point 1 in Fig. 1.2. As the fuel moves through the nozzle, its pressure reduces and once the pressure falls below point 2, vapor bubbles start appearing and growing. Beyond point 3, the vaporization of the liquid becomes extremely rapid. The point 3 lies on the liquid spinodal line, which will be explained in more detail later. In comparison to this process, in conventional

injection, as shown in Fig. 1.2, both the injection and the cylinder conditions lie in the subcooled section of the phase diagram.

The process of flash boiling can be divided into three stages [68] as shown in the Fig. 1.1: 1) nucleation, 2) bubble growth, and 3) atomization.

1) Nucleation: As the fluid is depressurized according to Fig. 1.2, beyond point 2, the liquid fuel exists in a metastable state. At this point any disturbances like dissolved gases, suspended particles, or wall roughness can lead to the formation of vapor bubbles. This is known as nucleation and the bubbles formed by this process exist in a metastable condition with the surrounding superheated fluid and can either grow or collapse on account of any disturbance in pressure. In this condition, the surface tension forces at the wall of the bubble balance the pressure differences between inside and outside the bubble as given by Eqn. 1.1

$$R_{cr} = \frac{2\sigma}{\Delta P} \tag{1.1}$$

where, R_{cr} is the critical radius of the nuclei, σ is the surface tension coefficient and ΔP is the pressure difference between the pressure inside the bubble and the pressure of the surrounding superheated liquid. If the radius of the nuclei formed exceeds R_{cr}, the vapor bubble will grow, otherwise it will collapse as the surface tension force will resist its growth.

This nucleation process can take place in two ways: heterogeneous or homogeneous. Heterogeneous nucleation involves the formation of nuclei on imperfections on the nozzle walls, on suspended solid particles or on trapped air bubbles. In case there is a small amount of dissolved gas in the liquid, the amount of superheat achievable by the liquid diminishes due to heterogeneous nucleation [58]. This is because dissolved gases are found to decrease the critical bubble radius [83].

4

Homogeneous nucleation occurs at high degrees of superheat and at random locations in the liquid. The occurrence of homogeneous nucleation is due to density fluctuations occurring in the superheated liquid at the molecular scale [37]. Homogeneous nucleation accelerates with the increase in the degree of superheat. The number of nuclei formed that will have radii higher than R_{cr} can be found out by the fluctuation theory of statistical mechanics [37]. One useful result from this theory [48] is the equation for the mean square density fluctuation in a volume of fluid V and is given by

$$\frac{\overline{(\Delta\rho)^2}}{\rho^2} = \frac{kT}{V^2}K \qquad (1.2)$$

where k is the Boltzmann's constant and K is the isothermal compressibility and is given as

$$K = -\rho((\frac{\partial P}{\partial v})_T)^{-1} \qquad (1.3)$$

It can be seen from the Eqn. 1.2, that as the isothermal compressibility becomes large, the density fluctuations become large. There exists a locus on the saturation diagram of a fluid on which the value of the isothermal compressibility theoretically becomes infinite [37]. This locus is known as the spinodal curve and when the degree of superheat crosses this threshold, the liquid, theoretically, cannot exist in a superheated state and will spontaneously separate into two phases. This curve is shown in Fig. 1.2.

2) Bubble growth: Once the nuclei are formed, they start growing due to the pressure difference ΔP, while surface tension, liquid inertia and viscosity oppose growth. Bubble growth occurs due to evaporation at the bubble wall and this process proceeds in three stages, as shown in Fig. 1.3. In the first stage, the nuclei are small and surface tension is dominant and restricts growth. This is

known as the idle [68] or delay period [55]. The second stage starts after the nuclei have grown to around double their diameter. The liquid inertia forces become dominant and bubble growth in this stage is dominated by the pressure difference ΔP. In this period, the bubble grows very fast and its radius increases as a linear function of time. The third stage is called the heat-conduction controlled stage. During this stage, the growth rate is mainly controlled by the rate at which heat transfer can be achieved from the liquid to the bubble in order to supply the latent heat of vaporization. In this stage the bubble radius grows as square root of the time [55]. Many studies have been performed to analyze the growth rates of the bubbles during the various stages of its growth. For a review, refer to Sher et al. [83]. Most of these studies considered either the inertia dominated range or the heat diffusion dominated stage of bubble growth. Mikic et al. [52] proposed a simple equation to calculate the bubble growth rates in both the inertia and heat diffusion controlled stages of bubble growth. They used the Clausius-Clapeyron equation to find the relationship between the vapor pressure and the temperature, assuming that the vapor density is constant. Miyatake and Tanaka [54] developed an improved bubble radius equation to cover the entire range of bubble growth. They used an equation which represented the true non linear relationship between vapor pressure and temperature which was obtained from the steam tables instead of the Clausius-Clapeyron equation. They also considered the acceleration of bubble growth observed after the idle time. The results obtained are shown in the Fig. 1.3.

3) Atomization: Atomization involves the formation of liquid fuel droplets in a jet of fuel vapor. A mechanism for this process was proposed by Sher and Elata [84]. They proposed that as the bubbles grow, the different bubbles will eventually touch each other and burst, thereby converting the flow of bubbles in liquid to a flow of droplets in vapor. The surface energy required for formation
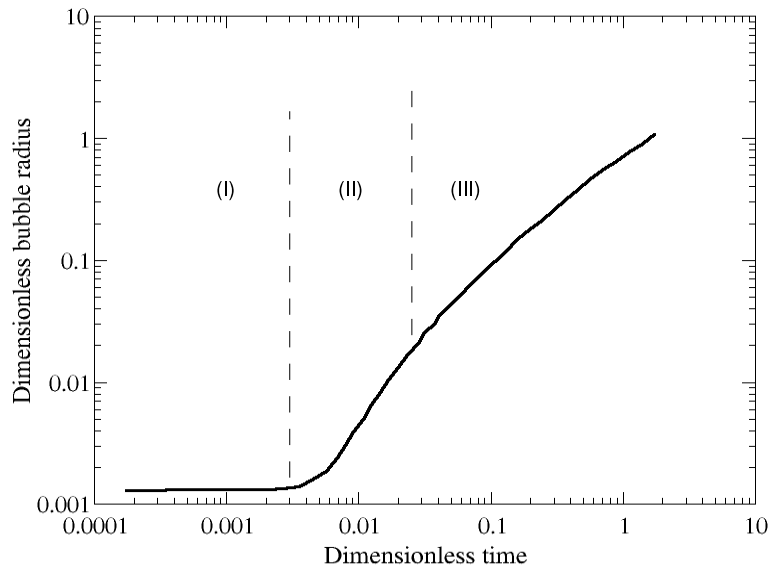
Figure 1.3. Bubble growth in superheated water based on [83, 55]

of the droplets is assumed to be provided by the energy contained in the bubbles at bursting. This mechanism of atomization would occur only in the case of nozzles that are very long so that the bubble can grow large enough to touch each other.

Another mechanism of flash boiling has been noted in literature and can be explained as follows. This phenomenon occurs when the amount of superheat is not high enough to initiate homogeneous nucleation within the liquid and when heterogeneous nucleation is suppressed. In a certain range of superheats and depending on the depressurization time scale, the phase change proceeds as an evaporation wave. This wave moves into the metastable liquid and leaves behind it a two phase mixture [37, 35, 85]. The experiments which have reported this mechanism consisted of connecting a vertical tube filled with a liquid in thermodynamic equilibrium to a very low-pressure chamber (see Fig. 1.4). As soon as the membrane between the liquid and the vacuum chamber is ruptured, rarefaction waves propagate through the liquid
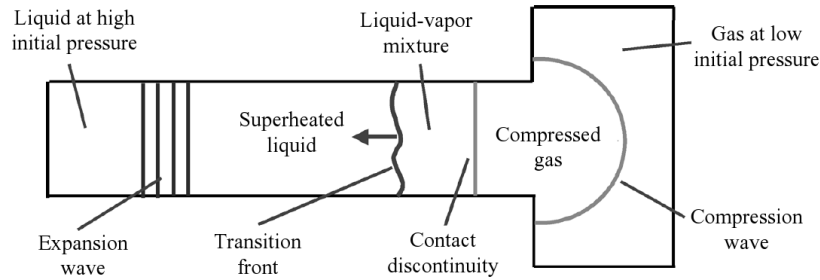
Figure 1.4. Simplied experimental setup used by Simões-Moreira and Shepherd [85] and associated waves.[78]

producing a superheated liquid. This is followed by the subsonic evaporation wave front. The different waves in the domain are shown in the Fig. 1.4. The above mechanism is mentioned here for completeness as it is known that industrial automotive fuels usually have dissolved impurities which act as nucleation sites for heterogeneous nucleation and so totally suppressing nucleation is very difficult.

1.2   Modeling of the Two-Phase Region Inside the Nozzle

The two phase mixture formed inside the nozzle due to the formation and growth of the bubbles determines the atomization and hence the quality of the ensuing spray. A significant amount of literature exists on the modeling of the two phase region inside the nozzle. Depending upon the distribution of bubbles in the liquid, there are two possible extremas that can be considered. In the first, it is assumed that one phase is finely dispersed in the other phase. In this case, there will be very little or no relative velocity between the phases, and such flows are called homogeneous flows. In the other extreme case, there can exist two separate streams with different phases. In this case, relative velocity between the phases needs to be considered and such flows are called separated flows. There are many other flow patterns identified in literature which lie between these two extremes [18]. Very often, simple analytical models are used to analyze multiphase flows [18]. For example:

1) Homogeneous flow model: The velocity, temperature and pressure of the phases are assumed to be equal due to very fast momentum, energy, and mass transfer between the phases so that equilibrium is reached. This assumption is valid when one phase is finely dispersed in another phase. The resulting conservation equations resemble those for a single fluid. The properties of density, internal energy, viscosity, and thermal conductivity are obtained by performing an average over the two phases.

2) Separated flow model: This model eliminates the assumption of equal phase velocities so that two different velocities are considered for the phases. This is important when buoyancy effects become dominant due to a large difference between the densities of the two phases [18]. In this case, there will be two momentum equations each containing a term that represents the drag at the interphase caused by the relative velocity between the phases.

3) Two fluid model: The two phases are treated as separate fluids with different sets of governing differential equations. In this case, each phase has its own velocity, temperature and pressure. The unequal phase velocities arises due to unequal densities, similar to the separated flow model. The thermal nonequilibrium is caused due to time lag of heat diffusion from one phase to another. This was discussed in the bubble growth section as the final stage of bubble growth. The presence of a pressure nonequilibrium can be due to three effects: 1) A pressure difference is required to balance the surface tension forces at the interface. 2) There is a pressure difference due to evaporation or condensation at the interface. 3) The third effect occurs when one phase has a larger pressure relative to the other phase due to very rapid pressurization effects. The modeling of pressure nonequilibrium is complicated and it is usually neglected [18]. The transport equations for the phases usually include source terms that rep-

resent the interphase transfer of momentum, heat and pressure (if considered) and need to be modeled using constitutive equations.

An important phenomenon associated with multiphase flows is called the choking (or critical) condition. This is the condition in which the mass flow rate is independent of the back pressure. Two-phase choking is extremely important for industrial applications since this condition limits the amount of mass flow rate that is achievable in the system. In single phase fluids, this condition occurs when the fluid velocity becomes equal to the speed of sound. Understanding critical flow is more complicated for multiphase flows since the speed of sound concept becomes non-trivial due to the presence of two phases. Different models have been used to predict the maximum mass flow rate achievable under the critical flow condition.

1) Homogeneous equilibrium model (HEM): The assumptions used by this model are the same as those used by the homogeneous flow model mentioned above. The prediction of the critical mass flow rate is quite accurate in the case of long pipes where there is sufficient time for equilibrium to be achieved and also when the flow pattern is such that the relative motion between the phases is not very important [93]. In this case the flow will be choked when the mass flow rate equals the mixture density times the sonic velocity in the mixture. Hence this is a direct extension of single phase flow.

2) Frozen flow model: This model assumes that the flow is frozen, so that there is no phase change. This is valid for short nozzles wherein the flow-through time is very short. Henry and Fauske [36] presented a frozen flow model which, in addition to frozen flow, made additional assumptions like the velocities of the phases are equal, there is no heat and mass transfer between the phases, and the expansion of vapor is isentropic. They used gas dynamics principles to calculate the critical flow rate.

3) Slip flow model: These models are similar to the separated flow model presented above so that the velocity difference between the phases is considered. Slip flow models were developed by Fauske [27] and Moody [57]. The slip flow model of Moody [57] was formulated by combining the continuity and energy equations to get an equation for mass flow rate. Then the mass flow rate was differentiated with respect to the slip ratio and equated to zero to obtain the slip ratio for maximum mass flow rate.

All the models mentioned above for simulating two phase flows are one dimensional models and make many simplifying assumptions about the two phase flow. These assumptions make the models specific to certain types of problems and limit their general applicability. The two main assumptions are of momentum equilibrium (equal velocities of the phases) and thermal equilibrium. Attou et al. [7] studied the importance of considering the slip between the phases. They applied the conservation of mass, momentum and energy on a control volume with a two-phase, bubbly liquid entering through a small orifice and expanding into a larger chamber. They assumed a steady state, sub-sonic flow with thermal equilibrium between the phases and derived two simple one dimensional models, namely, MEM (Momentum Equilibrium Model, assuming maximum momentum transfer or no slip between phases) and MFM (Momentum Frozen Model, assuming negligible momentum transfer or maximum slip between the two phases). It was found that in the MEM, due to complete momentum transfer between the phases, the lower inertia of the gas causes the liquid to decelerate faster than in reality, leading to a higher pressure recovery than predicted in experiments. Consequently, the MFM causes the liquid to decelerate slower and hence the pressure recovery predicted is lower than in experiments. Finally, a flow model is proposed which considers the drag on the bubble and is found to match the experimental data well.

The assumption of thermal equilibrium is found to be satisfactory for small-scale cavitating flows, but this assumption will lead to huge errors in flash boiling simulations. Kato et al. [43] presented an equation which gave the relative importance between bubble growth due to inertial and thermal effects. Schmidt [79] used this equation and performed calculations to show that the length scales required for the thermal effects to be important are much larger than the nozzles usually used in injectors. The reason for this is that the majority of the energy required for phase change is provided by the inter-phase heat transfer. In cavitating flows, the heat transfer is extremely fast [46] and hence the time scale for heat transfer is much smaller than the flow-through times in the nozzle. However, this is not the case in hot fluids, in which the rate of heat transfer is limited by the inter-phase heat transfer process. This can be explained further with the help of the non-dimensional Jakob number which is calculated from Eqn. 1.4.

$$Ja = \frac{\rho_l C_p \Delta T}{\rho_v h_{fg}} \tag{1.4}$$

Here ρ is the density and the subscripts l and v represent liquid and vapor, respectively. The variable C_p stands for the specific heat at constant pressure, ΔT represents the degree of superheat, and h_{fg} is the latent heat of vaporization. The Jakob number is the ratio of the amount of sensible heat available to the amount of energy required for vaporization. In cases where the Jakob number is very high, the available energy is much larger than the energy required for vaporization and hence for such cases, the heat transfer time scale can be assumed to be much smaller than the flow time scales. The Ja is mainly a function of the degree of superheat and the temperature of the fluid. At a constant superheat, as the temperature of the fluid increases, the denominator of the above equation increases. For example, the values of Ja for water at 300K and 320K are 668 and 241 respectively at a degree of superheat of 10K. Hence it can be seen that the value of Ja diminishes sharply

as temperature increases, and it can be expected that at much higher temperatures, it becomes close to unity. This means that at higher temperatures, the amount of energy available becomes close to the amount of energy required for vaporization.

Schmidt [79] simulated the flash-boiling experiment of Reitz [74] using a cavitation model that was based on the assumption of thermal equilibrium and another model that was based on the Homogeneous Relaxation Model (HRM) which will be explained below. It was observed that as the temperature of the fluid was increased, the mass flow rates predicted by the equilibrium model diverged further from the experimental values; however, the non-equilibrium HRM successfully predicted the experimental mass flow rates. This shows that in order to accurately simulate flash boiling, the model must capture the finite rate of interphase heat transfer.

A wide range of models have been developed and presented which try to incorporate some non equilibrium effects. These are divided into three groups: empirical models, models based on homogeneous flow assumption, and two-fluid models with interphase interaction terms

1) Empirical models: The model of Henry and Fauske [36] used an experimentally correlated coefficient to represent the non equilibrium vapor generation as a fraction of the equilibrium vapor generation.

2) Models based on homogeneous flow assumption: Downar-Zapolski et al. [24] used the HRM which accounted for the nonequilibrium vapor generation by introducing a relaxation term into the transport equation for quality. The relaxation term implied that the instantaneous quality would relax to the equilibrium value over a given time. This relaxation time was empirically correlated to represent the data of Reocreux [75]. The time scale is such that a very high value corresponds to a very small inter-phase mass transfer and the model takes the form of a homogeneous frozen model. In case of very low values of the time scale, the time required for equilibrium to be achieved is very low and the model

13

corresponds to a HEM model. Gopalakrishnan and Schmidt [33] used the HRM for two and three dimensional simulations. They incorporated the HRM into their pressure equation so that the final pressure equation satisfied compressibility as well as the density change due to phase change. This eliminated the need of solving a transport equation for mass fraction. Their model successfully predicted the vapor lock phenomenon. Blinkov et al. [13] developed a homogeneous model which used five transport equations: 2 equations for the mixture and vapor densities, momentum equation for the mixture, energy equation for the liquid and a bubble number density equation. Constitutive equations based on empirical data were used for the wall friction, rate of vapor generation, interfacial heat transfer and nucleation. The relations for wall friction and interfacial heat transfer were different for different sections of the flow field depending on whether the flow was bubbly, slug (large bubbles) or had liquid droplets dispersed in vapor. The constitutive relation for nucleation included a term for wall nucleation and bulk nucleation i.e. nucleation occurring from suspended particles in the liquid. All the bubbles at each cross section in the nozzle were assumed to have the same size. Chang and Lee [16] suggested an improvement to the model of Blinkov et al. to include the bubble size distribution through the assumption that bubbles exist in discrete groups depending on their size. They solved conservation equations for mixture density, mixture momentum, energy conservation and finally an equation for the bubble mass in each mass group. The source terms for the bubble mass equation included the effect of wall nucleation, bulk nucleation and shifting between the different mass groups. Their results indicated that considering the bubble size distribution is important for prediction of void fraction development in the nozzle. Bianchi et al. [10] also used the HRM equation to model the non-equilibrium vapor generation. In addition to the time scale based on quality used in the original model,

14

they use a time scale which was derived by Bilicki et al [12] and Mohammadein [56] based on the temperature changes of a growing vapor bubble surrounded by superheated liquid. Both relaxation times were calculated and the longer one was used to drive the flow to equilibrium. An atomization sub-model was considered to calculate the effect of the liquid superheat and turbulence on the liquid droplet diameters. Atomization was assumed to occur when the sum of two energies, energy due to the difference between the bubble pressure and the discharge pressure and the energy due to turbulence fluctuations, overcame the surface tension force on the bubble. Finally, the size of liquid droplets formed were determined from a probability density function. They found that increasing the superheat degree causes more droplets to have a uniform size and that this uniform size reduces with increasing the superheat. This is because as the superheat increases, heat transfer process becomes faster and has more possibility of reaching equilibrium, and hence the atomization process is more uniform. All models mentioned in this section, except the one used by Gopalakrishnan and Schmidt, were one dimensional models which modeled the multiphase friction coefficient as a correction multiplier times the friction coefficient for single phase liquid flow. Gopalakrishnan and Schmidt [33] used the viscous stress term of the momentum equation.

3) Models based on a two-fluid approach : Richter [76] developed a 1D model which solved 6 transport equations. These included two for mass balance of liquid and gas phases, two for momentum balances, one for the energy balance of the two-phase system and one for vapor generation. Correlations were used for the wall friction and the interphase heat transfer coefficient. The interfacial drag was calculated for lower void fraction regions using a constitutive equation for bubbly flow, whereas for high void fractions, an equation for annular flow was assumed. For intermediate void fractions, a weighted average of the

interfacial friction coefficients for the two regimes was used. Due to the phase change process, an additional term appeared in the source terms of the momentum equations which considered the momentum exchange due to phase change. For example, when a liquid evaporates, its velocity gets changed from the liquid velocity to the vapor velocity and this is also a source of momentum exchange. The heat transfer coefficient included heat exchange due to conduction and convection. The amount of vapor generated was calculated from an energy balance thereby satisfying the condition that the interfacial heat transfer limits the vaporization process. The initial bubble diameter and number of nucleation sites were constant values adjusted to fit experimental data. The results from this model suggested the following trend: In the initial stages of bubble growth, the bubbles are dispersed in the liquid and an assumption of hydrodynamic/momentum equilibrium is applicable, however, thermal nonequilibrium has to be considered since the surface area available for heat transfer is very less. As the bubbles grow and the void fraction exceeds a value of 0.3, thermal equilibrium can be assumed but slip between the phases becomes important and ignoring it will cause inaccuracies.

As can be observed from the above models, the more the amount of physics that one chooses to incorporate in the model, the more the experimental data required for deriving constitutive relations. Hence none of the above models can claim to be completely free of empirical correlations, and hence none of the models is applicable to all cases. This is an indication of the complexities involved in the flash boiling process.

The next section discusses the advantage of using fuel injectors operating on the principle of Gasoline Direct Injection (GDI) and the importance of studying flash boiling for designing these injectors.

1.3   Gasoline Direct Injection (GDI)

The fuel economy of a diesel engine is found to be much superior to the Port-Fuel Injection (PFI) engine due to its high compression ratio and unthrottled operation. However, the diesel engine also suffers from higher noise and vibration level, a limited speed range and higher emissions [98]. Hence research has been done to develop an engine which would exhibit a fuel economy similar to a diesel engine and, at the same time, incorporate the features of a PFI engine, like lower emissions. The Gasoline Direct Injection (GDI) engine promises to be a good candidate for such an engine. These engines operate on the concept of direct injection of gasoline into the combustion chamber. GDI engines are known to enhance the specific fuel consumption of gasoline greatly as compared to the PFI system [5]. In addition to this, directly injecting gasoline into the combustion chamber provides many other critical advantages. One of the major differences in the PFI system and the GDI system are in the mixture preparation method. As shown in Fig. 1.5 , in a PFI engine the fuel is injected on the back of the intake valve. There is a lag between the injection of the fuel and the beginning of the induction stroke. This causes a film of liquid fuel to collect near the intake valve area. This fuel wall wetting causes metering errors and higher emissions of UHCs. The direct injection of gasoline (Fig. 1.5) may be able to overcome these problems since the gasoline is injected directly into the cylinder. The GDI engine also offers the potential for leaner combustion and lower cylinder-to-cylinder air-fuel mixing variation [98]. During cold starting, fuel vapor pressure is much lower and this leads to a lot of liquid fuel getting collected at the intake port area of the PFI system leading to increased UHC emissions during the first few engine cycles during starting. The high fuel pressure employed in the GDI system leads to a much higher degree of fuel atomization and fuel vaporization rate [98]. Therefore, GDI engines can potentially achieve cold-start UHC emissions that are comparable to the levels observed during steady operating conditions.
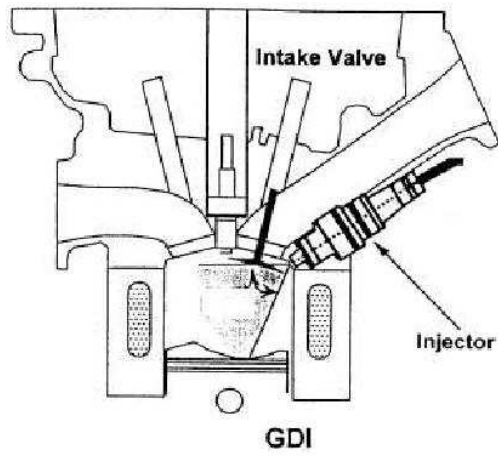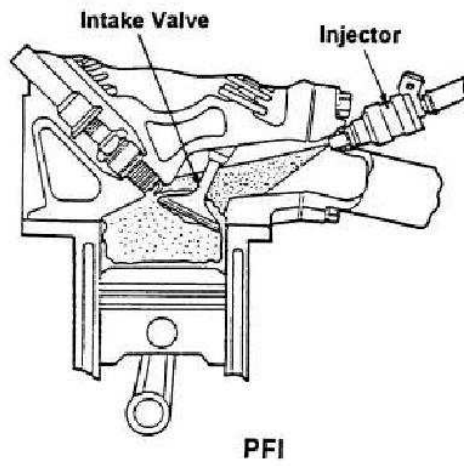
Figure 1.5. PFI versus GDI system [98]

The GDI engines theoretically can be designed to operate in two modes: a homogeneous mode for high load conditions and a stratified mode for part load conditions. In the homogeneous mode, the fuel is injected during the intake stroke and as the volume in the combustion chamber increases, the spray disperses in the cylinder forming a homogeneous air fuel mixture in the entire cylinder. In the stratified mode, the fuel is injected during the compression stroke and the mixture is prepared such that a stoichiometric mixture exists only in the vicinity of the spark plug and the mixture is lean in rest of the cylinder. The piston head of the GDI engine has a curved shape, as shown in Fig. 1.5 to direct the fuel into a reversed flow that carries it to the spark plug. The stratified mode of operation will help in significantly reducing the specific fuel consumption of the engine as compared to the PFI system [40]. Additionally, in the stratified mode, throttling can be eliminated, thereby minimizing the power loss associated with sucking air into the cylinder through the throttle restriction. In spite of the above mentioned advantages of the GDI system, it suffers from two major drawbacks. The first drawback is due to its mixture preparation strategy which provides very little time for fuel-air mixing. Secondly, due to its high pressure operation the high velocity fuel emerging from the fuel injector may impinge onto the piston head forming a liquid film near the piston and promoting the emission of UHCs. In order to eliminate this problem it is necessary to reduce the droplet sizes of the fuel spray, increase the spray cone angle, and reduce the penetration of the fuel jet into the cylinder. This can be achieved through flash boiling. Moreover, it has been observed that when GDI engines operate in the homogeneous mode with injection during the intake stroke, the pressure in the cylinder can drop below the fuel's vapor pressure causing it to flash boil. Hence, to eliminate the problems with the GDI engines, it is essential to study the phenomenon of flash boiling and find a way to control it in order to increase the usability of the GDI engine. The atomization requirements for GDI engines become more strict in case they are to be used with alternative fuels

19

like ethanol. This is mainly due to the fact that ethanol has a lower vapor pressure, and hence using fuels with 85 percent or higher ethanol content may lead to much higher emissions unless they are properly atomized. The next sections deal with the importance of investigating the use of ethanol as an alternative for gasoline and also the different methods that can be used to model flash boiling of gasoline-ethanol fuel blends.

1.4 Ethanol as Transportation Fuel

In 2008, the United States was the world's leading consumer of petroleum and was estimated to be using more than 7.6 billion barrels of oil a year. More than two thirds of this oil was utilized by the transportation sector. By 2030, it is predicted that the US will import an additional 4 million barrels of petroleum per day as compared to 2005 [4]. As most of this oil is imported, there are periodic supply interruptions leading to price fluctuations, economic instability, and great inconvenience to consumers. In addition to the economic concerns, the transportation sector is responsible for more than one-third of the United States total greenhouse gas emissions [4]. To address these issues, in recent times, research has pursued development of alternative energy resources to replace traditional, oil-based fuels. A possible alternate fuel is ethanol since it can be made from biomass and therefore may be considered as a renewable fuel [2, 38]. In the past few decades, a fuel with 10 percent ethanol and 90 percent gasoline, known as E10, has been used as automotive fuel in the United States. The addition of ethanol to gasoline has the following advantages:

1) Ethanol increases the octane rating of the fuel, thereby helping to reduce knocking. A higher compression ratio can be used which increases the power density and fuel efficiency.

3) Benzene is a very toxic compound emitted from vehicles and is a product of the combustion of aromatic compounds present in gasoline [95]. Increasing

20

aromatics in the fuel has also been found to increase particulate emissions [34]. Since both ethanol and aromatic compounds boost the octane rating of gasoline, refineries can reduce the amount of aromatic compounds in gasoline and achieve the same octane rating in the fuel through the addition of ethanol. Reducing aromatics in this way greatly reduces the emission of benzene and particulate matter [95].

2) Addition of ethanol leads to a reduction in exhaust emissions of carbon monoxide. This effect is due to the presence of an additional oxygen atom in the ethanol molecule which increases the amount of oxygen available for combustion thereby causing the engine to burn leaner than the stoichiometric ratio. The impact of this oxygen atom is not significant in vehicles using closed-loop control [42]. In such vehicles, the air/fuel ratio is adjusted based on the exhaust oxygen sensor data and the amount of fuel is automatically increased to accomodate for this "leaning" effect.

E10 can be used in conventional gasoline engines without any modifications. However, recently, car manufacturers have been producing cars that can run on fuels with up to 85 percent ethanol, known as E85. A major disadvantage of using E85 is that it has an energy content that is 71.95 percent that of gasoline [77] and, according to the National Ethanol Vehicle Coalition [3], using E85 instead of gasoline may decrease the fuel economy by 5 to 12 percent. Also, E85 has a lower vapor pressure than gasoline and hence the application of flash boiling to improve fuel atomization becomes very important in order to reduce UHC emissions and improve fuel efficiency.

1.5 Multicomponent Fuel Simulations

In flash boiling simulations of actual automotive fuels, multicomponent fuel modeling is extremely important for understanding the true nature of the phenomenon.

This is evident in the experiments of Schmitz et al. [81] which showed that though many single component fuels like iso-octane have been used to simulate gasoline, their spray and vaporization characteristics can differ significantly as compared to multi-component fuels. The only known flash boiling simulation for internal nozzle flow, conducted with multicomponent fuel was that by Lee et al.[49] for JP8 aviation fuel. They used a surrogate i.e. a mixture of limited number of hydrocarbons that represents some commercial fuel. In general, surrogates can be classified into three types: [26]

1) Physical surrogates: have the same physical properties as the real fuel

2) Chemical surrogates: have the same chemical properties as the real fuel

3) Comprehensive surrogates: have the same physical and chemical properties as the commercial fuel

The type of surrogate being used depends on the kind of fuel properties required. For flashing simulations, the two phase region is very important and so the surrogate has to properly reproduce the volatility of the fuel which is represented by the distillation curve [91]. Violi et al [91] developed surrogates for the aviation fuel JP8 intended to match the volatility, soot formation tendency, and combustion property. One of their surrogates named 'Sur2' was found to reproduce the distillation curve of JP8 very well. This surrogate was used by Lee et al. [49] to study internal flashing flows. The required properties were obtained from the standard code SUPERTRAPP [39].

Another approach for modeling multicomponent hydrocarbon is by continuous thermodynamics which has been used in the past for multicomponent droplet evaporation simulations [51, 90]. In this method, the composition of a complicated mixture is represented as a continuous distribution of some convenient macroscopic property

(I) such as boiling point or molecular weight [19]. The mole fraction of any species i in the multicomponent fluid is given as

$$y_i = y_f f(I)_i \Delta I_i \tag{1.5}$$

where, ΔI_i is the interval in I centered between the values of I corresponding to species i. The variable y_f is the fuel mole fraction and f is the distribution function. A common distribution function for petroleum fractions is the Γ distribution function [51, 90]. The model is applied to multicomponent vaporization studies by solving equations for the fuel molar fraction, the mean and the second moment of the distribution which represents the variance. At the interface between the two phases, vapor-liquid equilibrium is applied. All the properties of the mixture are calculated by combining property correlations with the distribution parameter.

Finally, a method traditionally employed in the petroleum industry is the use of cubic equations of state (EOS) like the Peng-Robinson or the Soave-Redlich-Kwong in conjunction with simple mixing rules like the van der Waals one-fluid mixing rules [29]. The main weakness of this method is that in order to accurately represent the vapor-liquid equilibrium behavior, empirical constants need to be specified. This makes these methods quite unsatisfactory when being used with mixtures for which there is a dearth of experimental data, like ethanol-gasoline blends.

None of the methods mentioned above have been used to model ethanol-gasoline fuel blends due to the highly non-ideal nature of this mixture which may be observed in the variation of the vapor pressure as a function of the ethanol concentration (Fig. 1.6). It can be seen that the vapor pressure of the mixture can be higher than that of either components. It is also observed that the ethanol concentration at which the maximum vapor pressure occurs, changes and is higher at higher temperatures. In addition, it is extremely difficult to get 100 percent pure ethanol due to its hygroscopic
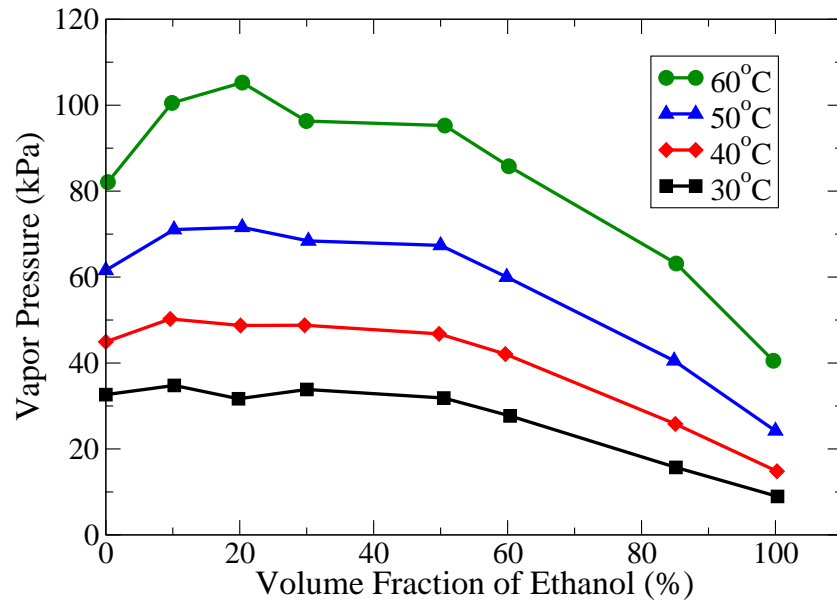
Figure 1.6. Vapor pressure of ethanol-gasoline blended fuel as a function of the volume percentage of ethanol [41]

nature and the presence of a small percentage of water can significantly alter the properties of the blended fuel [8].

Bennett et al.[9] tried to model the vapor-liquid equilibria (VLE) of ethanol hydrocarbon mixtures using a modified Peng-Robinson equation of state and van der Waals mixing rules and found that this method was not applicable to such non-ideal mixtures. Pumphrey et al. [71] proposed an approach for modeling ethanol-gasoline mixtures by treating them as pseudo binary systems of ethanol and gasoline. They used their experimental data for vapor pressures to fit the parameters of the Wilson equation. The Wilson equation is an equation which gives the excess Gibbs free energy in terms of the molar composition of a mixture [73]. This equation can be used to calculate the activity coefficients for the two components, which is a measure of the chemical potential. Finally, the activity coefficients were used to calculate the vapor pressure of the gasoline-alcohol mixture. The experimental data used to fit the parameters used anhydrous ethanol and hence may not be very accurate for matching the vapor pressure of gasoline ethanol blends with water present. Balabin et al. [8]

24

and Kar et al. [41] used the Clausius-Clapeyron equation assuming the vapor to be an ideal gas to find the enthalpy of vaporization of ethanol-gasoline mixtures from their vapor pressure measurements. Additionally, VLE of complex mixtures of hydrocarbons with alcohols have been modeled through the use of the cubic plus association equation of state (CPAEOS) ([97]) and by combining the Peng-Robinson equation of state with a group contribution method to calculate the binary interaction parameters ([70]). In this case, the CPAEOS is an attractive option since all parameters required by the EOS can be obtained by regressing vapor pressure and liquid density data and no experimental critical properties or accentric factors are required. However this method has yet to be applied to GE blends.

It can be observed that there is a need to develop and test a model which can provide the VLE properties and volatility information required for accurate flash boiling simulations of G-E fuel blends.

CHAPTER 2

METHODOLOGY

2.1 Modeling of the Flashing Process

The flashing process inside the nozzle is simulated using the HRM model which was presented by Gopalakrishnan and Schmidt [33], Lee et al. [49] and by Neroorkar et al. [61]. The concept of the model has been explained in the preceding chapter and the current section will deal with the governing equations, the complete model formulation and the numerical strategy.

2.1.1 Governing Equations

The governing equations include the continuity and momentum equations denoted by Eqns. 2.1 and 2.2.

$$\frac{\partial \rho}{\partial t} + \nabla \cdot \phi = 0 \tag{2.1}$$

$$\frac{\partial \rho U}{\partial t} + \nabla \cdot (\phi U) = -\nabla p + \nabla \overline{\overline{\tau}} \tag{2.2}$$

where ρ is the density, U is the velocity, p is the pressure, and t is the time. The variable $\overline{\overline{\tau}}$ represents the shear stress and ϕ represents the mass flux which is given as

$$\phi = \rho U \tag{2.3}$$

At present, no turbulence model has been incorporated and laminar flow is assumed. The reason for this assumption is that our main focus in this paper is understanding the effect of flash boiling on the flow. The study of flash boiling coupled with turbulence is left for future work.

As is common practice [28], the equation for pressure is derived by combining the continuity and momentum equations. However, since this is a multiphase model, the pressure equation cannot only include the divergence of velocity, but includes additional complexities owing to the phase change. To derive the pressure equation, we first start with a discretized form of the momentum equation

$$a_p U_p + \sum_N a_N U_N = r - \nabla p \tag{2.4}$$

where, the subscript p represents the computational cell under consideration and N represents the neighboring cells. The variable a represents the contributions from the specific cells and r is the contribution from the source terms to the linear system matrix. It is convenient to replace the off-diagonal and source term contributions by an operator H

$$H(U) = r - \sum_N a_N U_N \tag{2.5}$$

The momentum equation then becomes

$$a_p U_p = H(U) - \nabla p \tag{2.6}$$

In order to derive the pressure equation from this momentum equation, we consider the density to be a function of quality, in addition to pressure and enthalpy. The quality dependence of density is due to the thermal non equilibrium in the system [33] . In this case, the substantial derivative of density is given as

$$\frac{D\rho}{Dt} = \frac{\partial \rho}{\partial p}\Big|_{x,h} \frac{Dp}{Dt} + \frac{\partial \rho}{\partial x}\Big|_{p,h} \frac{Dx}{Dt} + \frac{\partial \rho}{\partial h}\Big|_{x,p} \frac{Dh}{Dt} \tag{2.7}$$

Subtracting the continuity equation, Eqn. 2.1, from the above equation and assuming adiabatic conditions, we get

$$-\rho \nabla \cdot U = \frac{\partial \rho}{\partial p}\Big|_{x,h} \frac{Dp}{Dt} + \frac{\partial \rho}{\partial x}\Big|_{p,h} \frac{Dx}{Dt} \tag{2.8}$$

Dividing Eqn. 2.6 by a_p and taking its divergence, we get an equation for the velocity divergence which is then substituted into the above equation to get

$$-\rho \nabla \cdot \frac{H(U)}{a_p} + \rho \nabla \cdot \frac{1}{a_p} \nabla p = \frac{\partial \rho}{\partial p} \mid_{x,h} \frac{Dp}{Dt} + \frac{\partial \rho}{\partial x} \mid_{p,h} \frac{Dx}{Dt} \qquad (2.9)$$

Expanding the substantial derivative for pressure,

$$\frac{\partial \rho}{\partial p} \mid_{x,h} (\frac{\partial p}{\partial t} + U \cdot \nabla p) + \frac{\partial \rho}{\partial x} \mid_{p,h} \frac{Dx}{Dt} + \rho \nabla \cdot (\frac{H(U)}{a_p}) - \rho \nabla \cdot (\frac{1}{a_p} \nabla p) = 0 \qquad (2.10)$$

Finally, adding the product of $\frac{p}{\rho} \frac{\partial \rho}{\partial p} \mid_{x,h}$ and Eqn. 2.1 to the above equation, we get

$$\frac{1}{\rho} \frac{\partial \rho}{\partial p} \mid_{x,h} (\frac{\partial \rho p}{\partial t} + \nabla \cdot \rho p \phi_v) + \rho \nabla \cdot (\frac{H(U)}{a_p}) - \rho \nabla \cdot \frac{1}{a_p} \nabla p + \frac{\partial \rho}{\partial x} \mid_{p,h} \frac{Dx}{Dt} = 0 \qquad (2.11)$$

The flash boiling model is then used to calculate the last term of the above equation. The first two terms in the above equation allow for the transmission of pressure waves for high Mach number flows and can be ignored for low Mach number flows.

2.1.2 Flash Boiling Model

The homogeneous relaxation model (HRM) was used to provide closure for the above mentioned system of equations. This model describes the rate at which the instantaneous (non equilibrium) mass fraction of vapor will tend towards its equilibrium value. The simple linearized form proposed by Bilicki and Kestin [11] for this rate equation is shown in Eqn. 2.12

$$\frac{Dx}{Dt} = \frac{\bar{x} - x}{\theta} \qquad (2.12)$$

In the above equation, x represents the instantaneous quality (mass fraction of vapor), $\bar{x}$ represents the equilibrium quality and θ represents the time scale over which x

relaxes to $\overline{x}$. The Eqn. 2.12 is a simple approximation to the extremely complicated processes that are associated with the flash boiling process. It can be noted that the the HRM equation is inserted into the last term of the pressure equation formulation, Eqn. 2.11. The value of $\overline{x}$ is obtained from a look-up table as a function of pressure and enthalpy. The instantaneous quality is calculated from the void fraction as shown below

$$x = \frac{\alpha \rho_v}{\rho} \tag{2.13}$$

where α is the void fraction of vapor, ρ is the density and the subscript v represents saturated vapor. The void fraction is calculated as follows

$$\alpha = \frac{\rho_l - \rho}{\rho_l - \rho_v} \tag{2.14}$$

The most important consideration while using the HRM model is the formulation of the time scale. Downnar-Zapolski [24] used the pressure profile and mass flux from the Moby Dick experiments of Reocreux [75] and combined their governing equations to derive an equation for the time scale. They found that in all cases, the time scale was a monotonically decreasing function of the void fraction and a non dimensional pressure. Based on their observations, they proposed the following equation for the time scale θ

$$\theta = \theta_0 \alpha^a \psi^b \tag{2.15}$$

where θ_0 is a constant and ψ is a non dimensional form of pressure. For lower pressures of up to 10 bar, the recommended coefficient values were $\theta_0 = 6.51 \cdot 10^{-4} s$, $a = -0.257$, and $b = -2.24$. The non dimensional form of the pressure proposed for these low pressures was

$$\psi = \frac{p_{sat} - p}{p_{sat}} \tag{2.16}$$

where p_{sat} is the saturation pressure. For higher pressures, the values of the coefficients are $\theta_0 = 3.84 \cdot 10^{-7}s$, $a = -0.54$, $b = -1.76$ and

$$\psi = \frac{p_{sat} - p}{p_c - p_{sat}} \tag{2.17}$$

where p_c is the critical pressure. Gopalakrishnan [32] also used a mixed correlation which used a and b values from the high pressure correlation while θ_0 and the form of ψ were taken from the low pressure correlation. In the current work, the complete high pressure correlation was considered in all cases unless specified otherwise.

2.1.3 Numerical Method

The first step in the numerical solution of the system of equations is the implicit solution of the continuity equation given in Eqn. 2.1. This is done by using a volumetric flux ϕ_v given as

$$\phi_v = U_f \cdot S_f \tag{2.18}$$

where U_f represents velocity interpolated to the cell face and S_f is the face normal area. The continuity equation then becomes

$$\frac{\partial \rho^{n+1}}{\partial t} + \nabla \cdot (\phi_v^n \rho^{n+1}) = 0 \tag{2.19}$$

where the superscript n represents the previous iteration, and $n + 1$ indicates that these variables are solved implicitly.

The next step involves updating of all the fluid properties, like the equilibrium mass fraction ($\overline{x}$), saturated liquid and vapor densities, vapor pressure, etc. In the work presented in Gopalakrishnan and Schmidt [33], curve fits were used to obtain some of the required properties for water. Schmidt et al. [80] and Neroorkar et al. [61] used the REFPROP database and code library [50] to obtain the properties of water and n-hexane respectively. REFPROP uses the Span and Wagner equation of state

30

[86] for the properties of n-hexane and the Wagner and Pruss equation of state [92] for water. Lee et al [49] used a look-up table generated by the code SUPERTRAPP [39] for the properties of JP8.

Finally, the momentum equation, Eqn. 2.2, is solved coupled with the pressure equation, Eqn. 2.11, using a predictor-corrector approach similar to the PISO method. The velocity field is predicted by solving the momentum equation using a lagged pressure field as shown below

$$\frac{\partial \rho U^0}{\partial t} + \nabla \cdot (\phi U^0) = -\nabla p^n + \nabla \mu \nabla U^0 \tag{2.20}$$

where U^0 indicates that the velocity is an estimation based on the value of pressure from the previous time step. The variable μ represents the dynamic viscosity of the fluid. The solution then proceeds by iteratively solving the pressure equation. However, the pressure equation has an added complexity due to the non-linear behavior of the last term in Eqn. 2.11, and the linearization of this term is achieved as follows. For ease of explanation, the form of the pressure equation without the compressible terms will be considered. From Eqn. 2.6, it can be observed that the term $\frac{H(U)}{a_p}$ is equivalent to the velocity field without the pressure gradient. The volumetric flux constructed from this velocity is represented by ϕ_v^*. Then Eqn. 2.11 can be written as

$$\rho \nabla \cdot \phi_v^* - L(p) + M(p) = 0 \tag{2.21}$$

where the second term represents the Laplacian term which is a linear function of pressure. The variable M represents the last term in the Eqn. 2.11, which introduces the nonlinearity to the pressure equation. In order to linearize this equation, a Newton's method is used. Given a function $f(p)$ and a derivative $J = f'(p)$, the Newton's method for the next best guess for the variable p is given as

$$Jp^{k+1} = Jp^k - f(p^k) \tag{2.22}$$

31

In the current case, the function that we have to solve is the left hand side of Eqn. 2.21, the Jacobian J can be formulated as

$$J = -L + \frac{\partial M}{\partial p} \qquad (2.23)$$

In this case, the first term of Eqn. 2.21 is not a function of pressure, and L represents the coefficient of pressure in the Laplacian term. It should be noted that since $\frac{\partial M}{\partial p}$ is a part of the Jacobian for the Newton's method, it represents the change in M with respect to the change in pressure from one Newton iteration to another. Hence, this is a diagonal term using values at the same computational point. Substituting Eqn. 2.23 and Eqn. 2.21 into Eqn. 2.22, we get the following

$$\rho \nabla \cdot \phi_v^* - L(p^{k+1}) + M(p^k) + \frac{\partial M}{\partial p} * (p^{k+1} - p^k) = 0 \qquad (2.24)$$

Once this equation is solved for pressure, the velocity is updated and this process is continued till the pressure value is sufficiently converged or the number of iterations exceeds a user input.

The above governing equations and numerical procedure were implemented into the open source CFD library known as OpenFOAM [94] and the final code is called HRMFoam. Fig. 2.1 shows the flowchart of the HRMFoam solver. The "property and flash boiling model calculation module" in the Fig. 2.1 is called "modelCalc". This module updates the properties of the working fluid, and calculates the last term in the Eqn. 2.11. This module links to the classes that perform interpolations in the look-up table for calculating the required properties as a function of pressure and enthalpy. An abstract base class is defined, and the two property interpolation routines: for REFPROP and JP8 properties, are derived classes of this base class. This allows for easier extension of the HRMFoam solver to incorporate other property calculation

routines. Additionally, the switching between the two property interpolation routines is performed at solver run-time and depends on user input.

An important point to be noted is that a new boundary condition was designed for the continuity equation. This boundary condition sets the density of the outgoing flow as zero gradient whereas calculates the density of the incoming flow based on the pressure and enthalpy at that location. In order to calculate this incoming fluid density, the modelCalc module is used.

2.2 Modeling of Gasoline-Ethanol Fuel

In previous work using HRMFoam, curve fits and standard programs from the National Institute of Standards and Technology (NIST) were used to generate the fluid property look-up tables. However these methods are unable to generate mixtures with ethanol due to its high polarity. The current section describes the steps followed in building a new model for properties of gasoline-ethanol blends using a binary mixture approximation based on the idea of Pumphrey et al. [71]. The model developed is known as the Gasoline-Ethanol Flash model (GEFlash), and the following sub-sections present the formulations used to calculate the different properties and the methodology used to combine these sub-models into one framework.

2.2.1 Vapor Pressure

The model of Pumphrey et al. [71] was used to calculate the vapor pressure of the gasoline-ethanol blends. According to this method, the vapor pressure of a gasoline-ethanol blended fuel can be obtained by Eqn. 2.25

$$P_{vap} = x_e \gamma_e P_{e,vap} + x_g \gamma_g P_{g,vap} \tag{2.25}$$

where the subscripts e and g stand for ethanol and gasoline respectively. The variables x, γ, P_{vap} represent the molar fractions, the activity coefficients, and vapor pressure

33
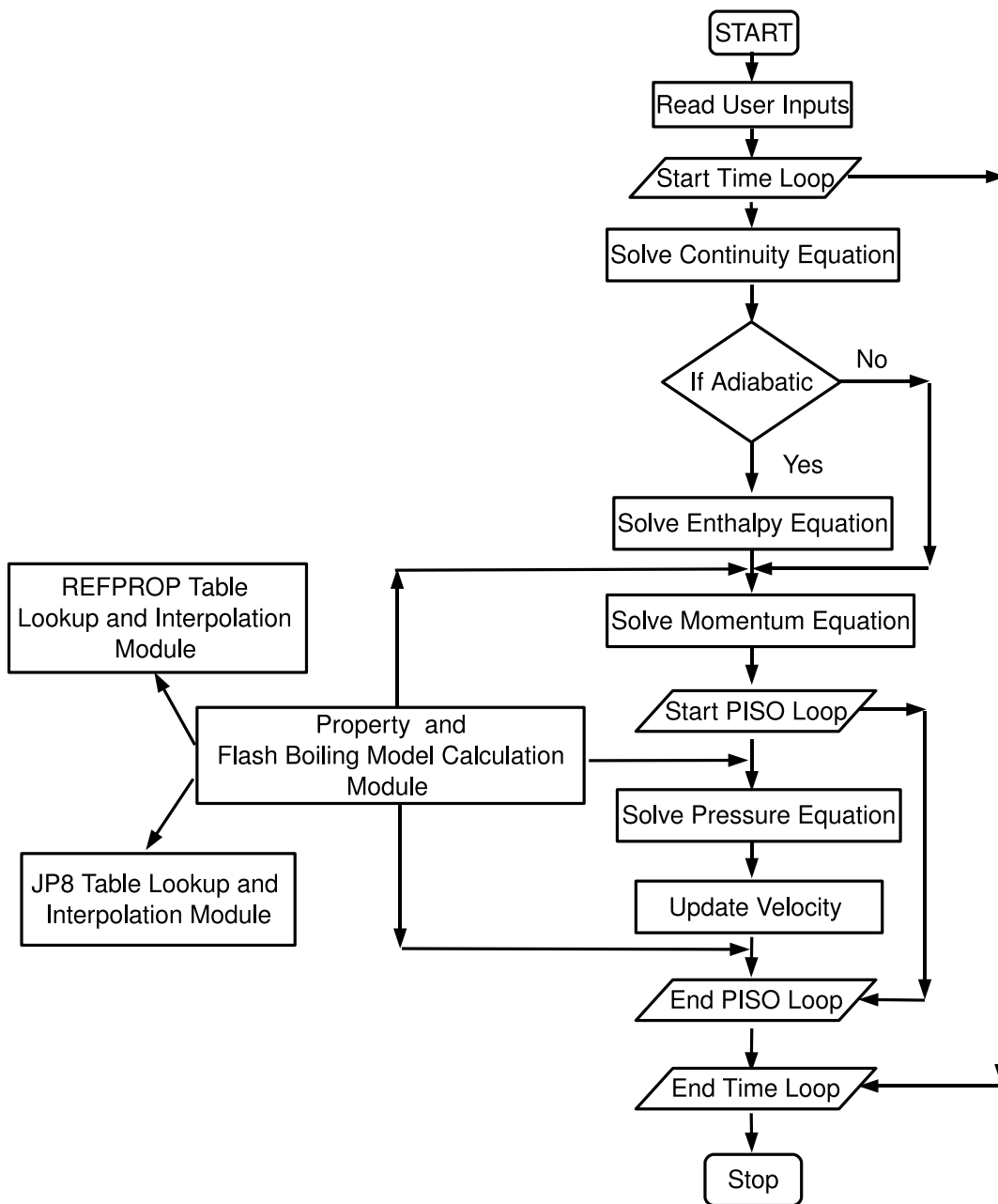
Figure 2.1. Flowchart for the HRMFoam solver
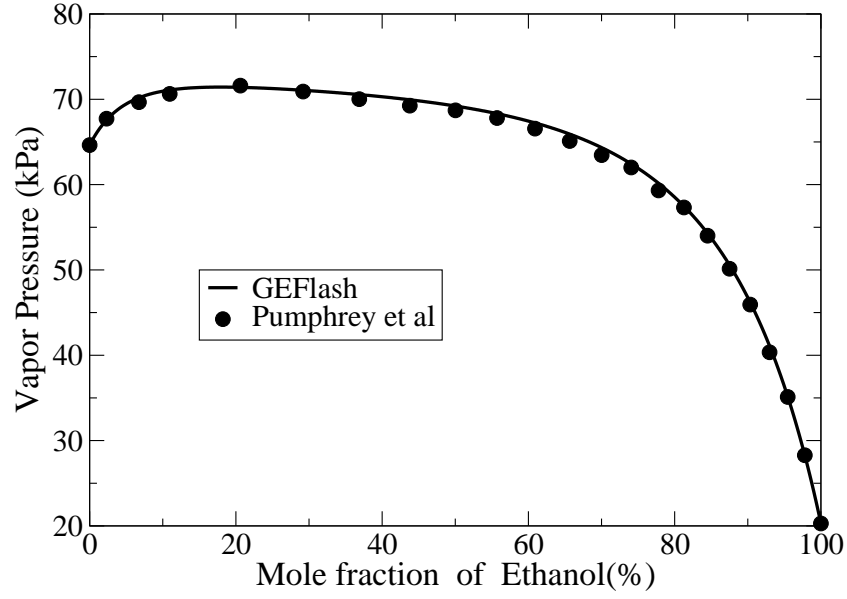
Figure 2.2. Comparison of the vapor pressure calculations with experimental data of Pumphrey et al.[71]

of the component respectively. The activity coefficients were calculated using the Wilson equation formulation [73] given as follows

$$ln(\gamma_e) = -\ln(x_e + \Lambda_{eg}x_g) + x_g\Big(\frac{\Lambda_{eg}}{x_e + \Lambda_{eg}x_g} - \frac{\Lambda_{ge}}{x_g + \Lambda_{ge}x_e}\Big) \qquad (2.26)$$

$$ln(\gamma_g) = -\ln(x_g + \Lambda_{ge}x_e) - x_e\Big(\frac{\Lambda_{eg}}{x_e + \Lambda_{eg}x_g} - \frac{\Lambda_{ge}}{x_g + \Lambda_{ge}x_e}\Big) \qquad (2.27)$$

The parameters Λ_{eg} and Λ_{ge} were obtained by Pumphrey et al from their experimental data as equal to 0.1665 and 0.3527 respectively. This method was implemented in this work and Fig. 2.2 is a verification that the implementation is accurate.

2.2.2 Enthalpy of Vaporization

The Clausius-Clapeyron equation was used by Kar et al.[41] and Balabin et al. [8] to calculate the enthalpy of vaporization of the gasoline-ethanol blends. This method

can be explained as follows. The Clausius-Clapeyron equation for pure substances is given as

$$\frac{dP_{sat}}{dT_{sat}} = \frac{H_{fg}}{T_{sat}\nu_{fg}} \tag{2.28}$$

where P_{sat} and T_{sat} are the saturation pressure and temperature of the liquid, H_{fg} is the enthalpy of vaporization, and ν_{fg} is the difference in the specific volumes of saturated liquid and vapor. Assuming that the specific volume of the liquid is negligible as compared to that of vapor and also that the ideal gas equation is valid for the vapor phase, we get the following

$$\frac{d(ln(P_{sat}))}{d(1/T_{sat})} = -\frac{H_{fg}}{R} \tag{2.29}$$

where R is the gas constant. From the slope of the plot of $ln(P_{sat})$ versus $1/T_{sat}$, the enthalpy of vaporization can be obtained. This method has been found to be accurate for pure ethanol and distilled water, and it is proposed by Kar et al. that it may give a good estimate for gasoline-ethanol blends over a narrow temperature range. In the current work, the left hand side of the Eqn. 2.29 is calculated by a simple first order Taylor series expansion. The vapor pressure is obtained from the code developed in the previous subsection.

Though the use of the ideal gas assumption is not strictly valid for multi-component modeling of non-ideal mixtures, this is the only known method that has been used to predict the enthalpy of vaporization for all gasoline-ethanol blends.

2.2.3 Saturated Liquid and Vapor Densities

Two different methods were tested to calculate the saturated liquid density of the blended fuel. The first method involves the solution of cubic equation of states (CEOS) for the molar volume and using the highest and the lowest root values as

Table 2.1. Parameters for five cubic EOS

EOS	u	w	b	a
Redlich-Kwong(RK) [73]	1	0	$\frac{0.08664RT_c}{P_c}$	$\frac{0.42748R^2T_c^{2.5}}{P_cT^{1/2}}$
Soave-RK [73]	1	0	$\frac{0.08664RT_c}{P_c}$	$\frac{0.42748R^2T_c^2}{P_c}[1+fw(1-T_r^{1/2})]^2$ where $fw = 0.48 + 1.574\omega - 0.176\omega^2$
Peng-Robinson [73]	2	-1	$\frac{0.07780RT_c}{P_c}$	$\frac{0.45724R^2T_c^2}{P_c}[1+fw(1-T_r^{1/2})]^2$ where $fw = 0.37464 + 1.54226\omega - 0.26992\omega^2$
Peng-Robinson-Gasem(PRG)[30]	2	-1	$\frac{0.07780RT_c}{P_c}$	$\frac{0.45724R^2T_c^2}{P_c}exp((2.0+0.836T_r)(1-T_r^{fw})$ where $fw = 0.134 + 0.508\omega - 0.0467\omega^2$
Peng-Robinson-Stryjek-Vera(PRSV) [88]	2	-1	$\frac{0.077796RT_c}{P_c}$	$\frac{0.457235R^2T_c^2}{P_c}[1+fw(1-T_r^{1/2})]^2$ where $fw = K0 + K1(1+T_r^{1/2})(0.7-T_r)$ And $K0 = 0.3789 + 1.4897\omega - 0.1713\omega^2 + 0.0196\omega^3$

the vapor and liquid molar volumes respectively. The third root has no physical significance and is discarded. A cubic equation of state can be described by

$$P = \frac{RT}{V-b} - \frac{a}{V^2 + ubV + wb^2} \tag{2.30}$$

where R is the gas constant, T is the temperature and V is the molar volume. The variables u and w are integer values which are different for different equations of state. The parameter b accounts for the fact that molecules cannot overlap, and a accounts for the attraction between molecules. The value of these four parameters are mentioned in Table 2.1 for some commonly used cubic equations of state.

In the Table 2.1, T_c and P_c are the critical temperature and pressure, T_r represents the reduced temperature, and $K1$ is an empirical constant that needs to be specified for the PRSV equation. The variable ω is known as the accentric factor and represents the non-sphericity of the molecule. The accentric factor is mostly obtained from empirical observations [73].

When the CEOS are to be applied to mixtures, the parameters b and a need to be specified by using mixing rules. In this work, the traditional van der Waals one-fluid mixing rule was used which gives the parameters as follows

$$a_m = \sum_i \sum_j x_i x_j a_{ij} \tag{2.31}$$

$$b_m = \sum_i \sum_j x_i x_j b_{ij} \tag{2.32}$$

where, i and j represent the molecular species. In the above equations, a_{ii} and b_{ii} can be calculated from the formulas for single components given in Table 2.1. The other terms, namely, a_{ij} and b_{ij} can be calculated as a combination of the single component parameters by the following formulas

$$a_{ij} = \sqrt{a_{ii}a_{jj}}(1 - k_{ij}) \tag{2.33}$$

$$b_{ij} = \frac{b_{ii} + b_{jj}}{2} \tag{2.34}$$

here, k_{ij} is the binary interaction parameter which is characteristic of each binary pair and needs to be obtained from experimental data. In this work, the value of the binary interaction parameter is taken as zero. The main reason for this assumption is that since the vapor pressures were obtained from the Wilson equation, whose parameters were already adjusted to match experimental data, the CEOS is indirectly affected by experimental data. Adding requirements for additional data were not desirable since such data are difficult to obtain for G-E blends.

The second method for calculating the saturated liquid density was the modified Rackett equation [73]. In this method, the molar saturated liquid volume is given as follows

$$V_m = R(\sum_i \frac{x_i T_{ci}}{P_{ci}}) Z_{RAm}^{[1+(1-T_r)^{2/7}]} \tag{2.35}$$

$$Z_{RAm} = \sum_i (x_i Z_{RAi}) \tag{2.36}$$

where, T_r in this case is given as

$$T_r = T/T_{cm} \tag{2.37}$$

38

T_{cm} is obtained from mixing rules. Spencer and Danner [87] recommended the Chueh-Prausnitz mixing rules which are given as follows

$$T_{cm} = \sum_i \sum_j \phi_i \phi_j T_{cij} \tag{2.38}$$

$$\phi_i = \frac{x_i V_{ci}}{\sum_i x_i V_{ci}} \tag{2.39}$$

$$T_{cij} = (1 - k_{ij})(T_{ci}T_{cj})^{1/2} \tag{2.40}$$

$$1 - k_{ij} = \frac{8(V_{ci}V_{cj})^{1/2}}{(V_{ci}^{1/3} + V_{cj}^{1/3})^3} \tag{2.41}$$

where V_c is the critical volume and Z_{RA} is a constant known as the Rackett compressibility factor. Reid [73] provides the value of this constant for a number of elements. The saturated vapor densities were always calculated from the equation of state solution, even when the liquid density was obtained from the modified Rackett equation.

The model was applied to a non-ideal methanol-toluene mixture. The Wilson equation parameters for this mixture were obtained from the DECHEMA chemistry data series [31]. Again, to verify that the implementation of the Wilson equation is accurate, the vapor-liquid equilibrium predictions are compared with the data of Oh et al.[66] in Fig. 2.3. The Fig. 2.3(b) also shows the plot if the ideal Raoult's law is used instead of the Wilson equation. This gives an idea of the non-ideal nature of the mixture.

Once the Wilson equation parameters were implemented and the correct vapor pressures were obtained for the mixture, the density of the binary mixture was calculated by the different implemented models and compared against the data of Nikam et al [63] in Fig. 2.4. It can be seen that the the liquid density predictions of the modified Rackett equation are closest to the experimental data and hence this method was used for modeling gasoline ethanol blends as well. All the required constants for
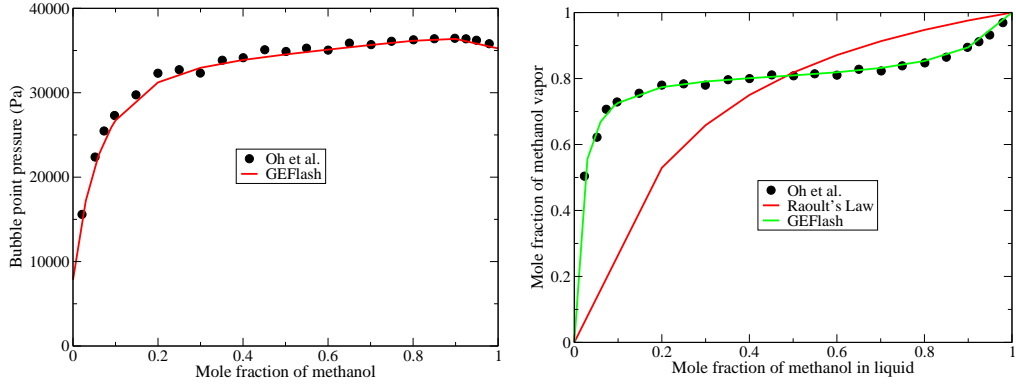
(a) Variation of vapor pressure with mole fraction of methanol

(b) Variation of liquid versus vapor mole fraction of methanol

Figure 2.3. Comparison of vapor-liquid equilibrium predictions from GEFlash with experimental data of Oh et al [66] for the methanol-toluene mixture at 40^oC

methanol and toluene: the critical temperature, pressure and volume, the accentric factor, and the Rackett equation compressibility, were obtained from Reid et al. [73]. The constant $K1$ (see table 2.1) is obtained from Stryjek and Vera [88]. The most accurate CEOS for the liquid for the liquid density predictions was the PRSV equation, so this was used for predicting the vapor density of the gasoline-ethanol blends.

2.2.4 Mole Fraction of Vapor

The mole fraction of vapor (v) was obtained by the Rachford-Rice equation which is given by Eqn. 2.42

$$\sum \frac{z_i(K_i - 1)}{1 + v(K_i - 1)} = 0 \tag{2.42}$$

where z is the mole fraction of component i and K is given as

$$K = \frac{\gamma_i * (P_{sat}^i)}{P} \tag{2.43}$$
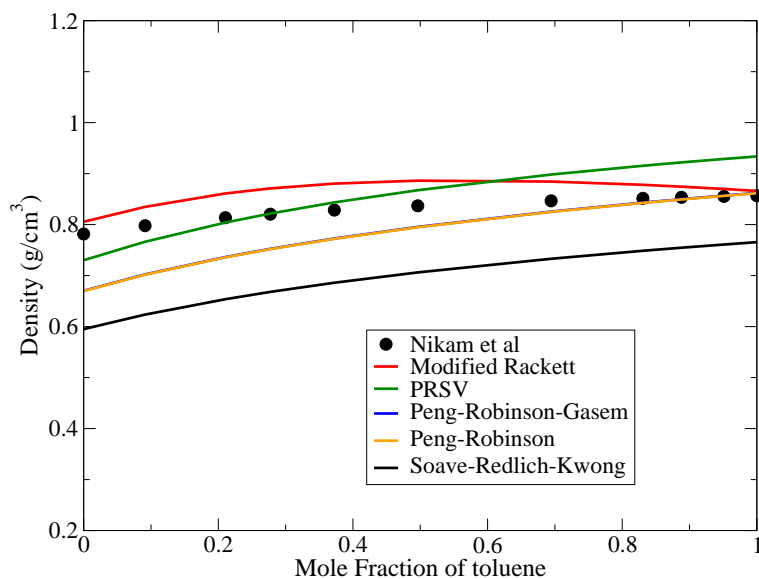
Figure 2.4. Comparison of liquid density predictions from GEFlash with the experimental data of Nikam et al. [63] for the methanol-toluene mixture at 30^oC

where γ_i and P_{sat}^i are the activity coefficient and saturation pressure of the component i respectively and P is the pressure in the system. The Eqn. 2.42 was solved using the Newton's method to get the value of mole fraction of vapor.

In order to validate these predictions, a plot of temperature versus the percent mole/mass fraction of fuel vaporized is needed. Usually, in presenting distillation data of this nature, the temperature is plotted against the percent volume of fuel distilled, which is equal to the volume of the liquid obtained by condensing the vapor exiting the distillation flask. The GEFlash model provides the mole fraction of vapor obtained from distillation and does not include a mechanism to calculate the volume of the liquid obtained from condensing this vapor. Since GEFlash cannot provide this liquid volume, a different method of validation was employed. A model for G-E blends was built in the chemical process engineering software Aspen Plus and was used to validate the GEFlash predictions. The full modeling procedure is explained in Section 2.2.6.

2.2.5 Final Setup of GEFlash Model

Finally, the above mentioned submodels were combined to calculate the required properties and the final flow chart for the GEFlash model is shown in Fig. 2.5. Note that the HRMFoam flow solver requires the properties to be specified as functions of pressure and enthalpy rather than temperature and so the GEFlash model was formulated accordingly. The different steps in the flow chart are explained as follows

1. The pressure and enthalpy values at which the properties are required are read in from an input file.

2. Since only the enthalpy is available, the temperature corresponding to the enthalpy is required. An initial temperature value is estimated and the loop starts.

3. For the estimated temperature, the vapor pressure is calculated from Eqn. 2.25, and the dew point is calculated from the modified Raoult's law as follows

$$P_{Dew} = \frac{1}{\sum(\frac{x_i}{\gamma_i P_{vap}^i})} \qquad (2.44)$$

4. The enthalpy of vaporization is calculated from the Clausius-Clapeyron equation, Eqn. 2.29.

5. The liquid enthalpy H_{liq} is calculated by

$$H_{liq} = C_p(T - T_{ref}) + H_{ref} \qquad (2.45)$$

where, the reference enthalpy H_{ref} and corresponding reference temperature T_{ref} are user inputs. It should be noted that enthalpy is relative and so H_{ref} can be set to any value. The specific heat for gasoline and ethanol have been taken to be equal to 2.13 J/K/g and 2.38 J/K/g respectively, which are the values at 20 ^oC obtained from Nan et al. [59]. The specific heat of the mixture is calculated

42
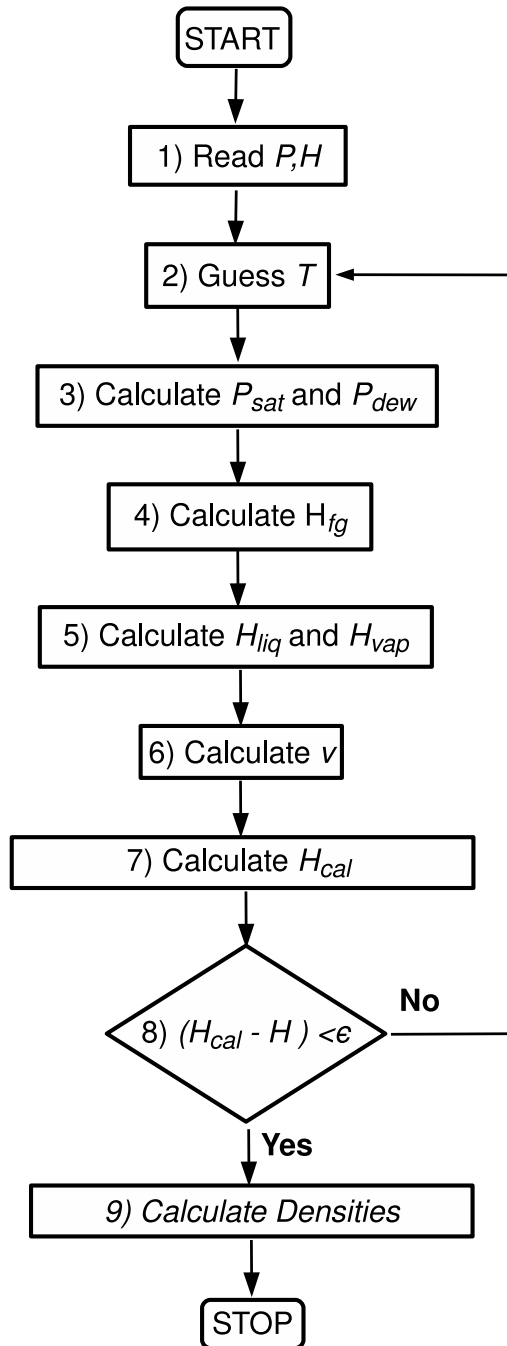
Figure 2.5. Flow chart for the GEFlash code

by adding these two values proportioned by the respective mole fractions. It is assumed that the specific heats of gasoline and ethanol do not change in the temperature range considered. The vapor enthalpy H_{vap} is calculated from the liquid enthalpy and H_{fg}.

6. The mole fraction of vapor is calculated from the Rachford-Rice equation, Eqn. 2.42. It should be noted that this step itself includes an iterative solution based on the Newton's iteration method.

7. The enthalpy obtained for the initially estimated temperature is calculated as

$$H_{cal} = H_{liq} + v H_{fg} \qquad (2.46)$$

8. If the difference between this enthalpy and the user input in step 1 is less than a certain tolerance, the loop is ended, else, the solution proceeds from step 2.

9. Based on the converged temperature and the vapor pressure, the liquid and vapor densities are calculated from the modified Rackett equation, Eqn. 2.35, and the PRSV CEOS respectively.

The temperature loop in the above algorithm uses the bisection method to find the temperature. The required inputs for GEFlash and the format of the input and output files are given in Appendix A.

2.2.6 Aspen Plus for Gasoline-Ethanol Fuel Blends

Aspen Plus is a software that is distributed by AspenTech and is used for modeling chemical engineering processes. As mentioned in section 2.2.4, this software was used in this work to obtain the properties of gasoline-ethanol blends in order to validate the predictions of GEFlash. Firstly, the process followed for obtaining the properties for water will be explained in detail followed by the method for modeling the gasoline-ethanol blends

2.2.6.1 Model for Water

The model used for water is shown in Fig. 2.6. It includes an input liquid stream flowing into a flash drum, which separates the stream into vapor and liquid depending on the conditions in the drum. In order to check the validity of this method for obtaining the properties, the model for water was coupled with the HRMFoam solver to simulate the test cases of Reitz [74]. This coupling was achieved by generating a look-up table using Aspen Plus which would be then used by the HRMFoam solver to obtain the properties of water. In order to generate the look-up table, a sensitivity analysis was performed in Aspen Plus. This kind of analysis allows the user to modify certain model variables and observe the effect on other variables. In this case, the sensitivity analysis involves modifying the temperature of the input stream and the pressure in the flash drum. This process is shown in the Fig. 2.7. The temperature range of the input stream and the pressure range in the flash drum govern the size of the look-up table. The temperature of the input stream is varied instead of the temperature in the flash drum because the HRMFoam solver requires properties to be specified as a function of enthalpy, so the flash drum will perform an adiabatic flash operation from the conditions of the input stream to the pressure specified in the drum. The NRTL(non-random two liquid) base property method was used which uses the NRTL model for calculating the liquid phase activity coefficient and the ideal gas approximation for the vapor phase. The NRTL model is an activity coefficient model similar to the Wilson equation (see [73]). The liquid volume was calculated by the VL2Quad method (liquid volume calculated by quadratic mixing rules from pure component liquid volumes) because this method was found to be accurate in predicting the density of water. Finally, the look-up table was copied from Aspen Plus and pasted into a word processing software, and the format of the table was adjusted according to the requirements of the HRMFoam solver. The Fig. 2.8 shows the comparison between the results obtained for the test cases of Reitz [74] using
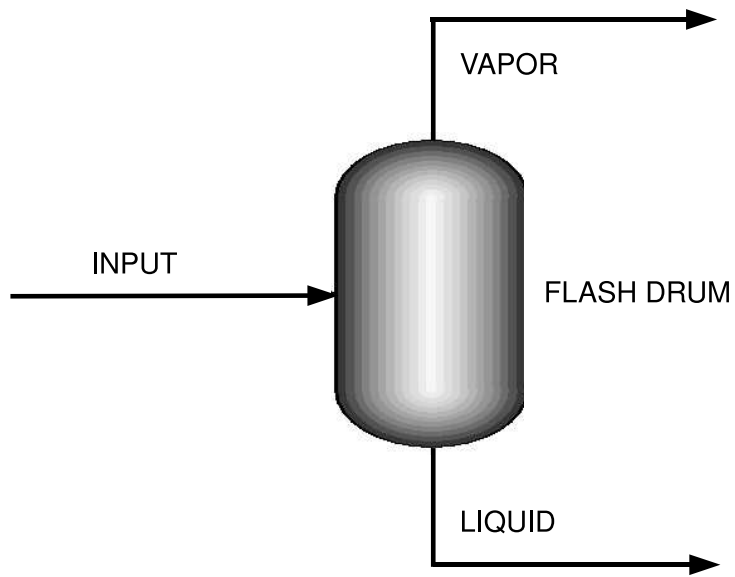
Figure 2.6. Model for water in Aspen Plus
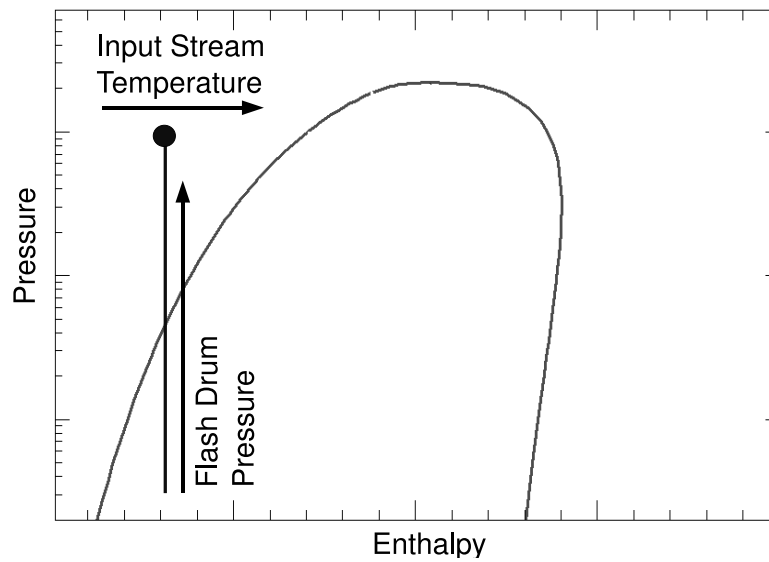
Figure 2.7. Sensitivity analysis settings used in Aspen Plus for generating look-up table for water
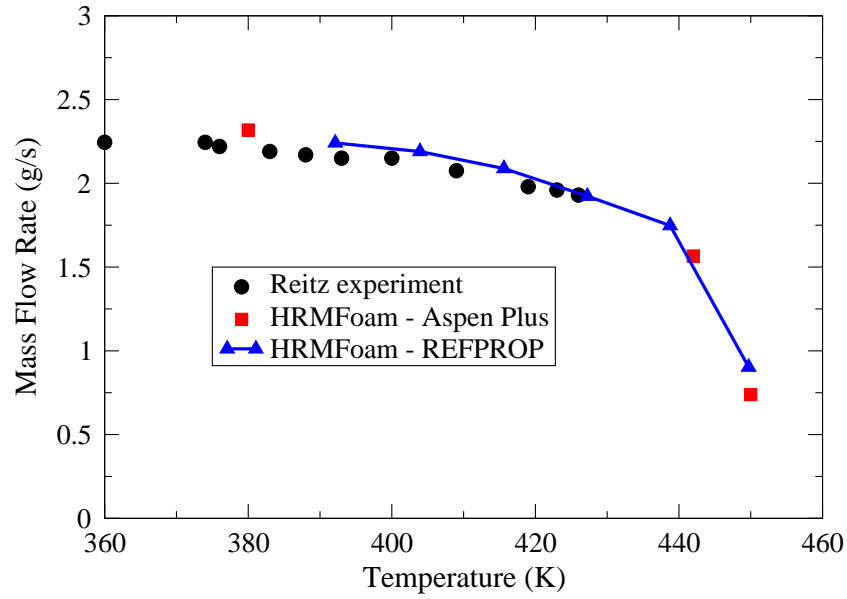
Figure 2.8. Comparison between predictions of HRMFoam using the look-up tables from Aspen Plus and REFPROP in simulating the experiments of Reitz [74]

HRMFoam with the look-up tables from Aspen Plus and from REFPROP. It can be seen from Fig. 2.8 that the predictions are quite close, hence, it is concluded that the model proposed for obtaining the properties of water is satisfactorily accurate. However, it is to be noted that Aspen Plus was found to crash if a very large table was generated. Hence the look-table used for these simulations was very sparse as compared to the REFPROP table, leading to higher interpolation error. Additionally, instead of generating one table that covered the entire range of temperatures required for the validation shown in Fig. 2.8, three separate tables had to be used for the three cases simulated due to the table size limit. Hence it must be noted that due to the difficulty in using Aspen Plus to generate the required look-up tables, this method will merely be used for validation of the GEFlash model rather than for running flash boiling simulations using HRMFoam.

47
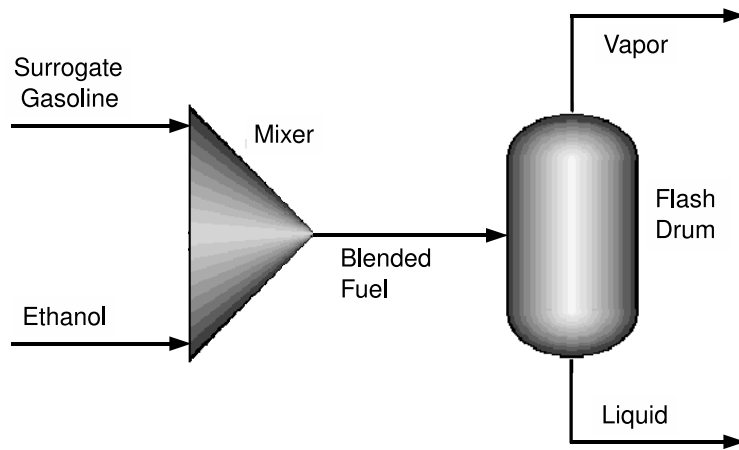
Figure 2.9. Model for gasoline-ethanol blend in Aspen Plus

2.2.6.2 Model for Gasoline-Ethanol Fuel

The model used for the gasoline-ethanol fuel is similar to the model for water, with an input stream consisting of liquid fuel flowing into the flash drum where it is separated into liquid and vapor. However, there is an additional stage in which a stream of ethanol is mixed with a stream of a gasoline surrogate in a mixer. This model is shown in Fig. 2.9. By changing the volume fraction of ethanol and surrogate gasoline flowing into the mixer, the type of gasoline-ethanol blend can be changed. If this model was to be coupled with HRMFoam, the method for conducting the sensitivity analysis to generate a look-up table for gasoline-ethanol blends would be the same as that for the water model, the only difference being that the temperature of the "blended fuel" stream would govern the temperature range of the look-up table. The next step in modeling the gasoline-ethanol fuel was to select an appropriate surrogate for gasoline.

Table 2.2. Formulation of gasoline surrogates [20]

Component	Indolene model (% mass)	Synthetic fuel model (% mass)
iso-pentane	16.18	16.61
cyclo-hexane	20.91	24.05
iso-octane	16.70	19.2
toluene	15.35	17.65
ethyl-benzene	15.59	12.93
n-decane	11.71	8.47
naphtalene	3.55	1.09

2.2.6.3   Surrogate for Gasoline

Curtis et al. [20] presented 7-component surrogates for three different fuels, namely, a hesitation fuel with high driveability index, indolene fuel and a synthetic fuel which had a D86 distillation curve [1] and a driveability index similar to a California Phase II fuel. The synthetic fuel and indolene surrogates were built in Aspen Plus and these formulations are shown in Table 2.2.

The Fig. 2.10 shows a comparison of the D86 distillation curves obtained from Aspen Plus with the experimental D86 curves presented by Curtis et al.[20]. In addition, the D86 curve for a refinery gasoline produced in Brazil and known as "Type A" gasoline [89] is also plotted. It can be observed that the D86 curves from Aspen Plus reproduce their respective experimental D86 curves very well. Overall, a maximum difference of approximately 7 % is observed between the two D86 curves obtained from Aspen Plus and the "Type A" gasoline. In both cases, the root mean square error is approximately 13 K. Since there is not much difference between the two models, the indolene model is chosen for further analysis.

It is assumed in both, the GEFlash method and the Aspen Plus model mentioned above, that the volumes of ethanol and gasoline are additive. For example, it is assumed that 0.2 m^3 of ethanol mixed with 0.8 m^3 of gasoline gives 1 m^3 of blended fuel E20. This assumption is inaccurate since volumes are not additive. In order
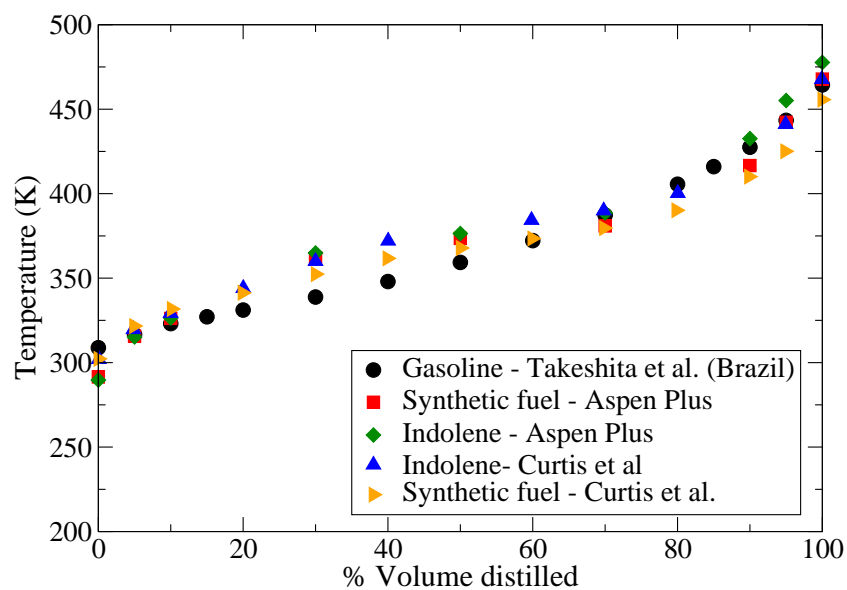
Figure 2.10. Comparison of D86 distillation curves of the surrogate gasolines from Aspen Plus with the experimental data of Curtis et al. [20], and the experimental data of Takeshita et al. [89]
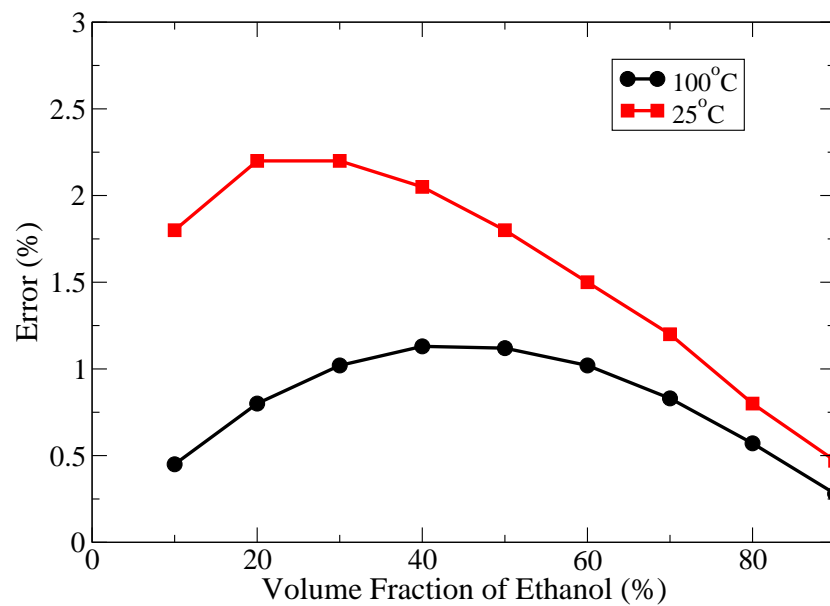
Figure 2.11. Error due to assumption of additive volumes plotted against the volume fraction of ethanol in the mixture

to check the validity of this assumption, the error is plotted in Fig. 2.11 for two temperatures. The error is calculated as follows

$$Error = \frac{|V_{act} - V_{add}|}{V_{add}} * 100 \tag{2.47}$$

where V_{act} is the actual volume of the blend obtained from the Aspen Plus simulation and V_{add} is the volume based on the assumption that the volumes are additive.

It can be seen from Fig. 2.11 that the maximum error for the two temperatures tested is at 25^oC and is equal to 2.2 % occurring at around 20 % ethanol. This means that at 25^oC, the fuel denoted as E20 can have 20 ± 2.2 % ethanol by volume. However, since flash boiling cases operate at much higher temperatures than 25^oC, it can be expected that the error will be much lower.

CHAPTER 3
RESULTS

3.1 Gasoline-Ethanol Fuel Modeling Results

3.1.1 Vapor Pressure

The vapor pressure predictions from the GEFlash model were compared to the experimental data of Kar et al.[41]. In this case, the pure component vapor pressures required in Eqn. 2.25 were obtained from the vapor pressure plot of Kar et al. The results are shown in Fig. 3.1 along with the predictions from the Aspen Plus model. It can be seen that the GEFlash model excels at matching the vapor pressures of the gasoline-ethanol blends. In this plot, the densities of ethanol and gasoline used to convert from mole fraction to volume fraction were 790.4 and 767 kg/m^3 respectively, taken from the paper by Kar et al. These densities of pure ethanol and gasoline were later calculated using the Rackett equation and it was found that the change in Fig. 3.1 was negligible.

The Aspen Plus predictions match the experimental data well in the region with low ethanol content. They also accurately capture the azeotropic behavior of the blended fuel with 10-20 % volume fraction of ethanol. However, the predictions deviate as the ethanol content increases. In fact, it is seen that the pure component ethanol vapor pressures predicted by Aspen Plus do not match the experimental data. So, pure component ethanol vapor pressure predictions using the equation proposed by Dillon and Penoncello [23] as implemented in the REFPROP program are also plotted in Fig. 3.1. It can be seen that the Aspen Plus predictions match the REFPROP predictions but the experimental data shows lower vapor pressures.
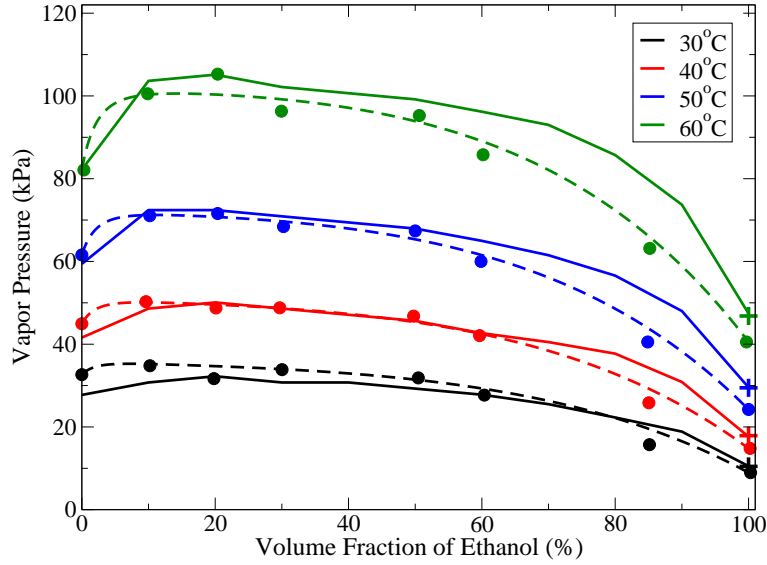
Figure 3.1. Comparison of gasoline-ethanol fuel vapor pressures predicted by GEFlash with data from Kar et al. [41] and predictions of Aspen Plus. Dashed lines represent GEFlash results, solid lines represent Aspen Plus predictions and symbols represent experimental data

In order to further validate the pure ethanol vapor pressure predictions, the results from REFPROP are compared with the experimental data of Nasirzadeh et al.[60] in Fig. 3.2. It can be seen that the REFPROP predictions are extremely accurate in the same temperature range as the experiments of Kar et al. It is mentioned in the work of Kar et al that the ethanol used was denatured by adding 2 % methanol and that inspite of this, the vapor pressure of ethanol agreed with published data for pure ethanol. However, from Figs. 3.1 and 3.2 it is hypothesized that the vapor pressure of the denatured ethanol may be slightly different from the pure ethanol.

3.1.2 Enthalpy of Vaporization

The comparison between the predictions of Kar et al and the current implementation are shown in Fig. 3.3. It is observed that the overall trend is satisfied but the predictions are inaccurate in the azeotropic region (around 20 % ethanol). This is
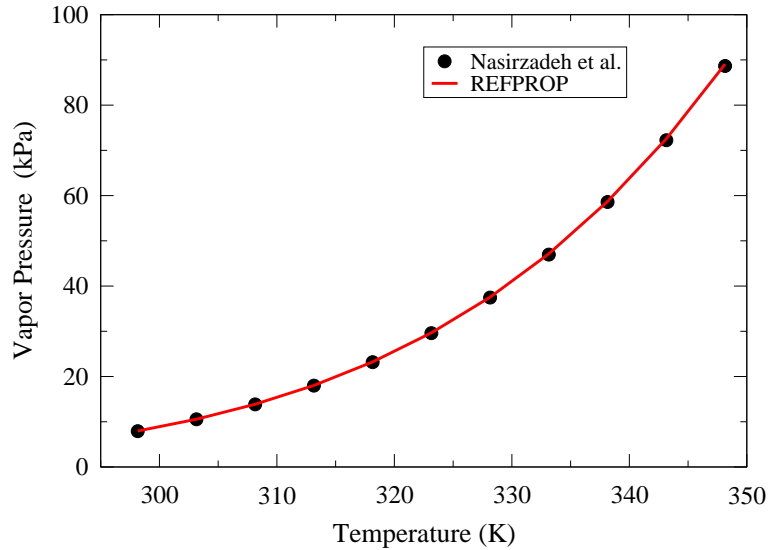
Figure 3.2. Comparison of pure ethanol vapor pressure predictions of REFPROP with data of Nasirzadeh et al. [60]

due to the small deviations between the predicted and experimental vapor pressures in this region as seen in Fig. 3.1

3.1.3   Saturated Liquid Density

The density predictions from the GEFlash and Aspen Plus models are compared with the experimental data of Takeshita at al. [89] in Fig. 3.4. It is seen that the density predictions from GEFlash deviate from the experimental data close to the pure gasoline section, with the maximum error being 4.6%. The main reason for this deviation is that the Rackett compressibility, molecular weight and the critical properties for gasoline were taken to be equal to those of iso-octane. To further investigate this result, the density predictions from GEFlash are compared, in Fig. 3.5, to the data of Kretschmer et al.[47] for a mixture of iso-octane with ethanol. The maximum error in this case is 2.6% and occurs at 0 ^{o}C and around 0.4 mole fraction ethanol. This shows that the liquid density prediction for G-E blends are closer to the densities of iso-octane-ethanol mixtures. Hence, the assumption that gasoline is similar to iso-octane in the modified Rackett equation causes the deviation in the

54
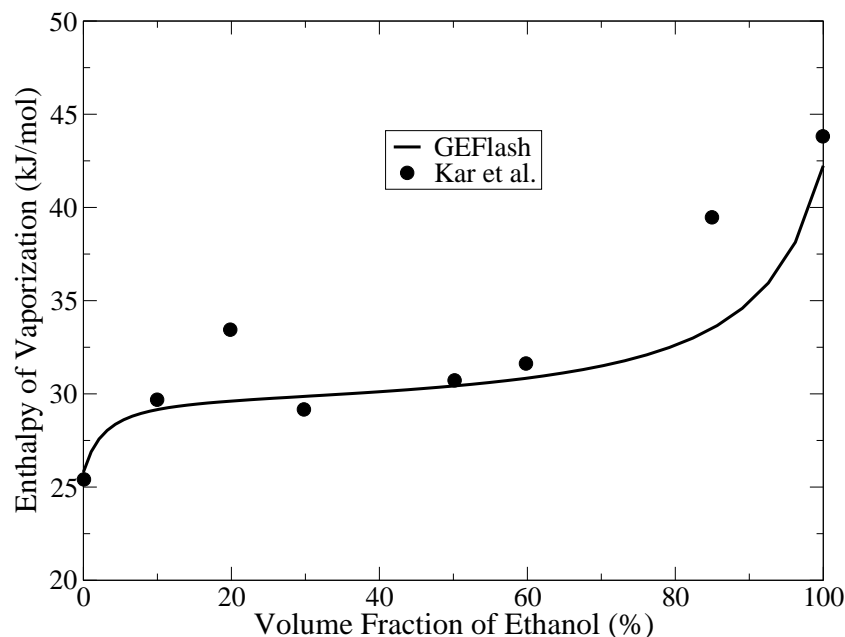
Figure 3.3. Comparison of enthalpy of vaporization predictions with calculations of Kar et al. [41]

prediction of liquid density in Fig. 3.4. It is to be noted here that methods more suited to mixtures of alcohols and hydrocarbons like the cubic plus equation of state [97] may also be used in place of the modified Rackett equation, however, it is seen from Fig. 3.4 and Fig. 3.5 that the saturated liquid density is not a very strong function of mole fraction of ethanol. Hence a simple method is considered to be satisfactory. Additionally, the worldwide variation in properties and composition of gasoline does not guarantee any improvement in predictions with a more complicated model.

For the Aspen Plus model also, the predictions are good for blends with higher ethanol (greater than 50%), but deviate in the region of pure gasoline. The maximum error occurs in the pure gasoline section and is equal to 4.5%. Such variations are expected since the density of a pure, Brazilian-made gasoline is compared with that of a surrogate, which was designed to match the distillation curve of indolene.
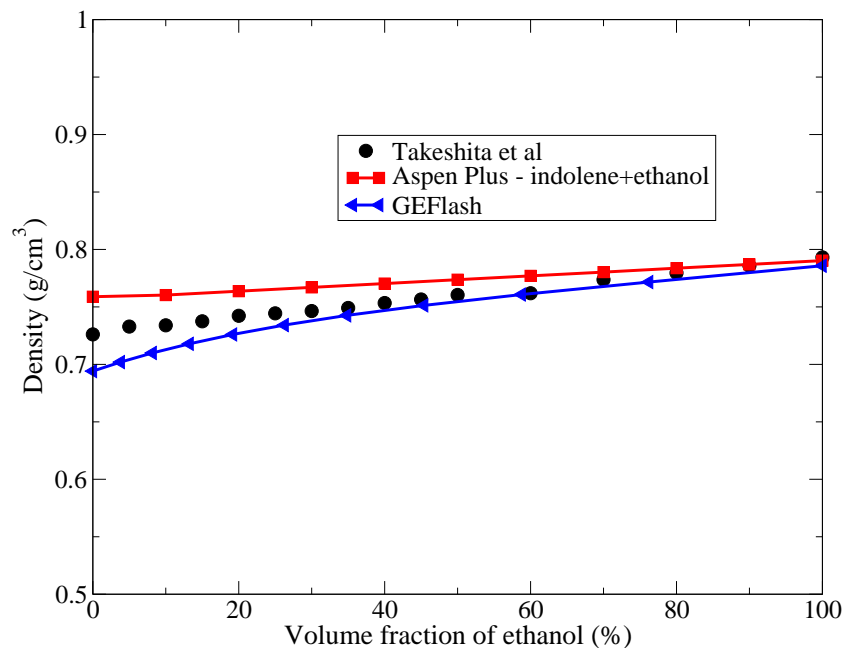
Figure 3.4. Comparison of liquid density of gasoline-ethanol fuels predicted by GEFlash with experimental data of Takeshita et al. [89] and predictions of Aspen Plus for the indolene-ethanol mixture
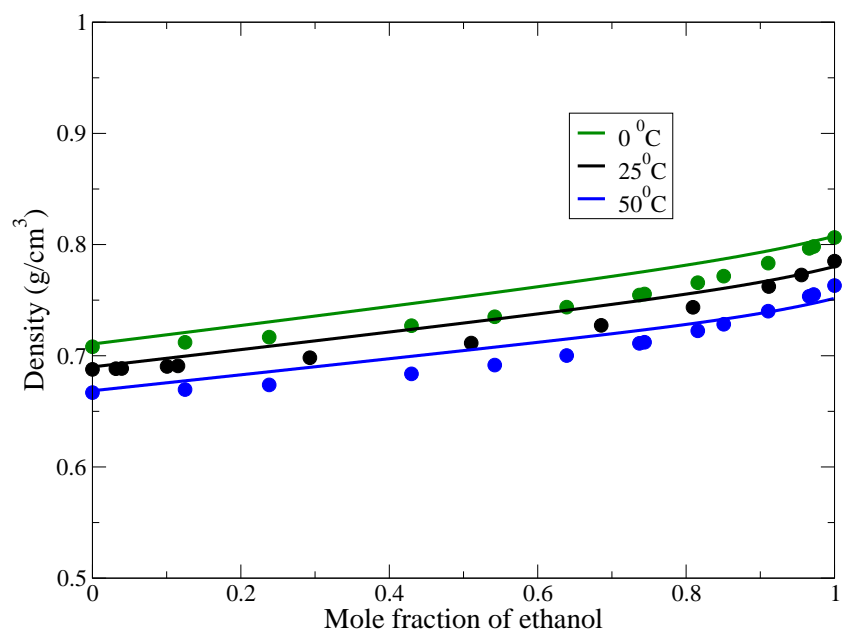
Figure 3.5. Comparison of liquid density of an iso-octane-ethanol mixture predicted by GEFlash (solid line) with the experimental data of Kretschmer et al. [47]

3.1.4 Mole Fraction of Vapor

As mentioned in the previous section, to perform validations of the vapor mole fraction, the Aspen Plus model was used instead of experimental data. However, it was first necessary to check that the Aspen Plus model satisfactorily reproduced the experimental D86 curves for the gasoline-ethanol blends. Fig. 3.6 compares the D86 distillation curves for the different ethanol blends predicted by Aspen Plus with the experimental data of Takeshita et al. From 3.6(a), it is seen that adding 20% ethanol causes the distillation curve to flatten between the distilled volumes of 40 % and 70%. Before and after this section, the curve is almost the same as the pure gasoline case. The prediction from Aspen Plus shows this flattening between these two points but change with respect to the pure indolene curve is not as significant as compared to the experimental data. As the amount of ethanol is increased, the flat section of the experimental data curve becomes longer so that finally, for E80, the distillation curve remains close to 350K from 20% to 90% volume distilled. Although it appears that the Aspen Plus predictions show some of this behavior, the response to the increase in ethanol content is not as strong as the experimental data. One of the causes for this might be the fact that the number of points for the D86 curve provided by Aspen Plus is less than that provided by Takeshita et al. and so it is possible that the area of interest falls between two reported points. Also, it cannot be expected that a surrogate for indolene can reproduce all the properties of a Brazillian gasoline, especially when it is mixed with a polar compound such as ethanol. However, the overall trends predicted by the Aspen Plus model are satisfactory.

In order to compare Aspen Plus predictions with GEFlash results, a sensitivity analysis was performed by keeping the pressure in the flash drum, shown in Fig. 2.9, at 0.5 bar and varying its temperature from 293K to 393K. The mole fraction of vapor was tabulated and the values are plotted against the predictions from GEFlash in Figs. 3.7 and 3.8.
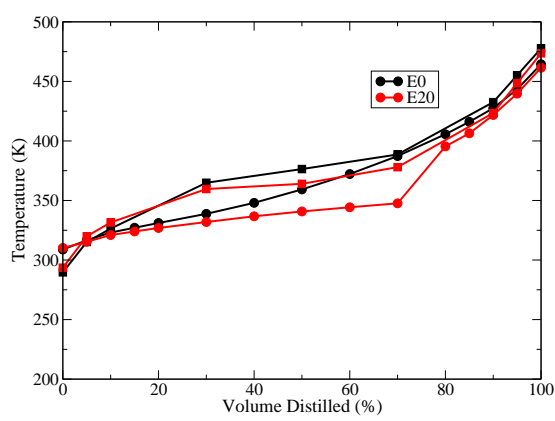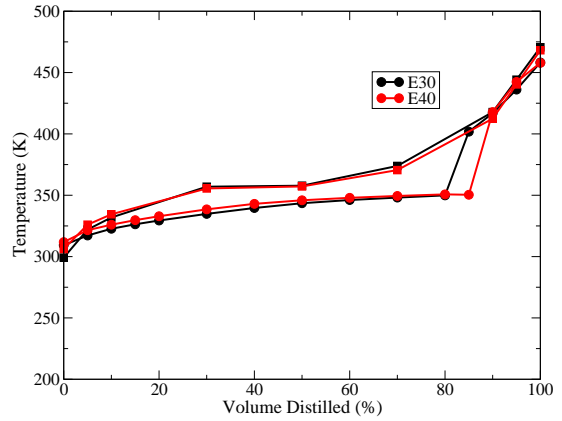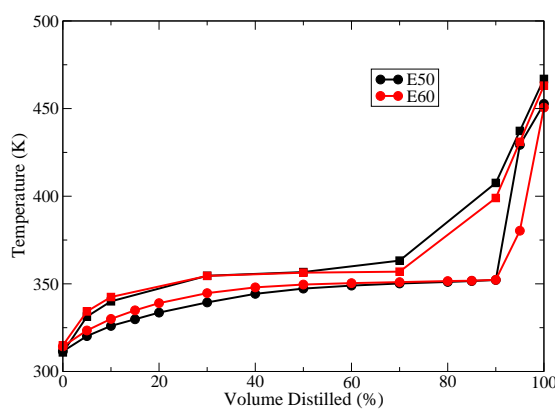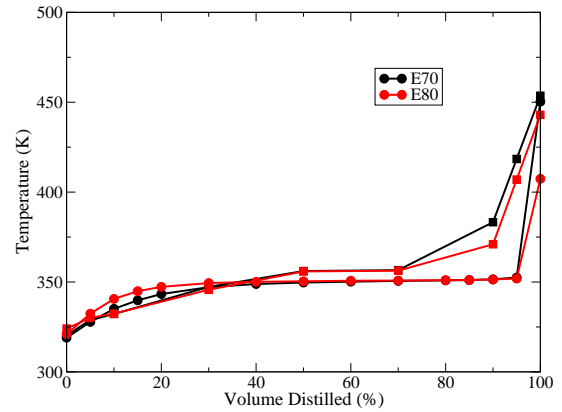
Figure 3.6. Comparison between D86 distillation curves from Aspen Plus and the experimental data of Takeshita et al.[89] for gasoline-ethanol blends. ■ represent Aspen Plus predictions, and ● represent experimental data.
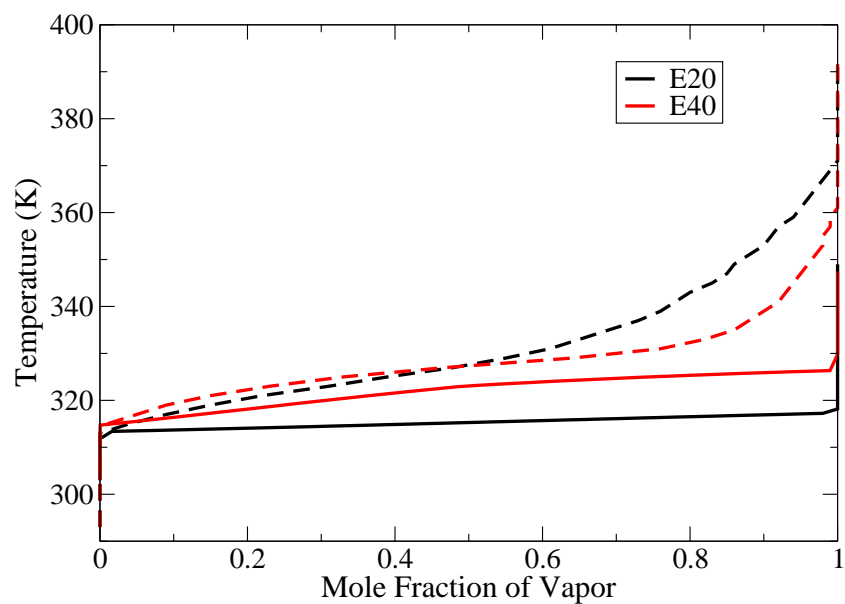
Figure 3.7. Comparison between mole fraction of vapor predicted by GEFlash (solid line) and Aspen Plus (dashed line): E20 and E40
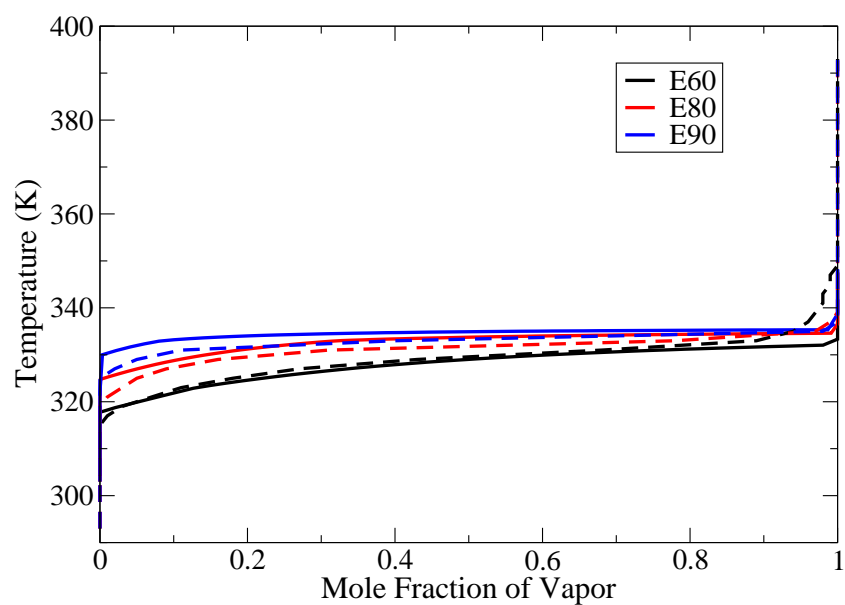
Figure 3.8. Comparison between mole fraction of vapor predicted by GEFlash (solid line) and Aspen Plus (dashed line): E60, E80 and E90

It is seen from the Fig. 3.7 that the GEFlash predictions for E20 do not match the predictions from Aspen Plus over most of the temperature range. However, for 40% ethanol, the trend is reproduced between 0 and 0.7 mole fraction of vapor. Fig. 3.8 shows that, as the ethanol percentage is increased to 60%, the GEFlash predictions seem to reproduce the trends of the Aspen Plus results over majority of the distillation range. For the E60 case, the deviation occurs only after 0.9 mole fraction. Whereas for the blends with higher ethanol content, the deviation occurs even later. The Aspen Plus predictions for the temperatures at which the vapor mole fraction becomes non zero i.e. the bubble points for E80 and E90 are lower than the GEFlash predictions. This is because Aspen Plus predicts a higher vapor pressure for these high ethanol content fuels (see Fig. 3.1) as compared to experiments whereas the GEFlash predictions are more accurate. As a result, the Aspen Plus model shows that vaporization begins at a lower temperature than the GEFlash model.

The main reason for the error in the GEFlash predictions for the lower ethanol content fuels is that since GEFlash is based on a binary component model, it assumes the gasoline to be a single component and hence it cannot capture the boiling of the different fractions in the multi-component gasoline. It is interesting to note that as the ethanol content in the fuel is increased, the predictions from GEFlash start matching the Aspen Plus predictions over a large portion of the distillation range.

3.2   Simulations with n-Hexane

3.2.1   Geometry and Test Conditions

The computational cases simulated here are similar to the experiments performed by Schmitz et al. [81]. Cases were simulated at temperatures of 323K, 343 K, 363 K and 381 K using n-hexane as fuel. An injection pressure of around 8 MPa and a chamber pressure of 50 kPa were used. A high pressure swirl injector was studied (see Fig. 3.9) which converts the high pressure energy of the GDI system into rotational
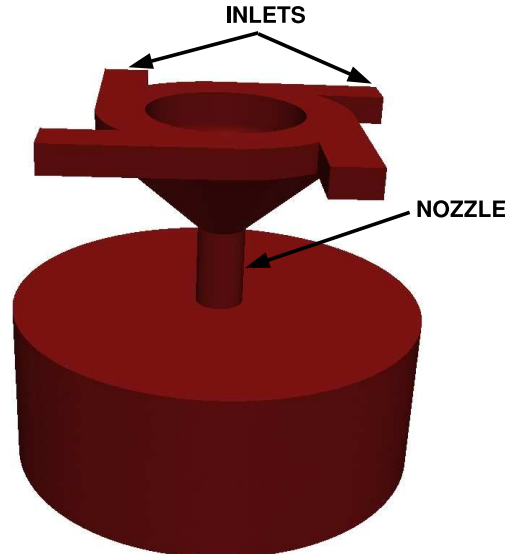
Figure 3.9. Geometry of high pressure swirl injector

momentum thereby enhancing atomization. The highly atomized fuel spray has much smaller droplets that vaporize faster promoting a more homogeneous fuel-air mixture with a significant decrease in UHC emissions. Though all the test conditions were the same as those reported by Schmitz et al., the geometry of the injector had to be estimated since it was not reported in the paper. The high pressure swirl injector geometry used in this study was drafted using estimates of critical dimensions from Alajbegovic et al. [5] and the injector was scaled appropriately to get a fuel flow rate of 15 cm^3/s, which is consistent with the flow rate reported by Schmitz et al. The geometry and the tetrahedral grid used in the current study are shown in Figs. 3.9 and 3.10 respectively. The quad-symmetry of the nozzle was utilized and simulations were done on a 90° section of the geometry as shown in Fig. 3.10.

3.2.2   Results and Discussions

An iso-contour was generated at a void fraction value of 0.8 as shown in the Fig. 3.11. The average radial distance of the outer envelope of this contour was calculated
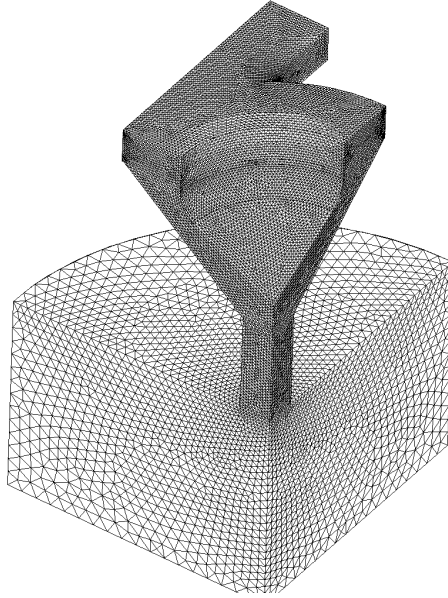
Figure 3.10. Computational mesh used for simulation of high pressure swirl injector

at a plane which was 0.5 mm from the nozzle exit. Finally, the spray cone angle was measured as shown in the Fig. 3.11. The method of fitting regression lines to the spray contours, similar to Schmitz et al., was not considered since our contours do not have as much scatter as is observed in experiments, and so a linear method is sufficient in this case. The results obtained are plotted in Fig. 3.12. It can be observed that the angle of the spray cone decreases with increasing temperatures similar to the data of Schmitz et al.[81]. It must be noted that the empirical timescale formulation used in this work was the same as that specified in the original paper by Downar-Zapolski et al.[24]. This equation was formulated to reproduce data for water and may not be accurate for other fluids. Also, in our simulations, we have observed that the exit spray cone angle is highly dependent on the internal geometry of the nozzle and so, unless the geometry used is the same, it cannot be expected that our results will match the data. However, the trend of the experimental data is satisfactorily predicted, especially the sharp decrease in the angle from 323K to 343K. Since we
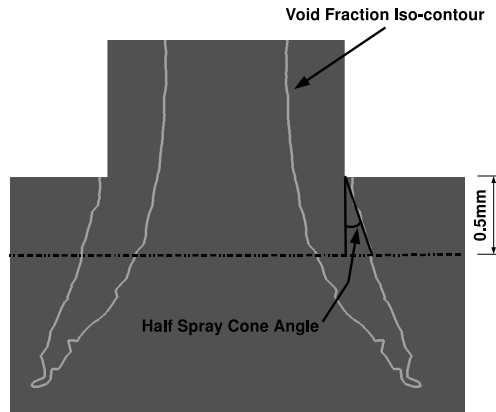
Figure 3.11. Spray cone angle measurement method for simulation of high pressure swirl injector

have not included any external spray calculations, the decrease in the spray cone angle must be caused by flash boiling in the interior of the nozzle. This is similar to the "internal flashing mode" observed by Oza [67] at injection pressures above the vapor pressure of the fuel.

The Fig. 3.13 shows the contour plots of the density, void fraction, pressure and velocity for the four cases simulated, alongside the spray images from Schmitz et al. [81]. The size of the plenum chamber used in these simulations was 4 mm from the nozzle exit. Hence, the scale provided in the paper by Schmitz et al. [81] was used to extract the corresponding part of the images. It can be noted that though the velocity contour is curving towards the center with an increase in temperature, our simulations do not predict the complete collapse of the hollow cone structure which is observed in the spray images. However, in our simulations we use a single pseudo-fluid approach which assumes that the outlet chamber is filled with a mixture of fuel liquid and vapor, unlike the experiments in which air was used in the chamber. The large difference between the fuel mixture and air densities at the downstream conditions is believed to be the main reason for the cone not collapsing completely. It is also possible that, in the experiment, the cone collapses because the atomization
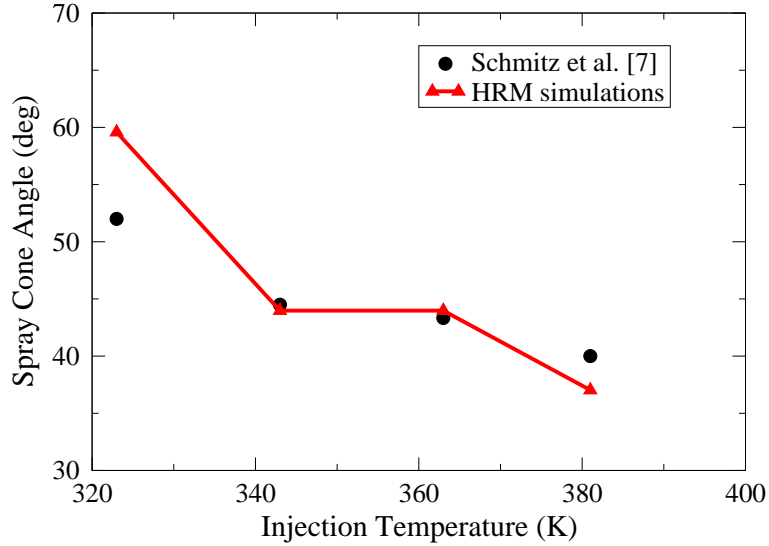
Figure 3.12. Comparison of exit spray cone angle prediction from HRMFoam with experimental data of Schmitz et al. [81]

due to flash-boiling causes smaller droplets in the spray. As these smaller droplets have lower mass, they are easily displaced by the air that is entrained from around the jet in a direction radially inwards.

Another interesting observation from the contour plots is that the region of vaporization, which usually occurs at the inlet corner of multi-hole injectors [33] has shifted to the center of the nozzle geometry because of the low pressure generated there from the swirling motion. At the center of the spray cone, the liquid-vapor mixture can be seen flowing from the plenum back into the swirl chamber through the center of the nozzle. The velocity of this flow increases with temperature because, as the temperature increases, the value of $p_{sat} - p$ increases (refer to Eqn. 2.17), thereby reducing the time scale of vaporization in Eqn. 2.12. As a result, in spite of the overall pressure gradient across the geometry remaining the same, the higher vaporization in the nozzle decreases the density of the fluid, consequently increasing its velocity. The results indicate that the code does a satisfactory job of predicting
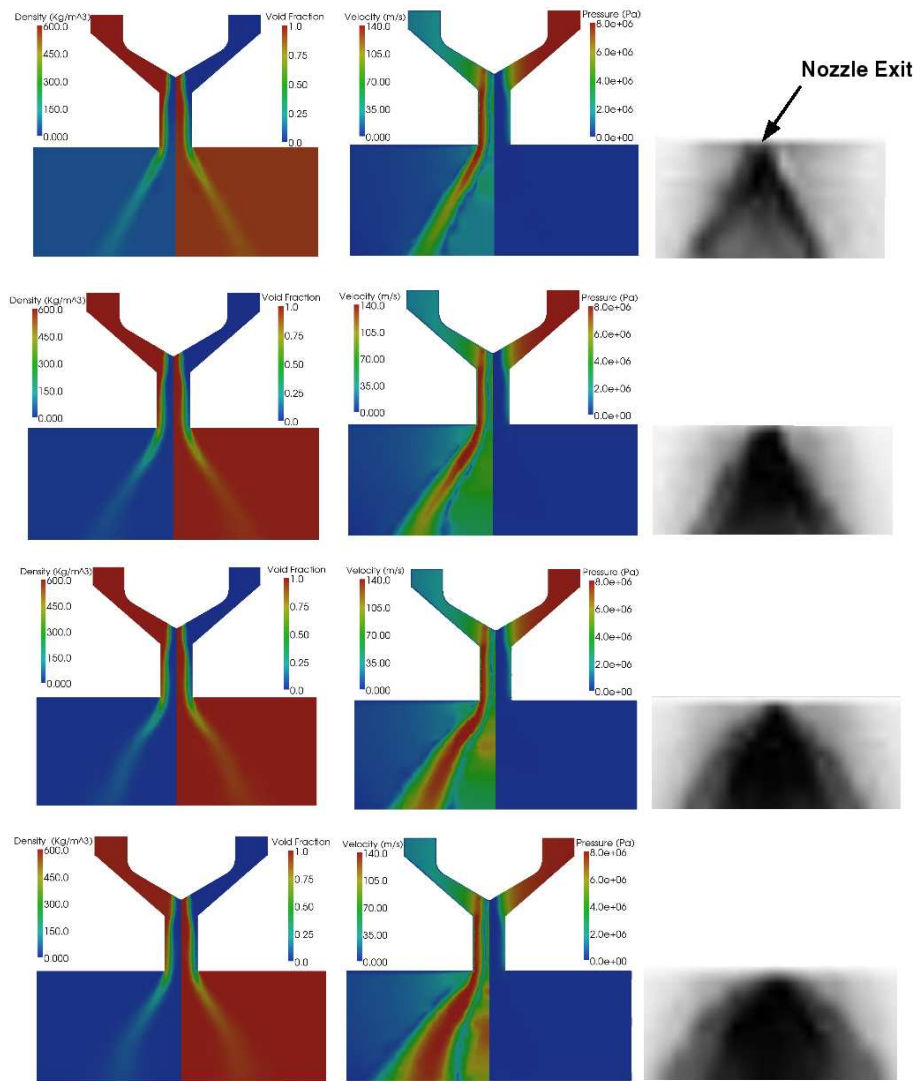
Figure 3.13. Computed contour plots of density, void fraction, velocity, and pressure from the present work, and experimental spray images from Schmitz et al. [81]. From top to bottom:323K, 343K, 363K and 381K.

the flash boiling process in the high pressure swirl injector with single component working fluids like hexane.

3.3 Simulations with Multi-Component JP8

This section presents simulations performed using the surrogate for JP8 fuel developed by Lee et al [49].

3.3.1 Geometry and Test Conditions

The matrix of test cases simulated is shown in Table 3.1 and the corresponding geometries and computational meshes are presented in the Figs. 3.14, 3.15, 3.16, and 3.17. These meshes were all 2D axisymmetric and the geometries were designed based on discussions with the United Technologies Research Center and the Energy Research Consultants (ERC). The geometries and test cases considered here correspond to planned experiments by ERC.

Inlet and outlet fillets in the nozzles were represented by conic section curves in order to avoid the generation of bad quality mesh cells. In all cases, a small rectangular section was added upstream of the nozzle geometry to prevent the boundary conditions from having a very strong effect on the flow in the nozzle. A similar section was initially added to the downstream section of these nozzles to prevent the downstream boundary conditions from being very close to the nozzle. However, it was found that the corresponding large recirculation of liquid fuel at the outlet caused the code to be unstable. Since most of the flow at the nozzle outlet is outwards and very little amount is reentering, the removal of these downstream sections improved the stability of the code. This also simplifies the process of extracting profiles of different variables like vapor void fraction, velocity etc at the nozzle outlet so as to compare these values with the experimental data.

It is to be noted that these cases were under cold conditions i.e. both inlet and outlet conditions were in the subcooled region for JP8. The downstream pressure was chosen to be high enough so that there would be no cavitation. This is done by calculating the cavitation parameter K which is given as

$$K = \frac{P_{up} - P_{vapor}}{P_{up} - P_{dn}} \tag{3.1}$$

where, P stands for the pressure, and the subscripts *up* and *dn* correspond to the conditions upstream and downstream of the nozzle respectively. The subscript *vapor* corresponds to the vapor pressure of the fuel. Nurick [65] developed a simple 1D analysis to evaluate the coefficient of discharge (C_D) of cavitating nozzles and found that C_D increased with $\sqrt{K}$ upto a certain point and then remained constant. The point at which the value of C_D becomes constant was found to be at a K value of less than 2 and is the critical point after which the nozzle no longer cavitates. Schmidt [79] plotted the experimental data of many different authors and found that most of the data agreed with the 1D analysis of Nurick. Hence, in the current simulations, the conditions were adjusted to keep the value of K as close to 2 as possible in order to avoid cavitation. The inlet pressure and temperature for these cases were 1.97MPa and 305K respectively, and the downstream pressure was 0.79MPa. These cases are run under conditions with no phase change even though HRMFoam is a flash boiling code in order to give an insight about the flow behavior in these nozzles. These results will assist experimentalists in building the test rig required to conduct flash boiling experiments. Finally, the data obtained will be used to better validate the HRMFoam code for multicomponent fluids and to adjust the empirical constants in the time scale formulation.

Different mesh resolutions were considered for the Case-1 and it was found that coarser resolutions at the inlet corner of the nozzle led to the formation of vapor which would be unexpected due to the adjustment of the K parameter. Hence, it was

Table 3.1. Test cases simulated for JP8

Case No.	Case Name	L/D ratio	Inlet Shape
1	Sudden Contraction	3.33	Corner radius=0.05mm
2	Rounded Inlet	3.33	Corner radius=0.25mm
3	Internal Perturbation-1	3.33	Cylindrical perturbation
4	Internal Perturbation-2	3.33	Frustum shaped perturbation

concluded that the mesh resolution needed to be fine enough to capture the small scale structures existing at the inlet corner of the nozzle. The mesh resolution was considered fine enough when the void fraction of vapor was found to be negligible. This condition was obtained when the distance of the first point from the wall was around 1 μm. The meshes for the remaining cases were constructed by generating a boundary layer mesh at the nozzle wall with the first point at 1 μm and a growth rate of 1.1 from the wall. A Cartesian mesh was then constructed for the remaining domain from this boundary layer mesh.

In all cases, the flow is initialized to a uniform pressure of 1.97MPa and then, a pressure ramp is set up to reduce the outlet pressure from this value to 0.79 MPa over a time of 0.01 milliseconds. A Neumann boundary condition of zero gradient is used at the inlet and outlet for the velocity and the walls are no-slip walls with zero velocity.

3.3.2   Results and Discussion

The contour plots presented here are snapshots of the cases and do not accurately represent the unsteady nature of these cases. The unsteadiness in Case-1 can be seen from the outlet mass flow rates shown in Fig. 3.18. The contour plots for pressure and velocity for Case-1 are shown in the Fig. 3.19. Due to the very small curvature of 0.05mm at the inlet corner, the flow separates and forms a vena contracta. This is accompanied by the formation and shedding of vortices as seen from the streamlines
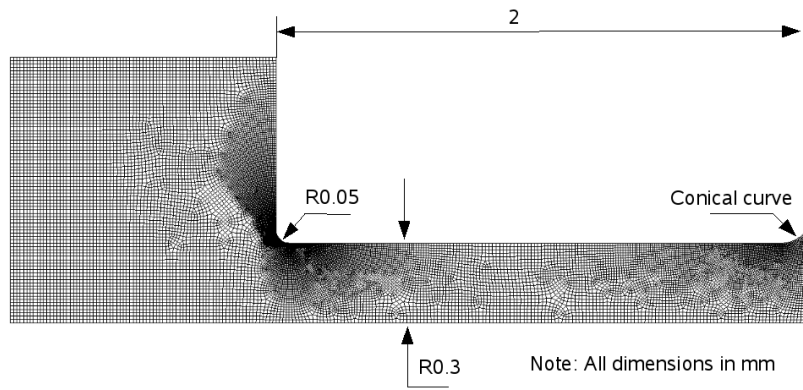
Figure 3.14. Geometry and mesh for the Case-1
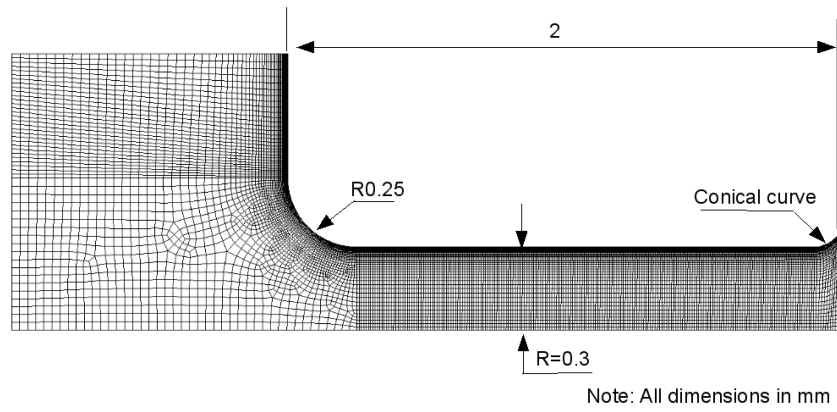
Figure 3.15. Geometry and mesh for the Case-2
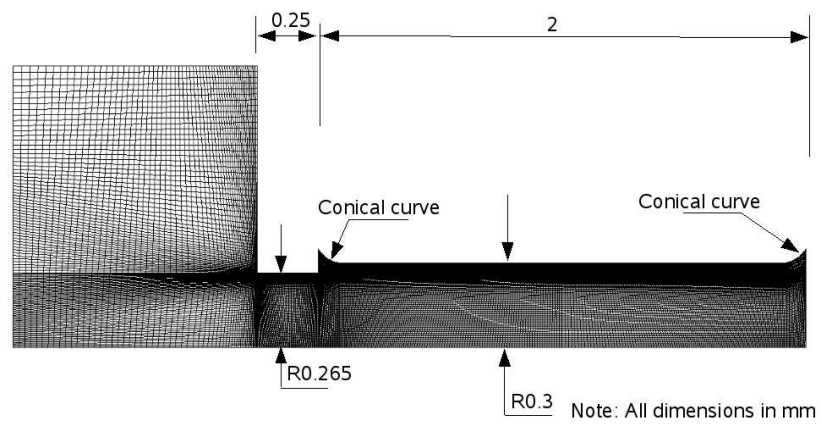
Figure 3.16. Geometry and mesh for the Case-3
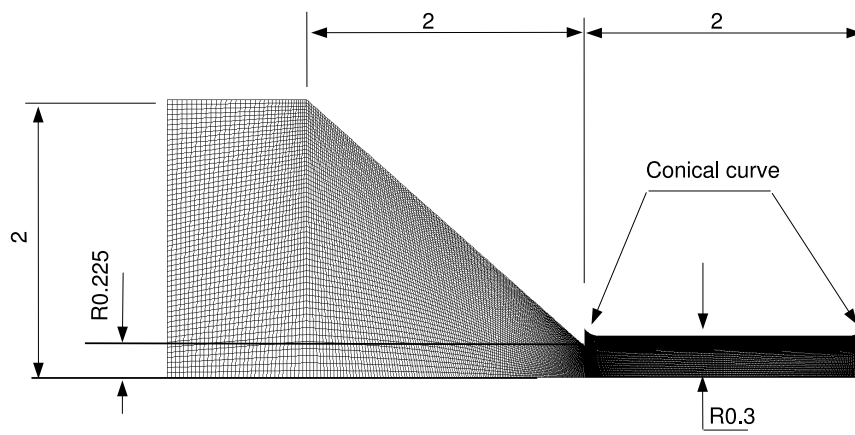
Figure 3.17. Geometry and mesh for the Case-4

70
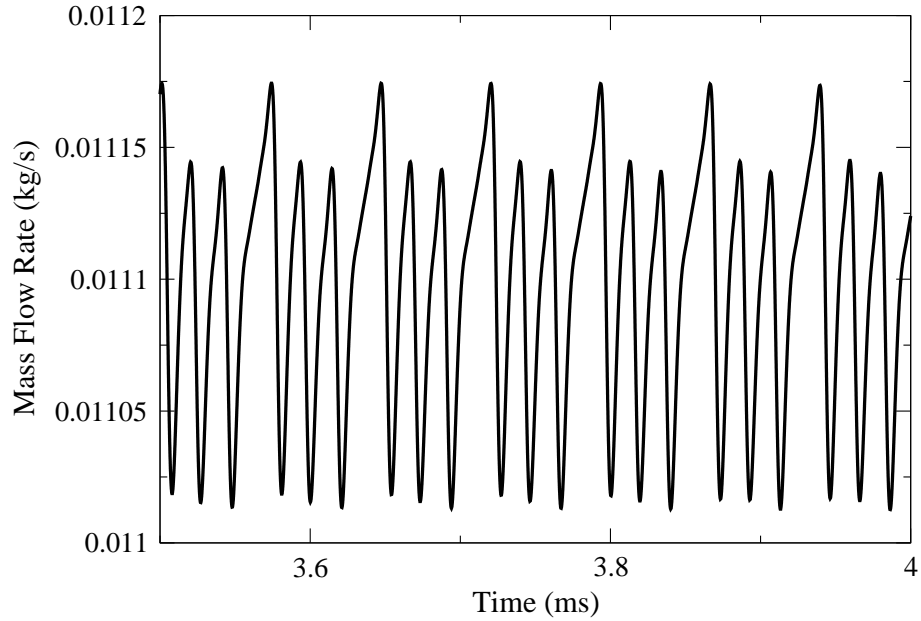
Figure 3.18. Outlet mass flow rates for Case-1

shown in Fig. 3.20. The flow behavior observed here is similar to that in the work of Canino and Heister [15]. A discrete Fourier transform was conducted on the outlet mass flow rates to determine the frequency of oscillations. Fig. 3.21 shows the magnitude of oscillations with respect to the frequency. Harmonics of 14kHz exist in the solution and the harmonic at 56kHz is most dominant. Canino and Heister found that at the beginning of every period of oscillation, several small recirculation regions are seen near the inlet corner. As time progresses, vortices pinch off from the recirculation region and are convected downstream. The streamline plot Fig. 3.20 shows this behavior. At the instant of this snapshot a vortex can be seen pinching off from the inlet corner and, further downstream, a couple of vortices can be seen being convected downstream. The colors of the streamline plot show that the pressure drop associated with the separation at the inlet corner does not lead to any cavitation.

The second case has a much larger curvature at the inlet corner. As seen from the contour plots in Fig. 3.22 and the streamline plot Fig. 3.23, the curvature is gradual
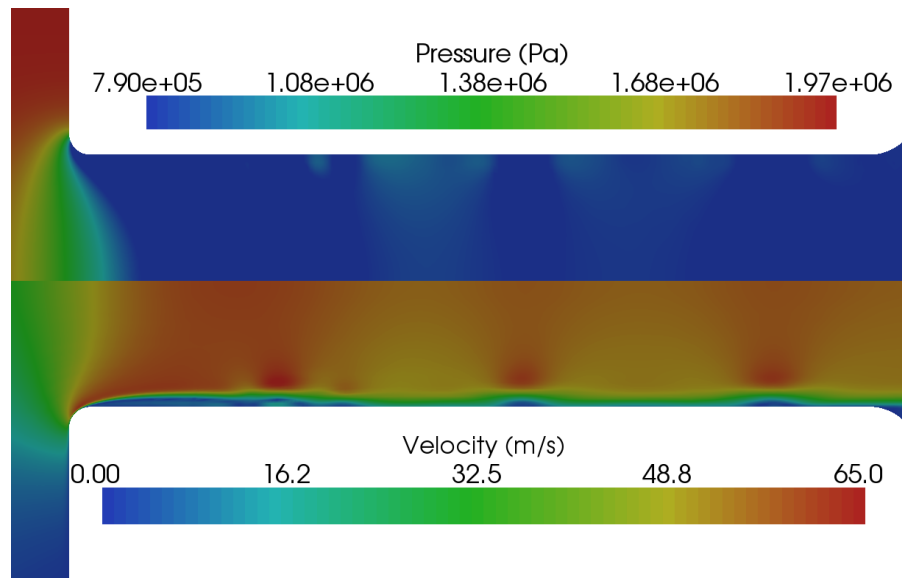
Figure 3.19. Pressure and velocity contour for Case-1
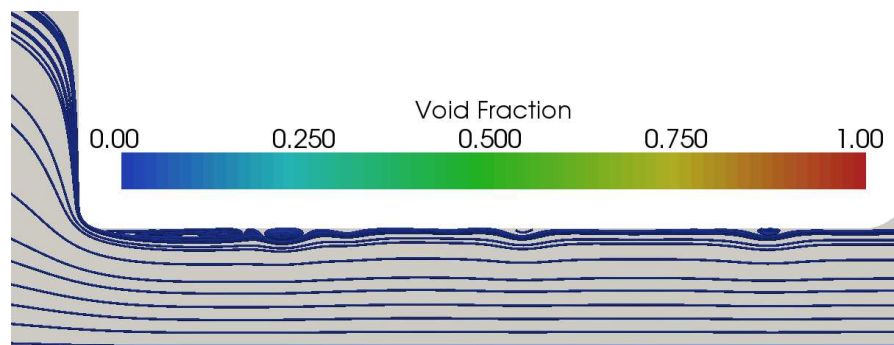
Figure 3.20. Velocity streamlines for Case-1 colored by void fraction of vapor

Figure 3.21. Discrete Fourier transform of outlet mass flow rates from Case-1

enough so that the flow does not separate at the inlet corner and no vena contracta is formed. These observations are consistent with the work of Canino and Heister [15] who found that the pulsations in the flow reduced with the increase in rounding of the inlet corner due to lack of flow separation. The colors of the streamline plot also show that there is no vapor generated in the domain. The curvature at the inlet corner prevents a steep pressure drop which is usually the main cause for vapor generation in nozzles with sharp inlet corners.

The final two cases are similar since they introduce some perturbations in the flow before it enters the nozzle. Fig. 3.24 shows the pressure and velocity contours for the Case-3. In this case, the flow encounters two sharp corners before entering the nozzle. This leads to two large recirculation regions and extremely unsteady flow with lots of oscillations as seen from the mass flow rate plot Fig. 3.25. The discrete Fourier transform of the mass flow rates, Fig. 3.26 shows that a number of frequencies dominate the unsteadiness. The streamline plot (Fig. 3.27) shows the

73
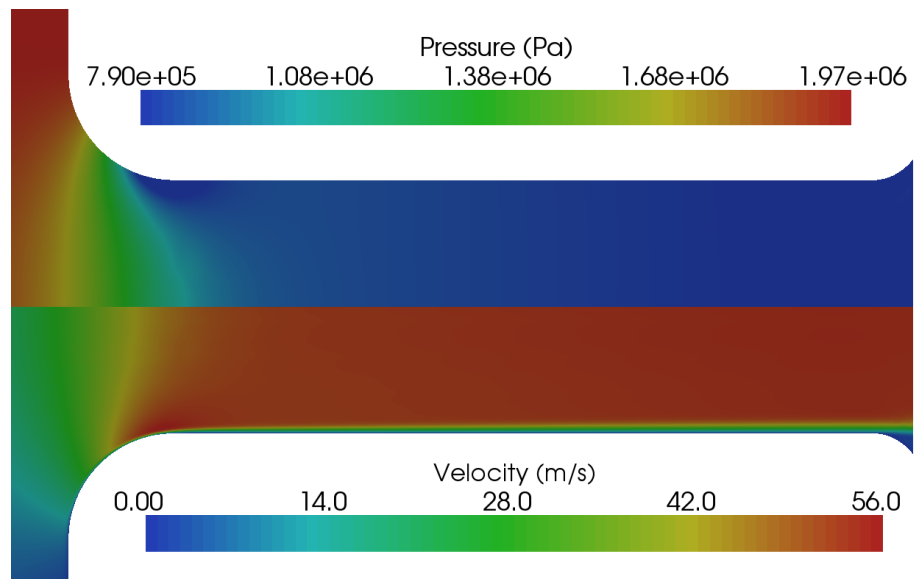
Figure 3.22. Pressure and velocity contour for Case-2
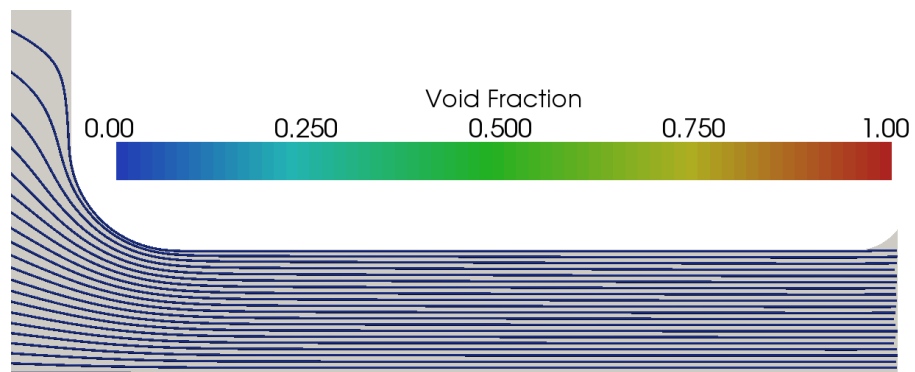
Figure 3.23. Velocity streamlines for Case-2 colored by void fraction of vapor
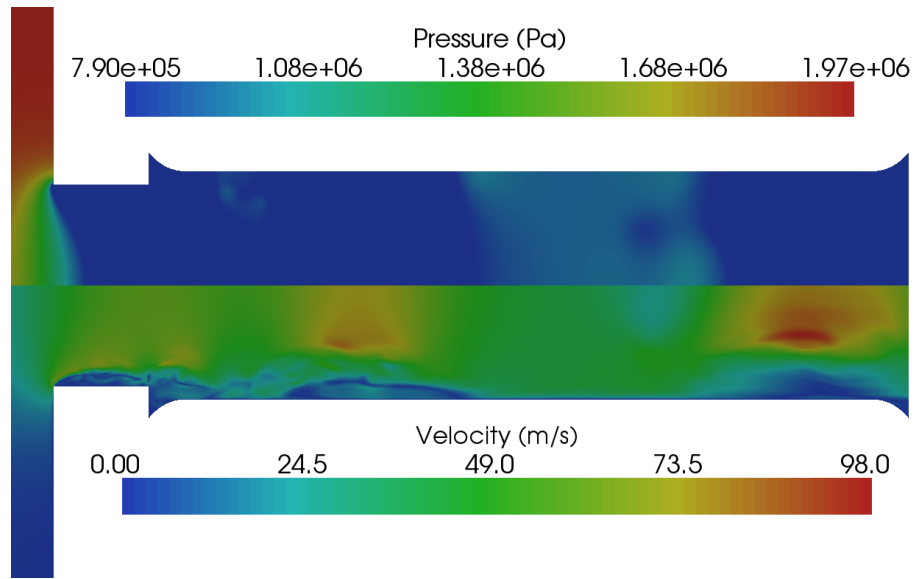
Figure 3.24. Pressure and velocity contour for Case-3

origin of vortical structures near the inlet corner and the subsequent shedding of these structures downstream. The void fraction contour indicates that the pressure drop at the inlet corner leads to the formation of significant amounts of vapor. In addition, a very low pressure exists at the center of the vortices leading to the formation of more vapor. As the liquid flows around the vortices, its velocity increases due to local contraction leading to periodical acceleration regions in the nozzle.

Finally, Fig. 3.28 and 3.29 are the results for Case-4. In this case, a large recirculation zone is formed at the inlet corner as a result of the angle of the incoming flow. The streamline plot shows the formation and shedding of vortical structures and the outflow mass flow rate plot, Fig. 3.30, shows the unsteadiness in this flow. Similar to the previous case, the discrete Fourier transform, Fig. 3.31 shows a number of dominant frequencies. The void fraction plot shows the formation of vapor at the inlet corner and at the center of the vortices.

An interesting phenomenon which can be observed from the void fraction plots 3.27 and 3.29, is that as the vapor bubble moves downstream, the color of the contour
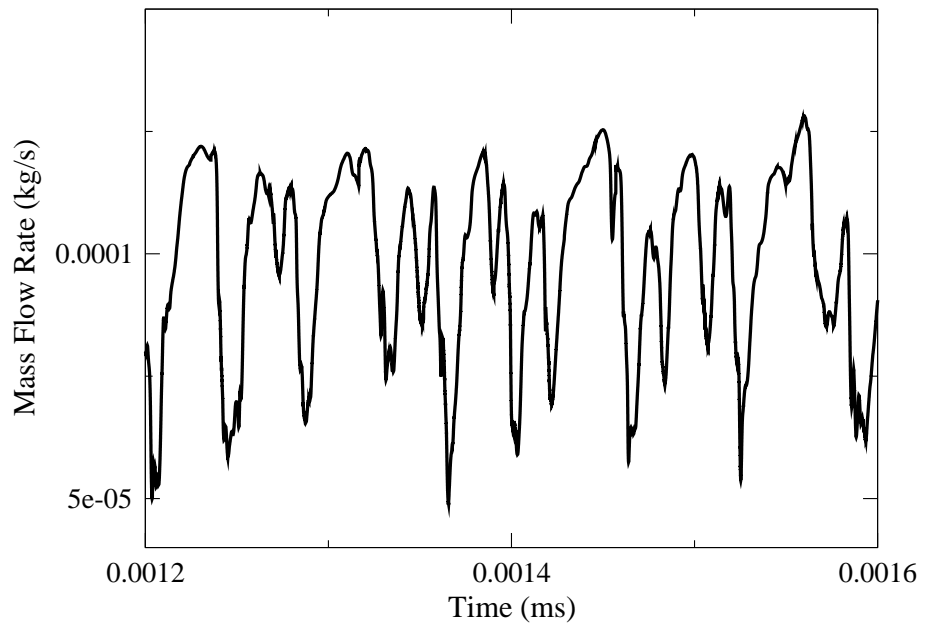
Figure 3.25. Outlet mass flow rates for Case-3
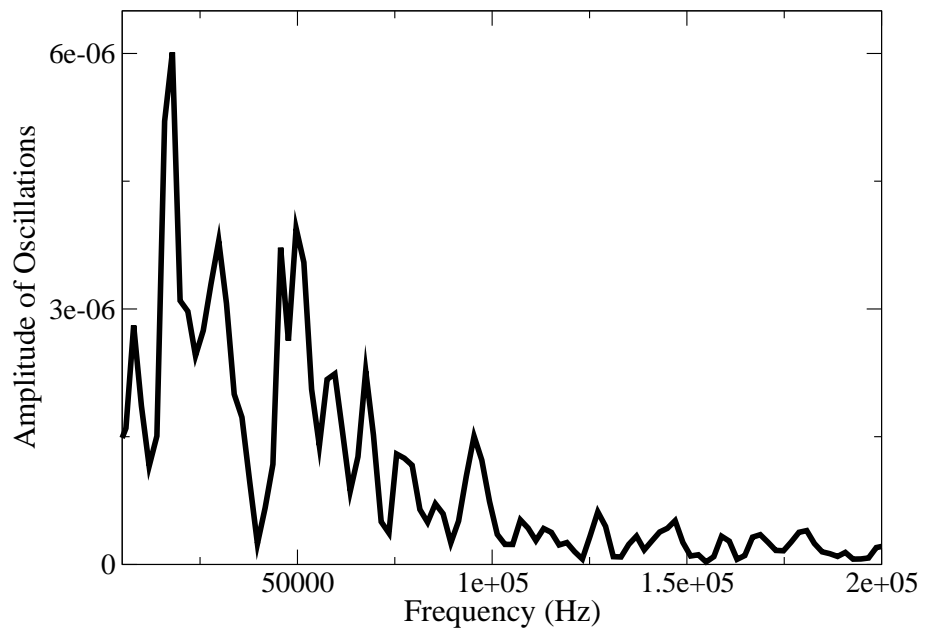
Figure 3.26. Discrete Fourier transform of outlet mass flow rates from Case-3
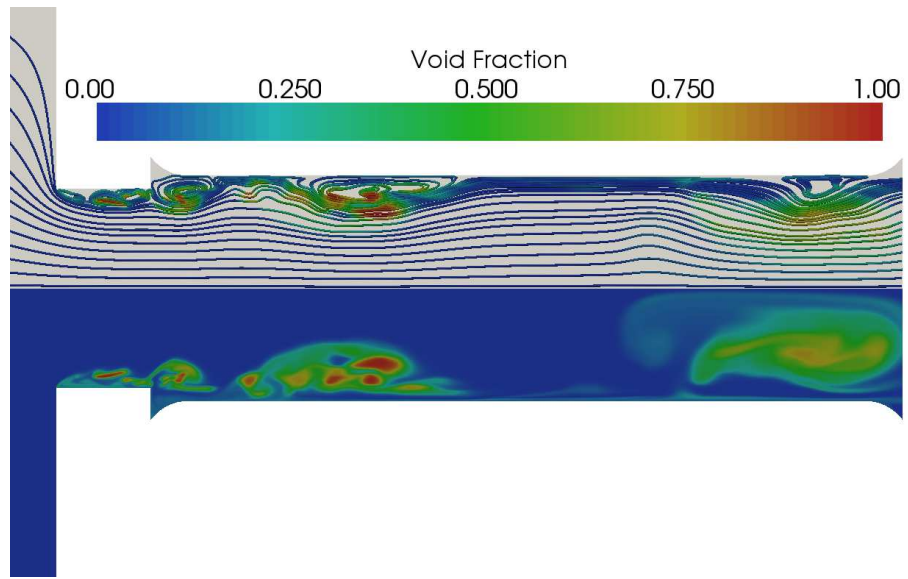
Figure 3.27. Velocity streamlines colored by void fraction of vapor and the void fraction contour for Case-3
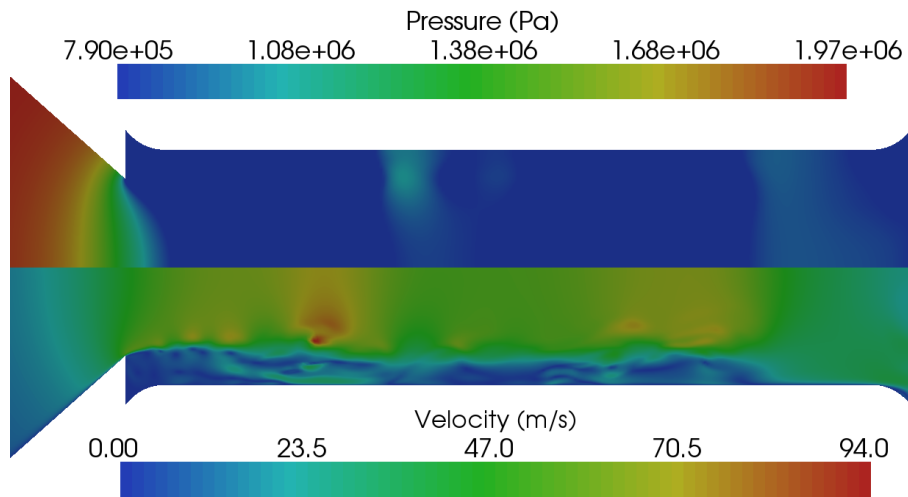
Figure 3.28. Pressure and velocity contour for Case-4
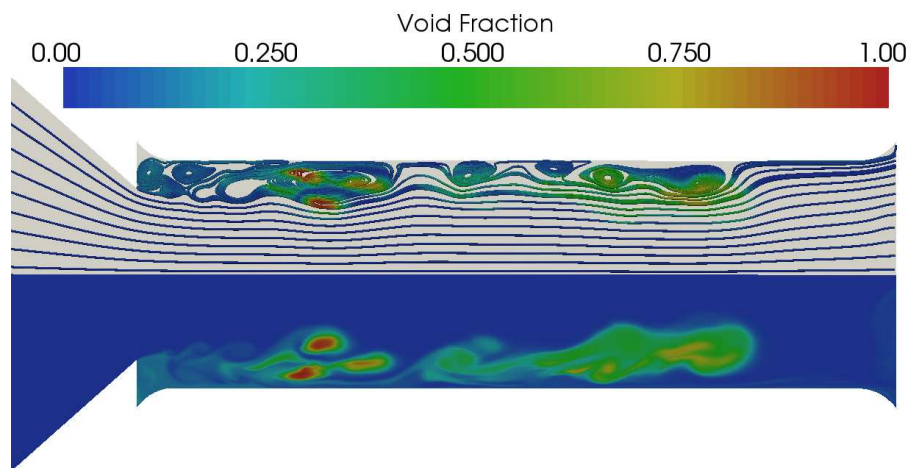
Figure 3.29. Velocity streamlines colored by void fraction of vapor and the void fraction contour for Case-4
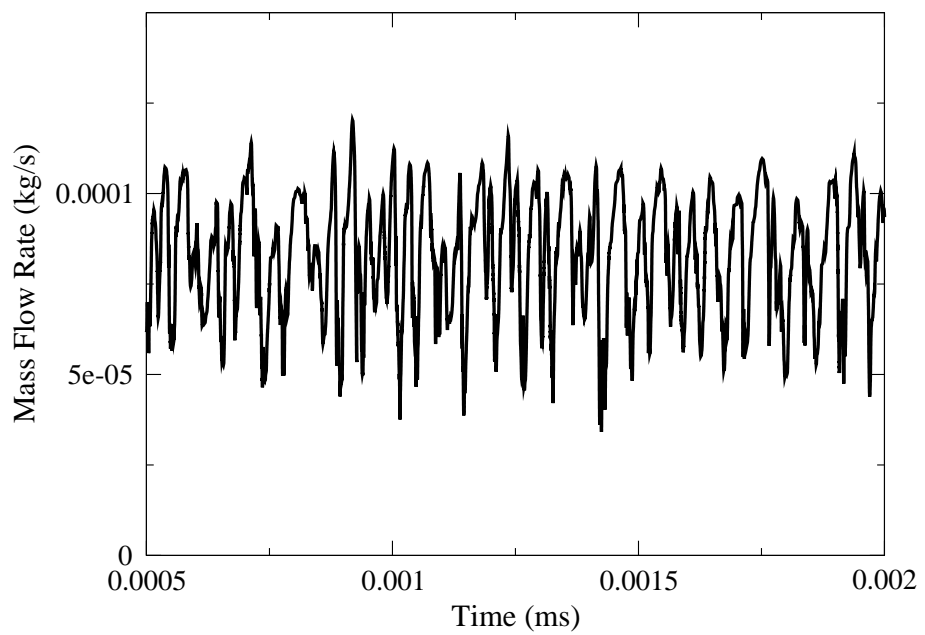
Figure 3.30. Outlet mass flow rates for Case-4

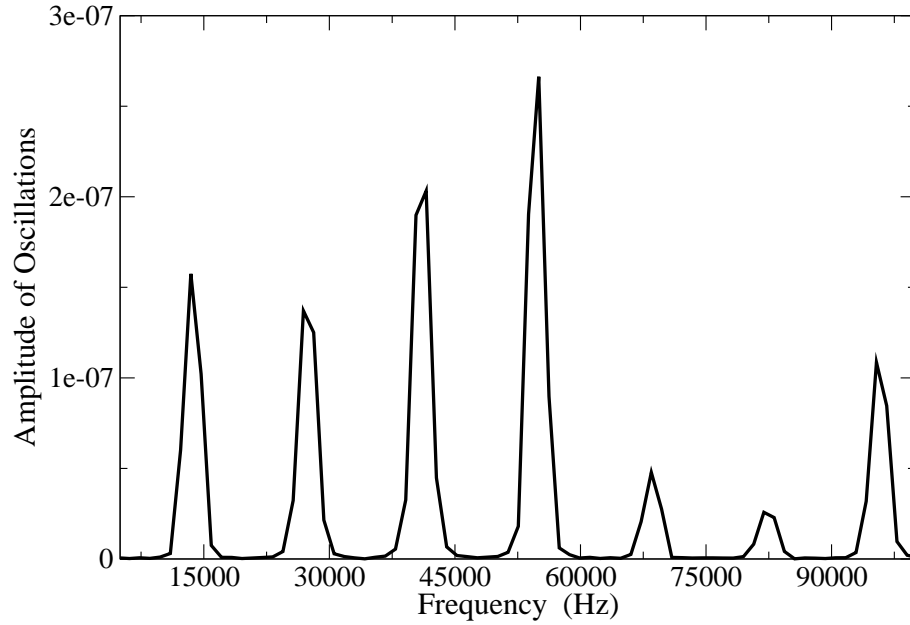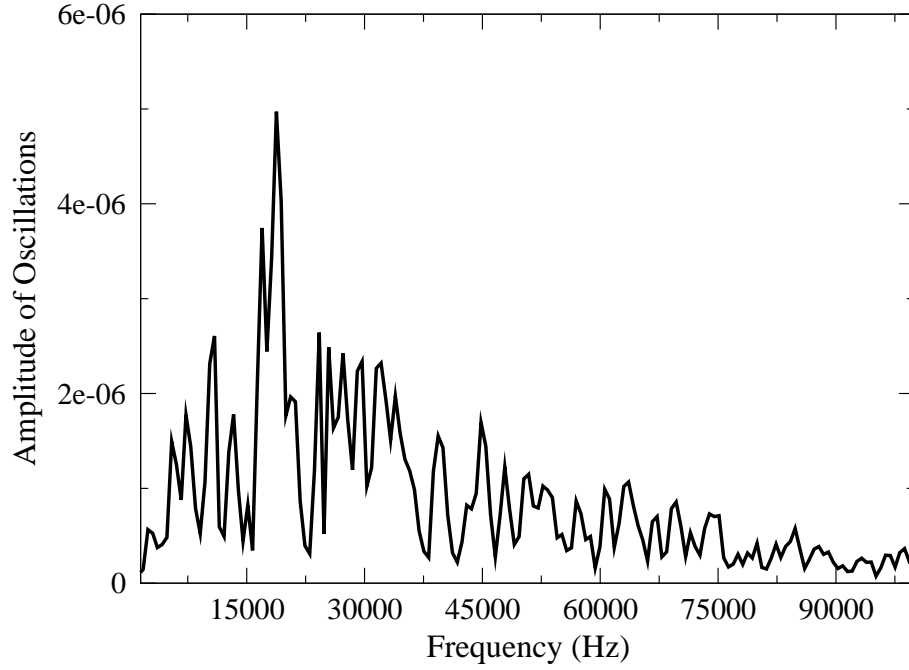**Figure 3.31.** Discrete Fourier transform of outlet mass flow rates from Case-4

at the center of the vortex becomes yellow. This means that the vapor formed at the inlet corner either mixes or condenses as it moves downstream since the conditions of the flow downstream are in the subcooled region for JP8. It is to be noted that in all contour plots, the pressure has been scaled according to the inlet and outlet pressures and not by the minimum and maximum pressure in the domain. The uniform scaling helps to directly compare the different contour plots. Finally, it is important to note that these calculations are all two-dimensional axisymmetric and thus any potential for variation in the third dimension is suppressed. It is quite possible that in real nozzles, the transient structures have significant three-dimensional features that cannot be represented in the current calculations. These three-dimensional aspects would significantly impact the energy spectrum of vortex shedding in the nozzles causing the actual frequencies to differ from those reported in the present work. Also, in the present work, a Newton's iteration is used to solve the pressure equation as explained in section 2.1.3. Since this is an iterative procedure, it is very possible that there

79
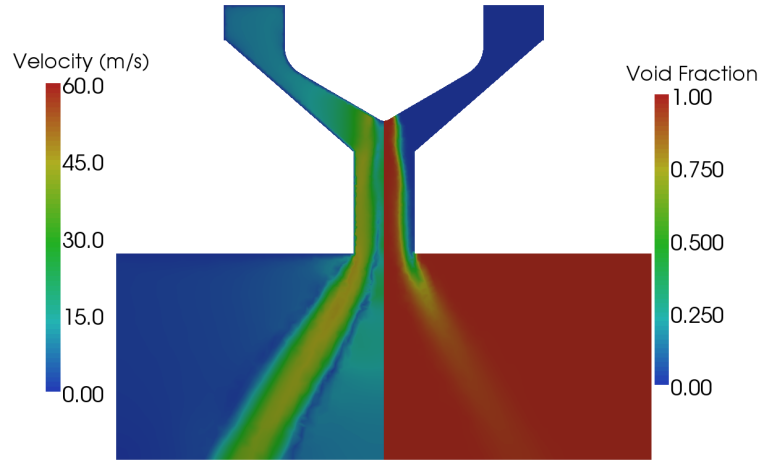
Figure 3.32. Velocity and void fraction contours for the high pressure swirl injector with E85 as fluid. Injection conditions were 1MPA and 345K, and downstream pressure was 0.05MPa

may be overshoots and undershoots in the pressure solution of these highly transient cases. This will further modify the nature of oscillations in the mass flow rates.

3.4   Simulations with Gasoline-Ethanol Blends

The high pressure swirl injector used in section 3.2 was used to simulate two cases with E85. Both the considered cases had the same injection conditions of 1MPa and 345K. However, the first case had a downstream (chamber) pressure of 0.05MPa whereas the second case had a very low pressure of 0.015MPa. The Figs. 3.32 and 3.33 show the consecutive velocity and void fraction contours. It can be seen from the velocity contours that the case with the lower downstream pressure no longer shows the hollow cone structure that is visible in Fig. 3.32 and in the results with n-hexane presented in section 3.2. It was noted in section 3.2 that for the cases of Schmitz et al. [81], HRMFoam did not show a complete cone collapse for the higher temperature cases. From Fig. 3.33, it can be observed that even though the atomization of the jet is not considered and the plenum is filled with fuel vapor instead of air, the cone collapse can be observed by drastically increasing the amount of vapor formed inside
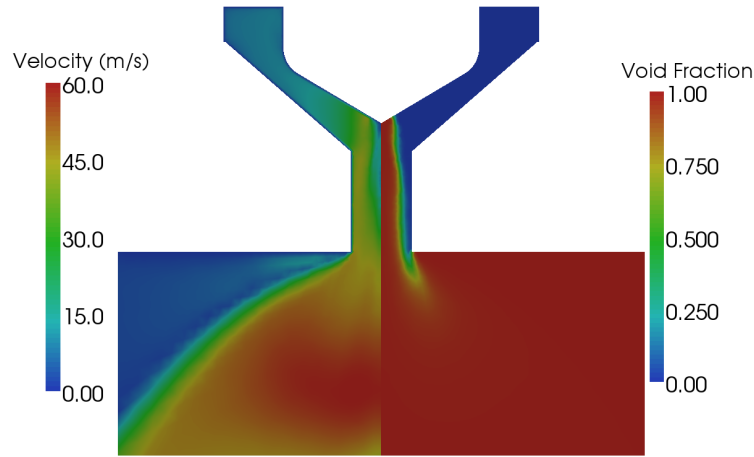
Figure 3.33. Velocity and void fraction contours for the high pressure swirl injector with E85 as fluid. Injection conditions were 1MPA and 345K, and downstream pressure was 0.015MPa

the nozzle. As the amount of vaporization increases, the cone collapses because the exiting jet no longer has the momentum to expand against the surrounding fuel vapor in the plenum. However, as the amount of vapor formed increases further, the jet is highly under expanded and so the exit cone angle starts increasing again. This can be noticed in velocity contour in Fig. 3.33, which shows a much higher spray cone angle as compared to that in Fig. 3.32. Additionally, the void fraction contours show that the low downstream pressure case has much less liquid penetration inside the plenum, which is expected due to the higher vaporization.

In order to compare between two gasoline-ethanol blends, simulations were performed on a multi-hole injector geometry. It has been found that the spray cone structure of the swirl injectors is highly dependent on the pressure in the chamber and complete collapse of the cone can occur in the stratified operation mode [53]. Comparatively, multi-hole injectors are found to produce sprays in which the spray cone angle is only marginally affected by injection and chamber pressures. However, flash boiling has been found to drastically affect the structure of these sprays as well [69]. The multi-hole injector used in this case was based on the design obtained from

81
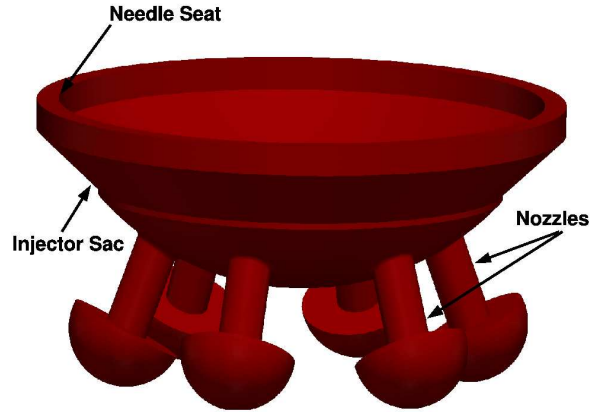
Figure 3.34. Geometry of six hole injector

Bosch GmbH. The complete design of this injector was presented in [33] and for the purpose of the current study, the geometry was modified to simulate a 6-hole injector. The modified geometry and mesh used are presented in Figs. 3.34 and 3.35 respectively. It can be seen that only a $1/6^{th}$ section of the actual injector is simulated with periodic boundaries on the cut planes. Also, a semi-spherical plenum is added to the downstream of the nozzle to avoid the strong influence of boundary conditions on the vaporization characteristics. Two gasoline-ethanol fuel blends were used as working fluids: E60 and E85. In both cases, the injection pressure and temperature were 0.2MPa and 345K respectively, and the chamber pressure was 50kPa. The Figs. 3.36, 3.37, 3.38, and 3.39 show the velocity and void fraction contours for the two cases respectively. E60 has a higher vapor pressure than E85 as seen from Fig. 3.1 and hence it undergoes more vaporization. This can be observed by comparing Fig. 3.37 and Fig. 3.39. The penetration of the liquid into the outlet plenum is much less in the case of E60 as compared to E85. Additionally, the velocity contours show a much wider spray cone angle for E60 due to the presence of more vapor inside the nozzle.

Figure 3.35. Computational mesh of six hole injector

Velocity (m/s)

| 0.00 | 4.50 | 9.00 | 13.5 | 18.0 |
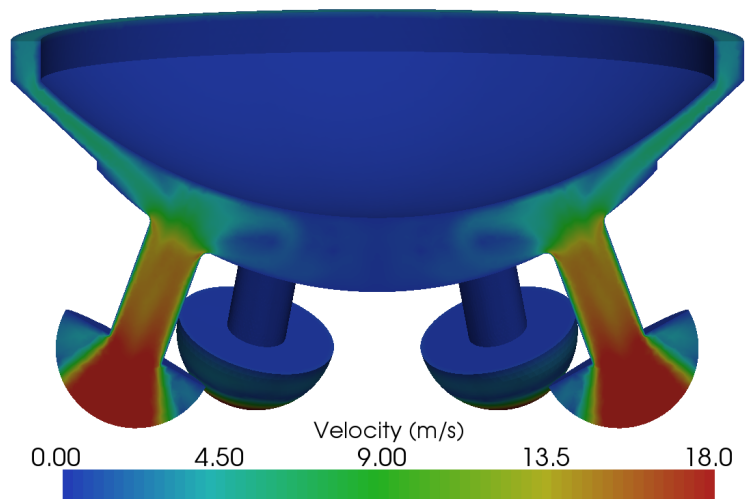
Figure 3.36. Velocity contour for 6-hole injector with E60 as fluid. Injection conditions were 0.2MPa and 345K respectively, and the chamber pressure was 50kPa
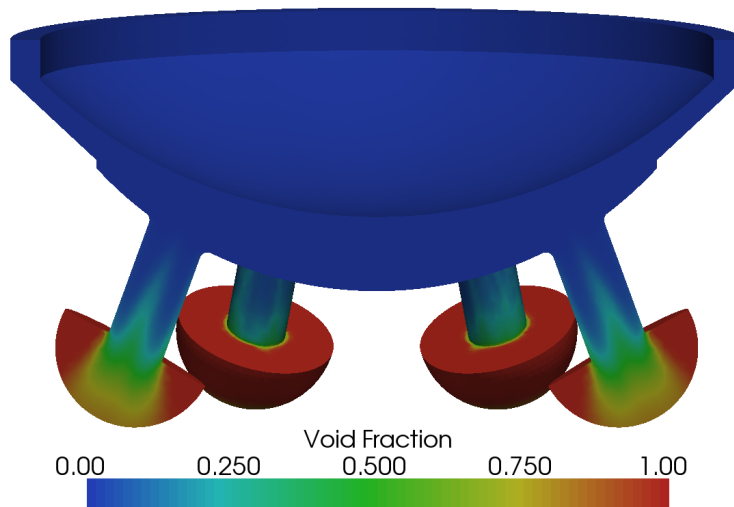
Figure 3.37. Void fraction contour for 6-hole injector with E60 as fluid. Injection conditions were 0.2MPa and 345K respectively, and the chamber pressure was 50kPa
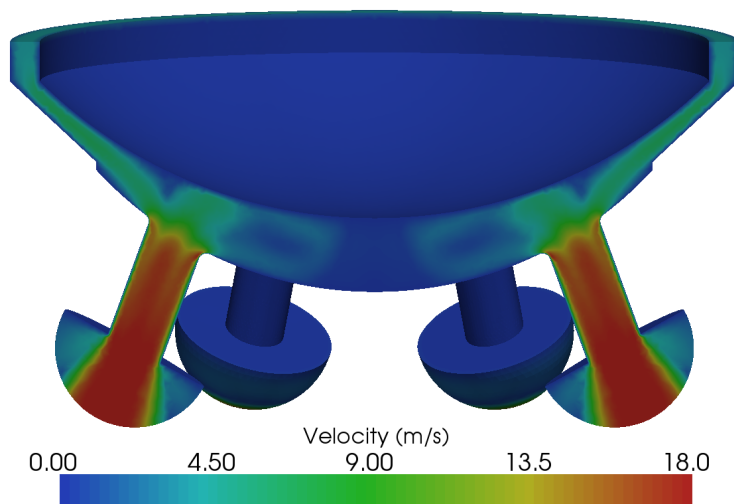
Figure 3.38. Velocity contour for 6-hole injector with E85 as fluid. Injection conditions were 0.2MPa and 345K respectively, and the chamber pressure was 50kPa
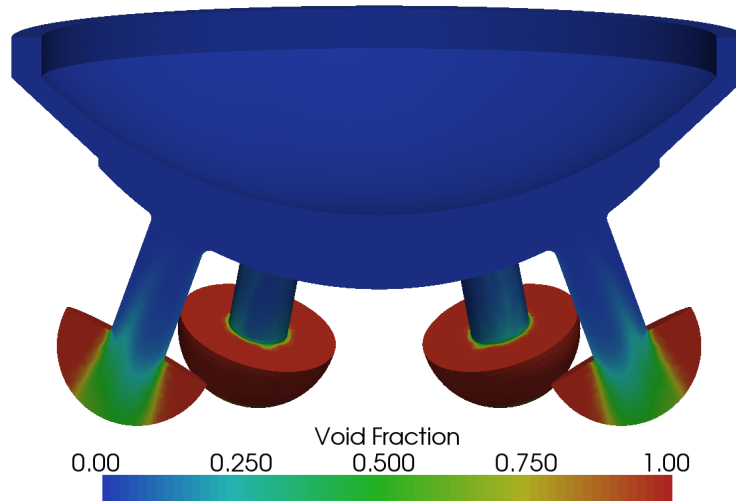
Figure 3.39. Void fraction for 6-hole injector with E85 as fluid. Injection conditions were 0.2MPa and 345K respectively, and the chamber pressure was 50kPa

An interesting phenomenon is observed from the void fraction contours Figs. 3.37 and 3.39. It can be seen that high vapor formation occurs around the center of the nozzle, close to the exit. In order to further investigate this phenomenon, Fig. 3.40, shows the streamlines inside the nozzle, colored by the velocity, for the simulation with E60. It is seen that a vortical structure exists at the center of the nozzle. The main cause of this vorticity is the large rotation that the high momentum flow has to go through, before it flows into the nozzle. As the fluid flows into the nozzle, its velocity increases due to the lower cross sectional area, thereby increasing its vorticity. Consequently, the pressure at the core of the vortex decreases leading to vapor formation at the center of the vortices. The evolution of pressure, presented in Fig. 3.41, shows this gradual decrease in pressure at the center of the vortex, starting from the needle tip.

In addition to the central vortex, two additional vortical structures can be observed in Fig. 3.40 originating from the central vortices and moving towards the periodic boundaries. These vortices appear to be similar to the bridging vortices observed in Reid et al. [72] for counter-rotating vortices, and in Chang et al. [17] for two
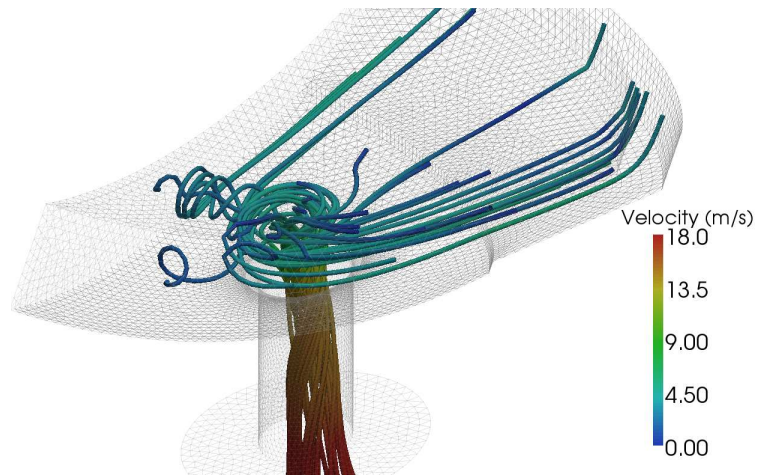
Figure 3.40. Streamlines colored by velocity showing central vortex and bridging vortices in 6-hole injector with E60. Injection conditions were 0.2MPa and 345K respectively, and the chamber pressure was 50kPa
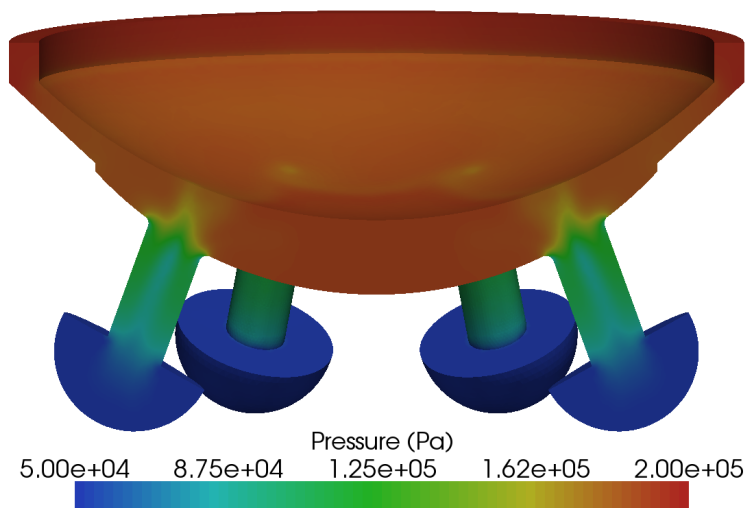
Figure 3.41. Pressure for 6-hole injector with E60 as fluid. Injection conditions were 0.2MPa and 345K respectively, and the chamber pressure was 50kPa

co-rotating vortices while studying cavitating flows. These bridging vortices originate due to the interaction between the outermost flow of the central vortices with the bulk flow, and link adjacent holes [72]. Similar vortical structures and subsequent vapor formation due to cavitation have been observed in fuel injectors for diesel engines [72, 6]. This mode of cavitation is known as vortex or string cavitation, and the current work is the first time that this mode is observed in flash boiling flows. However, the complete analysis of this "string flash boiling" is out of the scope of this work and is left for future work.

It should be noted that since GEFlash requires the pure component vapor pressures of ethanol and gasoline at the injection temperature (see Eqn. 2.25), and the pure gasoline vapor pressure at 345K was not found in literature, the vapor pressure of pure indolene was used from the Aspen Plus model developed in section 2.2.6. Also, the viscosity of the gasoline-ethanol blends was assumed to be a constant and its value was taken to be equal to the viscosity of octane at 273K. This assumption is not very significant because most of the injector flows considered here are very high Reynolds number flows and the viscosity is not expected to have much effect.

The results in this section qualitatively show the differences in the vaporization characteristics in two different injectors: the high pressure swirl injector and the 6-hole injector. Additionally, the differences in the flow with two different gasoline-ethanol blends is also presented. Though the results obtained follow the expected trends, in the absence of experimental validations, it is difficult to predict whether the results are quantitatively accurate.

3.5 Parametric Study

A parametric study was conducted in order to understand the finite rate mechanism that governs flash boiling. For the parametric study, a 2D axisymmetric nozzle with a diameter of 0.34mm, and length to diameter (L/D) ratio of 4 was used. Five

Table 3.2. Test cases for parametric study using water as working fluid

Case Name	P_{inj} (MPa)	P_{chm} (MPa)	T_{inj} (K)	no. cases
W-1	1	0.015	332-452	13
W-2	0.7	0.101	392-439	6
W-3	1	0.101	380-450	10
W-4	5	0.101	380-457	8
W-5	0.7	0.015	332-438	10

Table 3.3. Test cases for parametric study using n-hexane as working fluid

Case Name	P_{inj} (MPa)	P_{chm} (MPa)	T_{inj} (K)	no. cases
H-1	1	0.015	294-345	7
H-2	0.35	0.07	338-373	8
H-3	0.5	0.03	312-373	8

different fluids were considered: water, n-hexane, n-octane, E60, and E85. The properties of the single component fluids were provided by the REFPROP database and code library [50]. REFPROP uses the Span and Wagner equation of state [86] for n-hexane and n-octane, and the Wagner and Pruss equation of state [92] for water. The properties of the ethanol fuels were obtained from the GEFlash model. For different injection and chamber pressures, the injection temperature was varied from low to high. All cases were assumed to be under adiabatic conditions, and hence an increase in injection temperature implies an increase in the downstream degree of superheat. The Tables 3.2 - 3.6 show the different cases that were simulated. The variables P_{inj}, P_{chm}, and T_{inj} represent the injection pressure, downstream chamber pressure, and the injection temperature respectively.

In order to analyze the output obtained from these test cases, a variable is defined which indicates the amount of deviation from equilibrium. This variable is called ΔEq and is given as follows

$$\Delta Eq = Avg(x/\overline{x}) \tag{3.2}$$

Table 3.4. Test cases for parametric study using octane as working fluid

Case Name	P_{inj} (MPa)	P_{chm} (MPa)	T_{inj} (K)	no. cases
O-1	1	0.015	345-450	8
O-2	0.06	0.015	345-379	9

Table 3.5. Test cases for parametric study using E60 as working fluid

Case Name	P_{inj} (MPa)	P_{chm} (MPa)	T_{inj} (K)	no. cases
E60-1	15	0.05	318-348	4
E60-2	0.2	0.05	318-348	8

where Avg represents an average over the outlet of the nozzle. The second variable represents the maximum energy available for vaporization at the downstream condition, and is represented by the degree of superheat downstream of the nozzle. This variable is calculated as

$$\Delta T = T_{inj} - T_{sat}(P_{chm}) \tag{3.3}$$

where $T_{sat}(P_{chm})$ is the saturation temperature obtained at the downstream pressure. It is to be noted here that since a 2D axisymmetric case is used to perform this analysis, any variation in the 3rd dimension is suppressed. The Fig. 3.42 shows the plot of the ΔEq versus $\Delta T/T_{inj}$ for all the cases presented in Tables 3.2 -3.6.

Three distinct sections can be observed in each curve as shown in Fig. 3.43. Each of these sections will be explained below

Table 3.6. Test cases for parametric study using E85 as working fluid

Case Name	P_{inj} (MPa)	P_{chm} (MPa)	T_{inj} (K)	no. cases
E85-1	15	0.05	328-348	3
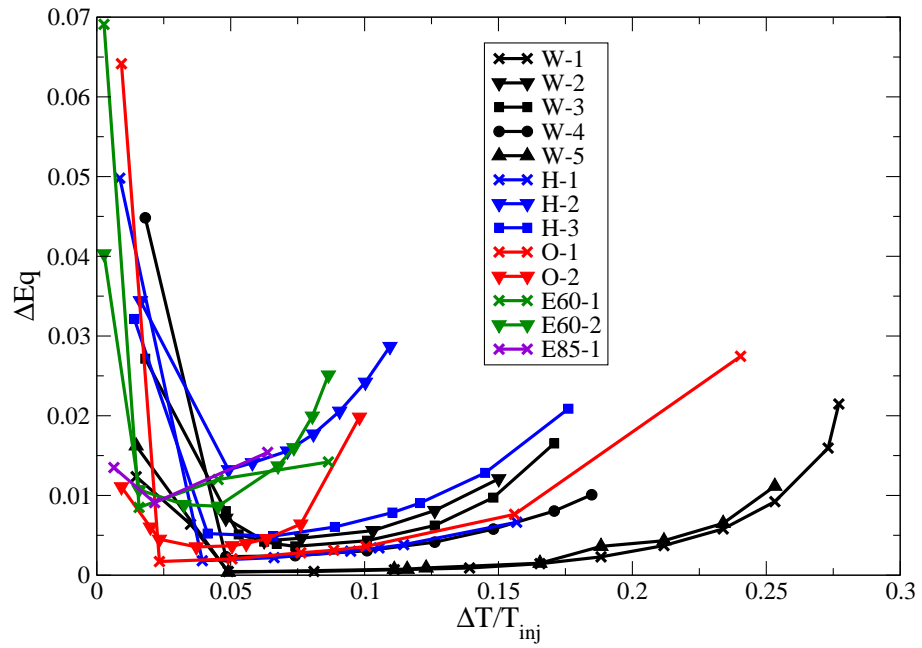
Figure 3.42. Plot of ΔEq versus $\frac{\Delta T}{T_{inj}}$.
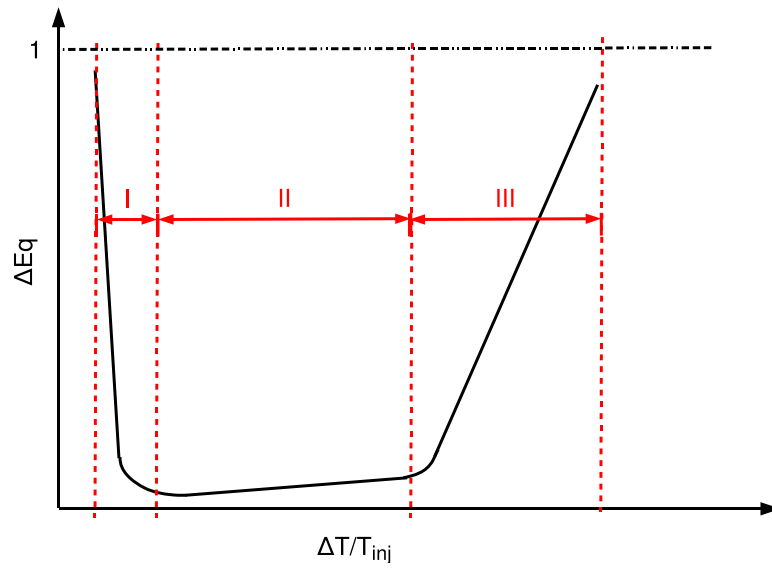
Figure 3.43. Conceptual plot representing ΔEq versus $\frac{\Delta T}{T_{inj}}$.

90

3.5.1 Section I:

As the degree of superheat increases above zero (implying that the downstream condition becomes superheated), the value of ΔEq decreases quickly with respect to the degree of superheat. To further explain this section, refer to Fig. 3.44 which shows a plot of mass fraction along the nozzle exit for the four lowest temperature runs in the W-3 case. The four runs are at injection temperatures of 380K, 392K, 394K, and 400K, and represent increasing degrees of superheat. It can be observed from this plot that, for lower degrees of superheat, the vapor formation close to the wall is very high whereas the amount of vapor formed in the interior of the nozzle is low. This is similar to a cavitating nozzle in which all the phase change occurs due to the pressure drop at the inlet corner and is limited to areas closer to the wall.

The low degree of superheat implies that the liquid has very little energy to provide for vaporization. As a result, the time for vaporization is high and the residence time in the nozzle limits the vapor formation. However, the main cause of the vapor formation close to the wall is the large pressure drop at the inlet corner. The decrease in the near-wall vapor formation is due to a reduction in this pressure drop with increasing degree of superheat.

This behavior can be explained as follows. As the flow moves beyond the inlet corner, it continues to undergo vaporization, and hence its velocity increases while the pressure decreases. This means that the pressure drop is no longer concentrated at the inlet corner as in colder cases [79]. Since the pressure drop at the inlet is diminished, the amount of vapor formed close to the wall at the inlet corner is also reduced with increasing degree of superheat. Any further vaporization downstream of the inlet corner is limited by the residence time similar to the flow in the core of the nozzle. This shows that as the degree of superheat is increased, the mass fraction of vapor starts approaching a more uniform profile. Section I can be considered as the geometrically driven flash boiling regime.
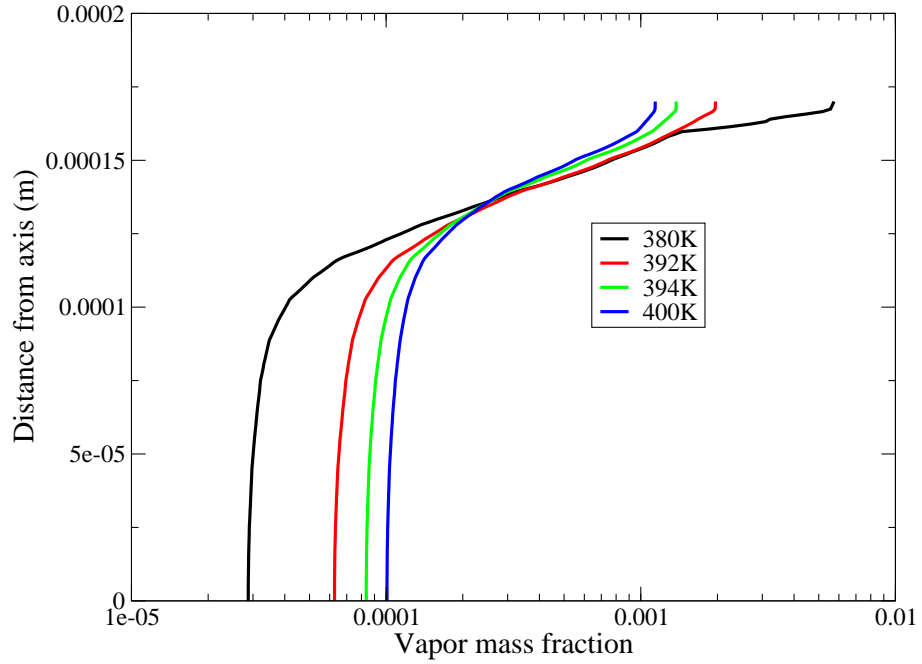
Figure 3.44. Plot of the vapor mass fraction variation along the outlet of the nozzle for four runs in the W-3 case

3.5.2 Section II:

As the degree of superheat is increased further, the amount of vaporization in the nozzle starts increasing as energy is added to the superheated liquid. This can be observed by considering the numerator of the Jakob number formulation (see Eqn. 1.4). Initially, the increase in the value of ΔEq is very slow. This is because, the degree of superheat has a low value and hence the flow through time is comparable to the vaporization time scale. Therefore the flow does not have enough residence time in the nozzle to form a lot of vapor. The length of this regime depends on the relative magnitudes of the time scale of vaporization and the residence time in the nozzle. Assuming a constant vaporization time scale, for longer nozzles and smaller pressure gradients, it would be expected that the residence time is longer and hence the length of this section would be shorter. Section II can be considered as the residence time dominated regime of flash boiling.

3.5.3 Section III:

As the degree of superheat is increased further, the amount of energy available for vaporization also increases. At some point, the amount of energy available is much larger than the amount of energy required. At this point, the vaporization in the nozzle starts increasing rapidly with respect to the degree of superheat. Eventually, if the degree of superheat was increased sufficiently, it would be expected that the value of ΔEq would approach 1. Again, the slope and length of this section would depend on the relative magnitude of the vaporization time scale and the flow residence time in the nozzle. For a given vaporization time scale, a higher pressure gradient or a shorter nozzle would have a smaller slope in section III because of the lower residence times. This behavior can be seen when the cases W-3 and W-4 are compared in Fig. 3.42. Both these cases have the same enthalpy and downstream pressures, but W-4 has a higher pressure gradient. It is observed that W-4 has a smaller slope in section III. Section III may be referred to as the vaporization time dominated regime.

It is seen from the above discussion that the two main factors affecting the flow through the nozzle are: the degree of superheat (indicating the energy available) and the pressure difference through the nozzle (representing the residence time). Hence, Fig. 3.45 is plotted which shows a plot of $\Delta T/T_{inj}$ versus the cavitation parameter K. The cavitation parameter is calculated as

$$K = \frac{P_{inj} - P_{sat}(T_{inj})}{P_{inj} - P_{chm}} \tag{3.4}$$

where $P_{sat}(T_{inj})$ is the saturation pressure obtained at the injection temperature. This plot includes two yellow curves showing ΔEq_{MIN} and ΔEq_{MAX}, which represent the intersections between sections I and II, and sections II and III respectively. The variable ΔEq_{MIN} is calculated as the point at which ΔEq starts increasing with an increase in degree of superheat, and ΔEq_{MAX} represents the point at which the value of ΔEq increases to twice its value at ΔEq_{MIN}.
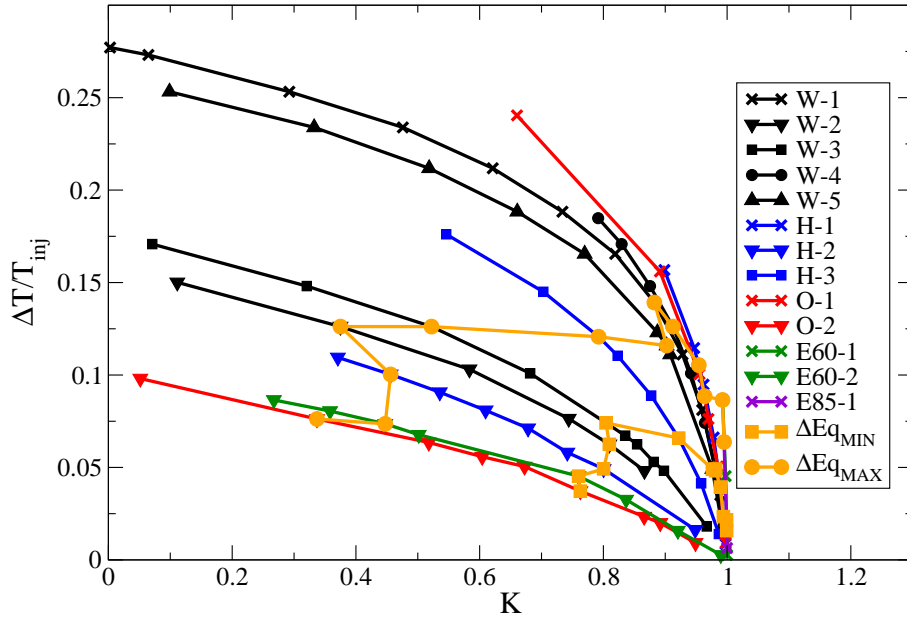
Figure 3.45. Plot of $\frac{\Delta T}{T_{inj}}$ versus the cavitation parameter showing the location of intersection between sections I and II, and sections II and III

It is observed that the two curves (ΔEq_{MIN} and ΔEq_{MAX}) divide the diagram into three sections similar to the Fig. 3.42. This indicates that all cases with conditions lying on the lower right side of the ΔEq_{MIN} curve exist in the geometrically driven regime (Section I). All points lying on the upper left side of the ΔEq_{MAX} curve exist in the vaporization time dominated regime (Section III). Finally, all points between the two curves lie in the residence time dominated regime. If the injection and downstream conditions of an injector are known, they can be plotted on the Fig. 3.45. This will give an idea about how much deviation from equilibrium can be expected in the injector nozzle. Additionally, it can be inferred whether there will be higher vapor formation close to the wall or in the interior.

In order to further analyze this behavior, a different nozzle with a diameter of 0.34mm and an L/D ratio of 6 was used. The case O-1 was simulated and the results are plotted in Fig. 3.46. It can be seen that again the overall behavior is similar to the cases simulated in Fig. 3.42. A few factors to note are that since the L/D

94
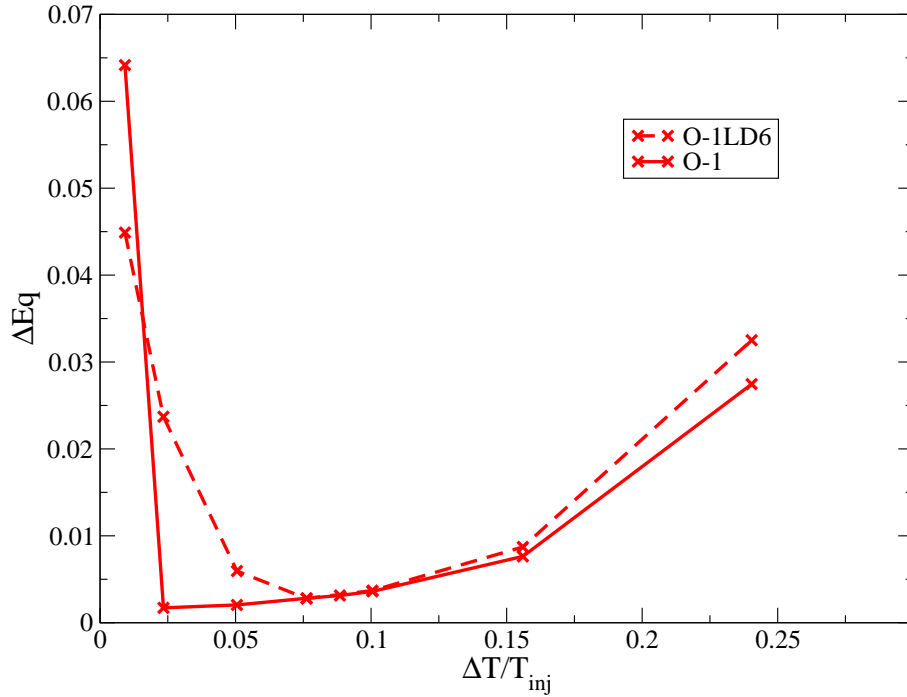
Figure 3.46. Plot of ΔEq versus $\frac{\Delta T}{T_{inj}}$ for the O-1 case for nozzles with L/D ratios of 4 (O-1) and 6 (O-1LD6).

ratio of the new nozzle is higher, the fluid has more residence time in the nozzle and this leads to a higher slope in section III and in section I. This confirms that as the residence time inside the nozzle reduces, the length of the residence time dominated regime (section II) increases. This can also be seen when other cases having the same downstream degree of superheat but varied upstream pressures are compared, for eg; W-2, W-3, and W-4; O-1 and O-2; and, E60-1 and E60-2.

Finally, the case E60-2 was simulated using the 3D 6-hole injector presented in section 3.4 to see if the trends observed in the 2D cases are reproduced. The plot of ΔEq versus $\Delta T/T$ is shown in Fig. 3.47. It can be observed from Fig. 3.47 that the sections II and III can be identified in the plot. However the plot does not show section I. The important point to be noted is that the 3D nozzle has an L/D ratio close to 2 and hence, even though the conditions for E60-2 are same for the 2D and 3D cases, the residence time in the 3D nozzle will be much shorter. Therefore, it
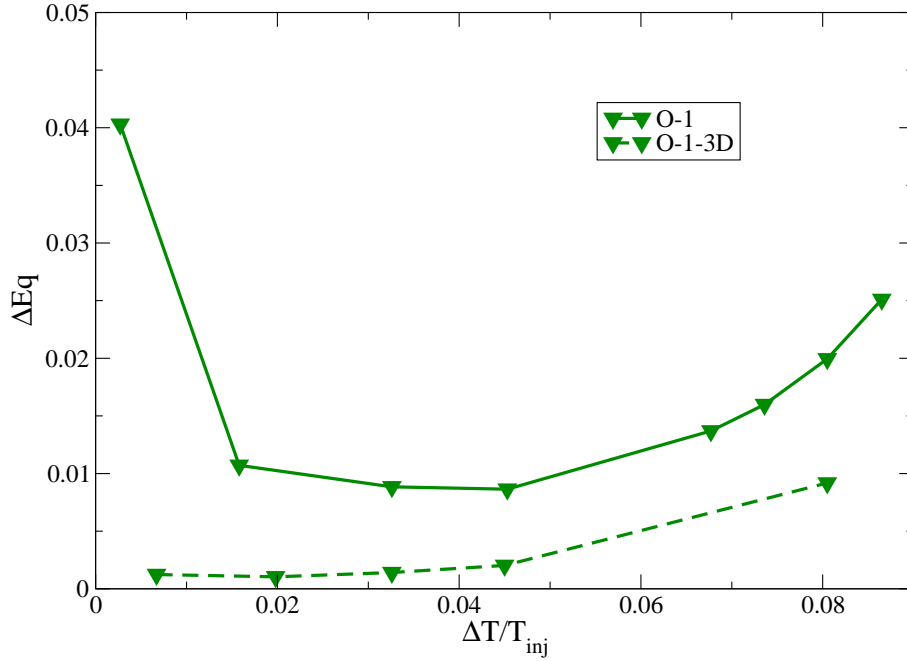
Figure 3.47. Plot of ΔEq versus $\frac{\Delta T}{T_{inj}}$ for a 3D, 6-hole injector (O-1-3D) with L/D of 2, compared with a 2D nozzle (O-1) with L/D ratio of 4

would be expected that the section II starts earlier and is longer than the 2D case. Also, the slope of the curve in section III should be smaller for the 3D nozzle. These observations are reproduced in Fig. 3.47. The reason for the absence of section I could be that the nozzle is so short that the residence time dominates the phase change process in the geometrically driven regime as well. Additionally, it is possible that since the 2D nozzles were run under axisymmetric conditions, the behavior of the full 3D nozzle is different.

All the empirical parameters in the time scale of vaporization formulation, Eq. 2.15, were kept the same for the different fluids. Though this assumption indicates that the time scale of vaporization will follow the same empirical law, the coupling between the time scale of vaporization and the residence time is unaffected and depends on the interaction between the vaporization model and the CFD flow solver. Hence it can be expected that the trends predicted in this study are accurate. This study will be useful when deciding the conditions that must be maintained in an in-

jector in order to achieve a certain degree of vaporization in the nozzle. Additionally, this study shows the importance of studying flash boiling since, from Fig. 3.43, it is evident that the amount of vapor inside the nozzle can deviate greatly from the equilibrium condition.

CHAPTER 4

CONCLUSIONS

4.1 Multi-Component Fuel Model

A simple model known as GEFlash was proposed to model the properties of gasoline-ethanol fuel blends. This approach gave very good predictions for the vapor pressure and captured the azeotropic nature of these blends. The density predictions were very good for high ethanol content blends but deviated near the pure gasoline region. The main reason for this was that gasoline was considered to be equivalent to iso-octane in the Rackett equation. The GEFlash formulation used an ideal gas equation coupled with the Clausius-Clapeyron equation to calculate the enthalpy of vaporization. Additionally, the enthalpy of vaporization was assumed to be constant over the temperature range considered. These assumptions are not considered acceptable for modeling these non-ideal mixtures, however, the enthalpy of vaporization was solely used to calculate the final enthalpy in the temperature and vapor fraction loop (see Fig. 2.5). Hence, any inaccuracies due to this assumption will be manifested in the distillation curve predictions presented in Figs. 3.7 and 3.8. Since it is found that the mole fraction of vapor predictions are accurate for GE blends with high ethanol content, it is proposed that the modeling assumptions are also acceptable for these blends. Additionally, a curve fit to the enthalpy of vaporization values of Kar et al. was used instead of the calculating it from the vapor pressure as shown in section 2.2.2 and it was found that the change in the mole fraction of vapor prediction was negligible.

A method for using Aspen Plus for volatility studies of gasoline-ethanol blends was proposed. This method was first used to generate a look-up table with properties of water. This table was read by the flash boiling solver HRMFoam in order to simulate the test cases of Reitz [74]. Good agreement was obtained with the experimental data and with the results obtained by running HRMFoam with a look-up table generated by the REFPROP code. A surrogate for indolene was used to represent gasoline in the gasoline-ethanol blended fuels and the predictions for the different properties were compared with experimental data. It was found that the density values were more accurate for high ethanol content blends whereas the vapor pressure values were more accurate for lower ethanol contents. Also, the D86 distillation curves for different gasoline-ethanol blends were compared with the experimental data of Takeshita et al. [89]. It was observed that the Aspen Plus distillation curves showed a weaker response to increase in ethanol content as compared to the experimental data. However, the trends agreed with those observed in the experiments.

The GEFlash model can be a valuable resource for modeling vapor-liquid equilibrium of gasolines with high ethanol content due to its simple concept and reduced computational effort. Also, this is the first time that a model for the VLE properties of gasoline-ethanol fuel blends including volatility has been proposed and rigorously tested with experimental data available in open literature. Additionally, since the source code of the GEFlash model was developed in-house, improvements can be made to the separate sub-models in order to improve predictions, whereas the source code and the empirical constant databases used by Aspen Plus are not accessible by the general scientific community.

One important point to be noted is that since gasoline is a mixture of hundreds of components, it is extremely difficult to predict the properties by using a generic model. In this work, different experimental data have been used to validate the various parts of the models. Many of these experiments have been carried out in

different countries where the specifications for gasoline are nonuniform. For example, a gasoline with a high vapor pressure in a hot climate has a tendency to cause vapor lock in the fuel lines. Hence it would be unreasonable to expect that any model would be able to match all the experimental data accurately. Keeping these points in mind, it is concluded that the shortcomings of the proposed modeling procedures are acceptable and these models can be used to give an idea about the volatility behavior of gasoline-ethanol blends.

4.2 Flash Boiling Simulations

The Homogeneous Relaxation Model coupled with a pseudo fluid approach was used for modeling the flash boiling flow. This model has a very simple concept and the current formulation allows it to be extended to 2D and 3D flows without much computational effort. However, this model uses an empirical time scale for capturing the non-equilibrium nature of flash boiling. This empirical time scale was initially adjusted to match experiments for water and hence might not be very valid for other fluids. The capability of the HRMFoam solver to predict flash boiling behavior has been shown in previous publications [80, 33, 49], however, none of the 3D cases presented in previous work were validated against experimental data. In this work, HRMFoam was used to simulate the high pressure swirl injector experiments of Schmitz et al [81], using n-hexane as fuel for four different injection temperatures. The results showed a decrease in the spray cone angle with an increase in the injection temperature. This trend was similar to that observed by Schmitz et al. The flash boiling model also predicted the sharp decrease in the spray cone angle between injection temperatures of 323K and 343K which was attributed to the commencement of flash boiling by Schmitz et al. Though the trend of the simulation results matched the experimental data, the exact values were different because the geometry used by Schmitz et al. was not known and had to be approximated. In addition, the method

100

used for spray cone angle measurement was different from that used by Schmitz et al. From the contour plots, it was observed that the simulation results predicted the curving of the velocity contour inwards which was believed to be a part of the cone collapse mechanism. However, the complete collapse of the spray cone, which was observed in the experiments, was not seen in the simulations. This was attributed to two possibilities: a two-phase fuel mixture was used in the exit chamber instead of air; and the simulation did not account for effects of atomization of the jet. This is the first time that 3D, validated results for flash boiling flows have been presented.

Simulations were performed using a multi-component JP8 surrogate as working fluid in four 2D, axisymmetric nozzle cases. The test conditions were adjusted so that no phase change was expected inside the nozzle. From Cases 1 and 2, it was found that the radius of the nozzle inlet corner governed whether the flow separated and also the amount of oscillations in the flow. This result was consistent with the observations of Canino and Heister [15]. The Cases 3 and 4 introduced perturbations in the flow before it entered the nozzle. These two cases showed large regions of recirculation at the inlet corner along with vapor generation due to the sharp pressure drop. The discrete Fourier transform plots of Cases 3 and 4 showed that a number of frequencies were responsible for the oscillations in the flow. These 4 cases were simulated to give experimentalists an insight about the flow behavior in these nozzle so as to assist them in conducting flash boiling experiments.

The HRMFoam solver was coupled with the GEFlash model to simulate two types of injectors which have been used in Gasoline Direct Injection systems: a high pressure swirl injector and a 6-hole injector. In the case of the high pressure swirl injector, two simulations were performed with E85 having the same injection conditions but different chamber pressures. It was found that by sufficiently reducing the downstream pressure, the collapse of the hollow cone, which was not noted in the results with n-hexane, could be observed. Additionally, the liquid penetration into the plenum

also decreased with a decrease in chamber pressure. The 6-hole injector was used to compare between two gasoline-ethanol blends E60 and E85 for the same injection and chamber conditions. It was observed that E60 showed a higher spray cone angle and a reduced liquid penetration into the chamber. This is expected since E60 has a higher vapor pressure than E85. These results showed the expected trends but in order to quantitatively validate them, comparisons with experimental results will be required.

Additionally, a previously unexplored phenomenon known as "string flash boiling" was observed inside the multi-hole injectors. This phenomenon shows vapor formation due to a vortex which is centrally located in the nozzle. Bridging vortices were seen originating from the central vortex and touching the periodic boundaries indicating connections between adjacent holes. This phenomenon has been observed in cavitating flows but this is the first evidence of its occurence in flash boiling. Again, experimental data would be required to confirm the existence of string flash boiling.

Finally, A parametric study was conducted using three single-component fluids (water, n-octane, and n-hexane) and two multi-component fluids (E60 and E85). A total of 102 different adiabatic cases were simulated and the deviation of these cases from equilibrium conditions was plotted with respect to the degree of superheat. Three distinct regions were observed in the plot: a geometrically driven regime (section I), a residence time driven regime (section II) and a vaporization time driven regime (section III). In order to collapse this information into one plot, the cavitation parameter was plotted against the degree of superheat. The plot included the intersections between the sections I and II, and sections II and III. It was found that the plot showed three separate regions representing the different regimes of the flash boiling flow. This indicates that for certain injector nozzle operating conditions, the amount of deviation from equilibrium can be predicted. This study will help

researchers in knowing when an equilibrium or frozen flow assumption is acceptable and when it is necessary to include a finite-rate heat transfer model.

In addition, a 3D 6-hole injector was simulated to see if it reproduced the same behavior as the 2D cases. It was found that the 3D case also clearly showed sections II and III. The absence of section I could be due to one of two reasons. Firstly, the 3D nozzle had a lower L/D ratio as compared to the 2D cases and hence, it was possible that the vaporization in the section I was also limited by the residence time. The second reason could be due to the fact that the 2D nozzles assume axisymmetric conditions which might alter their vaporization characteristics. An important point to be noted is that this is a preliminary study to understand the nature of flash boiling flows in injector nozzles. In order to make this study more reliable, the results would have to be confirmed through experimental observations.

4.3 Contributions of the Current Work

The first task in this work was to develop an application to simulate flash boiling flows in 3D fuel injectors for the Gasoline Direct Injection system. The HRMFoam solver had been initially tested and validated with 2D axisymmetric injector nozzles and was found to be highly unstable for 3D flows. Through the current work, a number of improvements were incorporated into the HRMFoam solver which included, but were not limited to, developing a thermodynamically consistent boundary condition for density, using object oriented programming techniques to improve the code management and efficiency, incorporating numerical tricks to improve the stability, etc. At the conclusion of this work, the HRMFoam solver has evolved into a dependable tool which can be used for analyzing 3D injector flows. The simulations with the high-pressure swirl injector using n-hexane, presented in section 3.2 and in Neroorkar et al. [61], are the first validated 3D flash boiling results that have been found in literature.

The next task of the current work was to formulate a method to simulate flash boiling in gasoline-ethanol blends. After exploring existing literature, the GEFlash model was developed to provide the properties of the blended fuels. In addition, a model for the blended fuels was built in the Aspen Plus software. Both these models were validated against existing experimental data, and the complete formulations are presented in section 2.2 and are published in the journal of Fuel [62]. The GEFlash model is the first complete modeling procedure which provides the vapor-liquid equilibrium properties including the distillation behavior for gasoline-ethanol blended fuels.

In simulations with the HRMFoam solver coupled with the GEFlash model, a new and previously unexplored phenomenon of string flash boiling was observed and has been presented in this work. This phenomenon has the potential to greatly affect the spray behavior inside the engine cylinder.

CHAPTER 5

FUTURE WORK

This section includes a few suggestions about the direction this work should take in the future. The first suggestion is for the improvement of the GEFlash model to account for the multi-component nature of gasoline. The basic assumption that the blended fuel is a binary mixture of ethanol and gasoline needs to be changed. In order to achieve this, firstly, a surrogate needs to be adopted to represent gasoline. Then, the equation to calculate vapor pressure, Eqn 2.25, needs to be modified to the following

$$P_{vap} = \sum_{i=1}^{N+1} x_i \gamma_i P_{i,vap} \tag{5.1}$$

where, N refers to the number of components in the surrogate, and the $N + 1^{th}$ component is ethanol. The multi-component formulation of the Wilson equation will replace the Eqns. 2.26 and 2.27. This can be given as follows [73]

$$ln(\gamma_i) = -ln(\sum_{j=1}^{N+1} x_j \Lambda_{ij}) + 1 - \sum_{k=1}^{N+1} \frac{x_k \Lambda_{ki}}{\sum_{j=1}^{N+1} x_j \Lambda_{kj}} \tag{5.2}$$

In this case, the parameters Λ need to be obtained from experimental data for binary mixtures between every binary pair existing in the mixture. The other sub-models used in GEFlash, like the modified Rackett equation, the Rachford-Rice equation, and the CEOS have been presented in their multi-component forms in section 2.2.

All the cases simulated in this work were laminar even though these were high Reynolds number flows where turbulence would be an important factor. A turbulence

model can be incorporated in the HRMFoam solver. An example of a turbulence model suitable for this application might be the model of Demoulin et al. [21]. They proposed a form of the $k - \epsilon$ equation to model flows with high density variations intended for atomization applications. However, it should be noted that the $k - \epsilon$ model has inherent disadvantages since a scalar kinetic energy is used to model turbulence. This assumption implies that the $k - \epsilon$ model cannot correctly capture the anisotropic nature of turbulence. Additionally, the $k - \epsilon$ model assumes that the Reynolds stresses change instantaneously when the mean rate of strain changes. Non-equilibrium between the Reynolds stresses and the mean strain rate are important for rapidly changing flow conditions [25].

The next suggestion relates to improving the formulation of the HRM equation itself. The time scale that is used to represent the deviation from equilibrium is empirical and was initially formulated for water. The use of this time scale for other fluids like n-octane, n-hexane, and the gasoline-ethanol blends is not accurate. Hence, as experimental data become available, it is essential that this time scale correlation be improved so that it accurately represents other fluids.

Once the above-mentioned suggestions are implemented, the parametric study presented in the current work can be extended to include more 2D and 3D nozzle geometries in order to better analyze the behavior of flash boiling flows in fuel injectors.

The phenomenon of string flash boiling should be studied in more detail since the presence of these vortices can profoundly change the spray behavior. For cavitating flows, string cavitation has been found to be sensitive to the needle lift and size of the nozzle [6]. Parametric studies should be conducted in order to analyze the factors affecting the nature of the string flash boiling flow.

The final suggestion is to couple the HRMFoam solver with a program that can accurately model atomization and the subsequent spray evolution. This coupling can be achieved by using the HRMFoam results at the nozzle outlet as inlet conditions

for the spray model. Similar work has been presented by Ning et al. [64] in which a cavitation model based on the HEM approximation was coupled with an atomization model. Such a coupling would help to better understand the effect of flash boiling on the spray characteristics like cone angle, droplet sizes and distribution, etc.

APPENDIX

INPUT FILES FOR GEFlash AND OUTPUT FORMAT

The GEFlash programs needs three input files. The first one, known as Pure-vap.inp gives the pure component vapor pressure of ethanol and gasoline and is shown below

```
9
#Temp(degK)    vap pressure ethanol(pa)   vapor pressure gasoline(pa)
273            1585.00                         5840.00
283            3120.00                        10230.00
293            5840.00                        17610.00
303            8949.00                        32631.6
313           14803.00                        44932.7
323           24210.5                         61578.9
333           40526.3                         82105.3
343           73000.0                        110000.00
353          109000.0                        145000.00
```

The first column represents the temperature, and the second and third columns represent the corresponding vapor pressures for pure ethanol and gasoline respectively. This list can be extended as more experimental data becomes available. The second input file is known as Thermoprops.inp and gives the various thermodynamic properties and constants required by the code. The layout of this file is shown below

```
Equation of State :1(RK),2(SRK),3(Peng-Robinson),4(Peng-Robinson-Gasem), 5(PRSV), 6(modified Rackett)
6
Ethanol###############################################################################
Tcrit(K)  Pcrit(Pa)  Volcrit(m^3/mol)    Molecular Wt(kg/kmol)    moleFraction
513.9     6140E3     167E-6                  46.069                  0.941

Accentric Factor K1 (For PRSV) ZRA(For modified Rackett) Specific Heat(CP) Viscosity Conductivity
0.644            -0.16816      0.2502                    2.38              0.000655    0.15

ISO-OCTANE###########################################################################
Tcrit(K)  Pcrit(Pa)  Volcrit(m^3/mol)    Molecular Wt(kg/kmol)    moleFraction
544.0     25.7E5      468E-6                 114.232                 0.059

Accentric Factor  K1 (For PRSV) ZRA(For modified Rackett) Specific Heat(CP) Viscosity  Conductivity
0.303            0.04464       0.2684                    2.16              0.000655   0.15
```

Finally, the last input file called PH.inp is needed to specify the pressure and enthalpy range of the final property table and the reference temperature and enthalpy values. This is shown below

```
#Tref(K)    Href(j/kg)
273   0
P_start   6000   P_end   3e6     P_step   200.00
H_start   0      H_end   180000  H_step   5000.00
```

The output from GEFlash has following form

```
GEFlash Ethanol Fuel = E84.98423227 with 0.941  moles ethanol
P_start 6000 P_end 3000000 stepP 200
H_start 0 H_end 180000 stepH 5000
Points 553927 pres 14971 Hres 37
CriticalPressure  2.56E6
# Pressure(Pa) Enthalpy(j/kg) VapMassFract  Density(kg/m^3)  RhoV(kg/m^3)   RhoL(kg/m^3)   Temp(K)
         Viscosity(microPa.s)  Conductivity(W/m.K)  Cv(kJ/kgK)   Cp(kJ/kgK)  SOS(m/s)   PBUB(Pa)
 6000     0    0  798.4298906    0.07183364069  798.4298906  273.0000024
         655  0.15   1e-15   2.36702      1e-15   3250.137255
 6000     5000  0  796.1902698    0.08413000433  796.1902698  275.1123624
         655  0.15   1e-15   2.36702      1e-15   3835.02387
 6000     10000  0  793.9427141    0.09624411904  793.9427141  277.2247224
         655  0.15   1e-15   2.36702      1e-15   4419.910484
 6000     15000  0  791.6871074    0.1081797787   791.6871074  279.3370824
         655  0.15   1e-15   2.36702      1e-15   5004.797098
 6000     20000  0  789.4233308    0.1199406801   789.4233308  281.4494424
         655  0.15   1e-15   2.36702      1e-15   5589.683713
 6000     25000  0.002630909937  46.10111593    0.1288064272  787.718742   283.0349402
         655  0.15   1e-15   2.36702      1e-15   6287.9504
 6000     30000  0.01174959458  11.02497352    0.1313564917  787.4378334  283.2958035
         655  0.15   1e-15   2.36702      1e-15   7299.141996
 6000     35000  0.02068632308  6.420077752    0.1338771177  787.159556   283.5541062
         655  0.15   1e-15   2.36702      1e-15   8310.333592
 6000     40000  0.02944729497  4.604413745    0.136361948   786.8846329  283.8091807
         655  0.15   1e-15   2.36702      1e-15   9321.525189
```

As mentioned in the first line in the above table, this output was generated for E85. The critical pressure value of iso-octane is used for the gasoline ethanol blends in the absence of a better estimate. The different properties included in the above table are: pressure, enthalpy, mass fraction of vapor, density, saturated vapor density (RhoV), saturated liquid density (RhoL), temperature (Temp), viscosity, thermal conductivity, specific heat at constant volume (Cv) and constant pressure (Cp), speed of sound (SOS), and the vapor pressure (PBUB). For a given blend, this table is read into the HRMFoam code, and depending on the local enthalpy and pressure, interpolations are performed to find the correponding properties. As seen above, arbitrary values are used for the specific heat at constant volume and the speed of sound because these two properties are presently not used in the HRMFoam solver.

BIBLIOGRAPHY

[1] ASTMD86: Standard test method for distillation of petroleum products. *Annual Book of ASTM Standards 5.01* (1994).

[2] Alternative fuels:E85 and flex fuel vehicles. Tech. Rep. EPA420-F-06-047, U.S. Environmental Protection Agency, October 2006.

[3] E85 and energy content–how much energy is there? Tech. rep., National Ethanol Vehicle Coalition, 2007. cited by [77].

[4] Greener fuels, greener vehicles: A state resource guide. Tech. rep., National Governors Association, 2008.

[5] Alajbegovic, A., Meister, G., Greif, D., and Basara, B. Three phase cavitating flows in high-pressure swirl injectors. *Experimental Thermal and Fluid Science 26*, 6-7 (2002), 677 – 681.

[6] Arcoumanis, C., Gavaises, M., Nouri, J.M., Abdul-Wahab, E., and Horrocks, R.W. Analysis of the flow in the nozzle of a vertical multi hole diesel engine injector. *SAE Transactions Journal of Engines 107* (1998).

[7] Attou, A., Giot, M., and Seynhaeve, J.M. Modeling of steady-state two phase bubbly flow through a sudden enlargement. *International Journal of Multiphase Flow 40*, 14 (1997), 3375–3385.

[8] Balabin, R., Syunyaev, R.Z., and Karpov, S.A. Molar enthalpy of vaporization of ethanol-gasoline mixtures and their colloid state. *Fuel 86* (2007), 323–327.

[9] Bennett, A., Lamm, S., Orbey, H., and Sandler, S.I. Vapor-liquid equilibria of hydrocarbons and fuel oxygenates. *Journal of Chemical and Engineering Data 38*, 2 (1993), 263–269.

[10] Bianchi, G. M., Negro, S., Forte, C., Cazzoli, G., and Pelloni, P. The prediction of flash atomization in GDI multi-hole injectors. *SAE Paper 2009-01-1501* (2009).

[11] Bilicki, Z., and Kestin, J. Physical aspects of the relaxation model in two-phase flow. *Proceedings of the Royal Society of London: Series A 428* (1990), 379–397.

[12] Bilicki, Z., Kwidziński, R., and Mohammadein, S.A. Evaluation of the relaxation time of heat and mass exchange in the liquid-vapor bubble flow. *International Journal of Heat and Mass Transfer 39*, 4 (1996), 753 – 759.

[13] Blinkov, V.N., Jones, O.C., and Nigmatulin, B.I. Nucleation and flashing in nozzles -2 :comparison with experiments using a five equation model for vapor void development. *International Journal of Multiphase Flow 19* (1993), 965–986.

[14] Buros, O.K. The ABCs of desalting. Tech. rep., International Desalination Association, Topesfield, Massachusetts, USA, 2000.

[15] Canino, J., and Heister, S.D. Contributions of orifice hydrodynamic instabilities to primary atomization. *Atomization and Sprays 19*, 1 (2009), 91–102.

[16] Chang, D.-L., and Lee, C.-F. Preliminary computational studies of flash boiling for fuel injectors in gasoline direct injection automotive engines. *Proceedings of the Intersociety Energy Conversion Engineering Conference 37* (2002), 464–469.

[17] Chang, N.A., Yakushiji, R., Dowling, D.R., and Ceccio, S.L. Cavitation visualization of vorticity bridging during the merger of co-rotating line vortices. *Physics of Fluids 19* (2007).

[18] Corradini, M.L. *Fundamentals of Multiphase Flow.* 1997. `http://wins.engr.wisc.edu/teaching/mpfBook/main.html`, Accessed 7th July 2009.

[19] Cotterman, R.L.and Bender, R., and Prausnitz, J.M. Phase equilibria for mixtures containing very many components:development and application of continuous thermodynamics for chemical process design. *Industrial Engineering Chemical Process Design Development 24* (1985), 194–203.

[20] Curtis, E., Russ, S., Aquino, C., Lavoie, G., and Trigui, N. The effects of injector targeting and fuel volatility on fuel dynamics in a PFI engine during warm-up: Part II- modeling results. *SAE paper 982519* (1998).

[21] Demoulin, F.-X., Beau, P.-A., Blokkeel, G., Mura, A., and Borghi, R. A new model for turbulent flows with large density fluctuations: application to liquid atomization. *Atomization and Sprays 17* (2007), 315 – 345.

[22] Desideri, U., and Bidini, G. Study of possible optimisation criteria for geothermal power plants. *Energy Conversion and Management 38*, 15-17 (1997), 1681 – 1691.

[23] Dillon, H.E., and Penoncello, S.G. A fundamental equation for calculation of the thermodynamic properties of ethanol. *International Journal of Thermophysics 25* (2004), 321–335.

[24] Downar-Zapolski, P., Bilicki, Z., Bolle, L., and Franco, F. The non-equilibrium relaxation model for one-dimensional flashing liquid flow. *3rd ASME/JSME Joint Fluids Engineering Conference 208*, 616 (1999).

[25] Durbin, P.A., and Pettersson Reif, B.A. *Statistical Theory and Modeling for Turbulent Flows.* John Wiley and Sons, New York ,NY, USA, 2001, 2001.

[26] Edwards, T., and Maurice, L. Surrogate mixtures to represent complex aviation and rocket fuels. *AIAA-1999-2217* (1999). AIAA/ASME/SAE/ASEE Joint Propulsion Conference and Exhibit, Los Angeles, CA.

[27] Fauske, H.K. Contribution to the theory of two-phase, one component critical flow. Tech. Rep. ANL-6633, Argonne National Lab, 1962.

[28] Ferziger, J.H., and Peric, M. *Computational Methods for Fluid Dynamics.* Springer, 2002.

[29] French, R., and Malone, P. Phase equilibria of ethanol fuel blends. *Fluid Phase Equilibria 228-229* (2005), 27 – 40.

[30] Gasem, K.A.M., Gao, W., Pan, Z., and Robinson, R.L. A modified temperature dependence for the Peng-Robinson equation of state. *Fluid Phase Equilibria 181*, 1-2 (2001), 113 – 125.

[31] Gmehling, J., and Onken, U. *Vapor-liquid equilibrium data collection, chemistry data series*, vol. 1. DECHEMA, Frankfurt, 2006.

[32] Gopalakrishnan, S. *Modeling of thermal non-equilibrium in superheated injector flows.* PhD thesis, University of Massachusetts Amherst, Amherst, Ma, United States, 2010.

[33] Gopalakrishnan, S., and Schmidt, D.P. A computational study of flashing flow in fuel injector nozzles. *SAE Paper-2008-01-0141* (2008).

[34] Graskow, B.R., Kitttelson, D.B., Abdul-Khalek, I.S., Ahmadi, M.R., and Morris, J.E. Characterization of exhaust particulate emissions from a spark ignition engine. *SAE Paper 980528* (1998).

[35] Hahne, E., and Barthau, G. Evaporation waves in flashing processes. *International Journal of Multiphase Flow 26*, 4 (2000), 531 – 547.

[36] Henry, R.E., and Fauske, H.K. The two-phase critical flow of one component mixtures in nozzles, orifices and short tubes. *Journal of Heat Transfer 93* (1971), 179–187.

[37] Hill, L.G. *An experimental study of evaporation waves in a superheated liquid.* PhD thesis, California Institute of Technology,Pasadena, Ca, 1991.

[38] Hsieh, W.-D., Chen, R.-H., Wu, T.-L., and Lin, T.-H. Engine performance and pollutant emission of an SI engine using ethanol-gasoline blended fuels. *Atmospheric Environment 36*, 3 (2002), 403 – 410.

[39] Huber, M.L. *NIST thermophysical properties of hydrocarbon mixtures database (SUPERTRAPP).* U.S. Department of Commerce, National Institute of Standards and Technology, 2003.

[40] Jankowski, A., Sandel, S., Seçzyk, J., and Siemińska-Jankowska, B. Some problems of improvement fuel efficiency and emissions in internal combustion engines. *Journal of KONES Internal Combustion Engines*, 1-2 (2002), 333 – 356.

[41] Kar, K., Last, T., Haywood, C., and Raine, R.R. Measurement of vapor pressures and enthalpies of vaporization of gasoline and ethanol blends and their effects on mixture preparation in an SI engine. *SAE Paper 2008-01-0317* (2008).

[42] Karman, D. Ethanol fuelled motor vehicle emissions: A literature review. Tech. rep., Air Health Effects Division, Health Canada, 2003.

[43] Kato, H., Kayano, H., and Kageyama, Y. A consideration of thermal effects on cavitation bubble growth. *Cavitation and Multiphase flow ASME FED vol. 194* (1994).

[44] Kawano, D., Senda, J., Wada, Y., and Fujimoto, H. Fuel design concept for low emission in engine systems 4th report:effect of spray characteristics of mixed fuel on exhaust concentrations in diesel engine. *SAE Paper 2003-01-1038* (2003).

[45] Kim, Y.K., Twai, N., Suto, H., and Tsuruga, T. Improvement of alcohol engine performance by flashing injection. *JSAE Review 2* (1980), 81–86.

[46] Knapp, R.T., James, W.D, and Hammitt, F.G. *Cavitation*. McGraw-Hill, 1970.

[47] Kretschmer, C.B., Nowakowska, J., and Wiebe, R. Densities and liquid–vapor equilibria of the system ethanol–isooctane (2,2,4-trimethylpentane) between 0 and 50°C. *Journal of the American Chemical Society 70*, 5 (1948), 1785–1790.

[48] Landau, L.D., Lifšic, E.M., Pitaevskii, L.P, Sykes, J.B., and Kearsley, M.J. *Statistical Physics*. Pergamon, 1969.

[49] Lee, J., Madabhushi, R., Fotache, C., Gopalakrishnan, S., and Schmidt, D. Flashing flow of superheated jet fuel. *Proceedings of the Combustion Institute 32*, 2 (2009), 3215 – 3222.

[50] Lemmon, E.W., Huber, M.L., and McLinden, M.O. *NIST Standard Reference Database 23: Reference Fluid Thermodynamic and Transport Properties-REFPROP, Version 8.0*. National Institute of Standards and Technology, Gaithersburg, 2007.

[51] Lippert, A.M. *Modeling of multicomponent fuels with the application to sprays and simulation of diesel engine cold start*. PhD thesis, The University of Wisconsin-Madison, 1999.

[52] Mikic, B.B., Rohsenow, W.M., and Griffith, P. On bubble growth rates. *International Journal of Heat and Mass Transfer 13* (1970), 657–666.

[53] Mitroglou, N.and Nouri, J.M., Yan, Y., Gavaises, M., and Arcoumanis, C. Spray structure generated by multi-hole injectors for gasoline direct-injection engines. *SAE Paper-2007-01-1417* (2007).

[54] Miyatake, O., and Tanaka, I. Bubble growth in uniformly superheated water at reduced pressures, part i: numerical analysis and derivation of a simplified expression. *Transactions JSME, Series B* (1982).

[55] Miyatake, O., Tanaka, I., and Lior, N. A simple universal equation for bubble growth in pure liquids and binary solutions with a non-volatile solute. *International Journal of Heat and Mass Transfer 40*, 7 (1997), 1577–1584.

[56] Mohammadein, S.A. The derivation of thermal relaxation time between two-phase bubbly flow. *Heat Mass Transfer 42*, 5 (2006), 364–369.

[57] Moody, F.J. Maximum flow rate of a single component, two-phase mixture. *Journal of Heat Transfer 82* (1965).

[58] Mori, Y., Hijikata, K., and Nagatani, T.K. Effect of dissolved gas on bubble nucleation. *International Journal of Heat and Mass Transfer 19* (1976), 1153–1159.

[59] Nan, Z., Tan, Z.-C., and Sun, L. Investigation on thermodynamic properties of ethanol + gasoline blended fuel. *Energy and Fuels 18*, 1 (2004), 84–89.

[60] Nasirzadeh, K., Zimin, D., Neueder, R., and Kunz, W. Vapor-pressure measurements of liquid solutions at different temperatures: Apparatus for use over an extended temperature range and some new data. *Journal of Chemical and Engineering Data 49*, 3 (2004), 607–612.

[61] Neroorkar, K., Gopalakrishnan, S., Schmidt, D., and Grover Jr., R.O. Simulation of flash-boiling in pressure swirl injectors. *11th Triennial International Conference on Liquid Atomization and Spray Systems* (2009). Vail, Colorado USA.

[62] Neroorkar, K., and Schmidt, D. Modeling of vapor-liquid equilibrium of gasoline-ethanol blended fuels for flash boiling simulations. *Fuel 90*, 2 (2011), 665–673.

[63] Nikam, P.S., Jagdale, B.S., Sawant, A.B., and Hasan, M. Densities and viscosities of binary mixtures of toluene with methanol, ethanol, propan-1-ol, butan-1-ol, pentan-1-ol, and 2-methylpropan-2-ol at (303.15, 308.15, 313.15) K. *Journal of Chemical and Engineering Data 45*, 4 (2000), 559–563.

[64] Ning, W., Reitz, R., Diwakar, R., and A.M., Lippert. An eulerian-lagrangian spray and atomization model with improved turbulence modeling. *Atomization and Sprays 19* (2009), 727 – 739.

[65] Nurick, W.H. Orifice cavitation and its effects on spray mixing. *Journal of Fluids Engineering 98* (1976).

[66] Oh, J.-H., Han, K.-J., Won, D.-B., and Park, S.-J. Vapor-liquid equilibria for the ternary systems of methyl tert-butyl ether + methanol + benzene and methyl tert-butyl ether + methanol + toluene and constituent binary systems at 313.15 K. *Fluid Phase Equilibria 209* (2003), 215 – 228.

[67] Oza, R.D. On the mechanism of flashing injection of initially subcooled fuels. *Journal of Fluids Engineering 106* (1984), 105 – 109.

[68] Oza, R.D., and Sinnamon, J.F. An experimental and analytical study of flash-boiling fuel injection. *SAE Paper 830590* (1983).

[69] Parrish, S.E., and Zink, R.J. Spray characteristics of multi-hole injectors under flash boiling conditions. *ILASS Americas, 21st Annual Conference on Liquid Atomization and Spray Systems* (2008). Orlando, Florida.

[70] Privat, R., Jaubert, J.-N., Garcia, F., and Molière, M. Ethanol-hydrocarbon blend vapor prediction. *Journal of Engineering for Gas Turbines and Power 132*, 9 (2010).

[71] Pumphrey, J.A., Brand, J.I., and Scheller, W.A. Vapor pressure measurements and predictions for alcohol-gasoline blends. *Fuel 79*, 11 (2000), 1405 – 1411.

[72] Reid, B.A., Hargrave, G.K., Garner, C.P., and G, Wigley. An investigation of string cavitation in a true-scale fuel injector flow geometry at high pressure. *Physics of Fluids 22* (2010).

[73] Reid, R.C., Prausnitz, J.M., and Poling, B.E. *The Properties of Gas and Liquids*, 4 ed. McGraw-Hill, New York, 1987.

[74] Reitz, R. A photographic study of flash-boiling atomization. *Aerosol Science and Technology 12* (1990), 561–569.

[75] Reocreux, M. *Contribution a letude des debits critiques en ecoulement diphasique eau-vapeur*. PhD thesis, Universite Scientifique et Medicale de Grenoble, France, 1974.

[76] Richter, H.J. Separated two-phase flow model: application to critical two phase flow. *International Journal of Multiphase Flow 9*, 5 (1983), 511–530.

[77] Roberts, M.C. E85 and fuel efficiency: An empirical analysis of 2007 EPA test data. *Energy Policy 36*, 3 (2008), 1233 – 1235.

[78] Saurel, R., Petitpas, F., and Abgrall, R. Modelling phase transition in metastable liquids: application to cavitating and flashing flows. *Journal of Fluid Mechanics 607* (2008), 313 – 350.

[79] Schmidt, D.P. *Cavitation in Diesel Fuel Injector Nozzles*. PhD thesis, The University of Wisconsin-Madison, 1997.

[80] Schmidt, D.P., Gopalakrishnan, S., and Jasak, H. multidimensional simulation of thermal non-equilibrium channel flow. *Intl. J. of Multiphase Flow 36* (2010), 284–292.

[81] Schmitz, I., Ipp, W., and Leipertz, A. Flash boiling effects on the development of gasoline direct-injection sprays. *SAE Paper 2002-01-2661* (2002).

[82] Sebastian, P., and Nadeau, J.P. Experiments and modeling of falling jet flash evaporators for vintage treatment. *International Journal of Thermal Sciences 41*, 3 (2002), 269 – 280.

[83] Sher, E., Bar-Kohany, T., and Rashkovan, A. Flash-boiling atomization. *Progress in Energy and Combustion Science 34*, 4 (2008), 417 – 439.

[84] Sher, E., and Elata, C. Spray formation from pressure cans by flashing. *Industrial and Engineering Chemistry Process Design and Development* (1977).

[85] Simões-Moreira, J.R., and Shepherd, J.E. Evaporation waves in superheated dodecane. *Journal of Fluid Mechanics 382* (1999), 63 – 86.

[86] Span, R., and Wagner, W. Equations of state for technical applications. ii. results for nonpolar fluids. *International Journal of Thermophysics 24* (2003), 41–109.

[87] Spencer, C.F., and Danner, R.P. Improved equation for prediction of saturated liquid density. *Journal of Chemical and Engineering Data 17* (1972), 236–241.

[88] Stryjek, R., and Vera, J.H. PRSV: An improved Peng-Robinson equation of state for pure compounds and mixtures. *The Canadian Journal of Chemical Engineering 64*, 2 (1986), 323–333.

[89] Takeshita, E.V., Rezende, R.V.P., Guelli U. de Souza, S.M.A., and Ulson de Souza, A.A. Influence of solvent addition on the physicochemical properties of Brazilian gasoline. *Fuel 87*, 10-11 (2008), 2168 – 2177.

[90] Tamim, J., and Hallett, W.L.H. A continuous thermodynamics model for multicomponent droplet vaporization. *Chemical Engineering Science 50*, 18 (1995), 2933 – 2942.

[91] Violi, A, Yan, S., Eddings, E.G., Sarofim, A.F., Granata, S., Faravelli, T., and Ranzi, E. Experimental formulation and kinetic model for JP-8 surrogate mixtures. *Combustion Science and Technology 174* (2002), 399 – 417.

[92] Wagner, W., and Pruss, A. The IAPWS formulation 1995 for the thermodynamic properties of ordinary water substance for general and scientic use. *Journal of Physical and Chemical Reference Data 31* (2002), 387–535.

[93] Wallis, G.B. Critical two-phase flow. *International Journal of Multiphase Flow 6* (1980), 97 – 112.

[94] Weller, H.G., Tabor, G., Jasak, H., and Fureby, C. A tensorial approach to computational continuum mechanics using object-oriented techniques. *Computers in Physics 12*, 6 (1998), 620–631.

[95] Whitten, G.Z., and Reyes, S. Air quality and ethanol in gasoline. In *Proceedings of the ninth annual ethanol conference, policy and marketing* (2004).

[96] Woods, A., Bloom, F., and Orloff, D. Modeling of flash evaporation I: Formulation of the mathematical model. *Mathematical and Computer Modelling 32*, 10 (2000), 1153 – 1169.

[97] Yakoumis, I.V., Kontogeorgis, G.M., Voutsas, E.C., and Tassios, D.P. Vapor-liquid equilibria for alcohol/hydrocarbon systems using the CPA equation of state. *Fluid Phase Equilibria 130*, 1-2 (1997), 31 – 47.

[98] Zhao, F., Lai, M.-C., and Harrington, D.L. Automotive spark-ignited direct-injection gasoline engines. *Progress in Energy and Combustion Science 25*, 5 (1999), 437 – 562.